

Assessing Martian Bedrock Mineralogy Through “Windows” in the Dust
Using Near- and Thermal Infrared Remote Sensing

by

Jason Chi-Shun Lai

A Thesis Presented in Partial Fulfillment
of the Requirements for the Degree
Master of Science

Approved October 2014 by the
Graduate Supervisory Committee:

James Bell, Chair
Philip Christensen
Richard Hervig

ARIZONA STATE UNIVERSITY

December 2014

ABSTRACT

Much of Mars' surface is mantled by bright dust, which masks the spectral features used to interpret the mineralogy of the underlying bedrock. Despite the wealth of near-infrared (NIR) and thermal infrared data returned from orbiting spacecraft in recent decades, the detailed bedrock composition of approximately half of the martian surface remains relatively unknown due to dust cover. To address this issue, and to help gain a better understanding of the bedrock mineralogy in dusty regions, data from the Thermal Emission Spectrometer (TES) Dust Cover Index (DCI) and Mars Reconnaissance Orbiter (MRO) Mars Color Imager (MARCI) were used to identify 63 small localized areas within the classical bright dusty regions of Arabia Terra, Elysium Planitia, and Tharsis as potential "windows" through the dust; that is, areas where the dust cover is thin enough to permit infrared remote sensing of the underlying bedrock. The bedrock mineralogy of each candidate "window" was inferred using processed spectra from the Mars Express (MEx) Observatoire pour la Mineralogie, l'Eau, les Glaces et l'Activité (OMEGA) NIR spectrometer and, where possible, TES. 12 areas of interest returned spectra that are consistent with mineral species expected to be present at the regional scale, such as high- and low-calcium pyroxene, olivine, and iron-bearing glass. Distribution maps were created using previously defined index parameters for each species present within an area. High-quality TES spectra, if present within an area of interest, were deconvolved to estimate modal mineralogy and support NIR results. OMEGA data from Arabia Terra and Elysium Planitia are largely similar and indicate the presence of high-calcium pyroxene with significant contributions of glass and olivine, while TES data suggest an

intermediate between the established southern highlands and Syrtis Major compositions. Limited data from Tharsis indicate low-calcium pyroxene mixed with lesser amounts of high-calcium pyroxene and perhaps glass. TES data from southern Tharsis correlate well with the previously inferred compositions of the Aonium and Mare Sirenum highlands immediately to the south.

ACKNOWLEDGEMENTS

Firstly I would like to express my thanks and appreciation for my advisor, Professor Jim Bell, for accepting me into his distinguished research group, and for the motivation and support that he has provided me over the past two years.

Professors Phil Christensen and Rick Hervig also contributed valuable guidance as members of my thesis committee as well as in the classroom.

Thank you to my colleagues at Arizona State, who have also been my greatest friends during my time here. I am extremely grateful for their support and companionship. From my very first day as a graduate student, Dr. Briony Horgan has been a wonderful mentor. Without her advice, expertise, and willingness to lend a helping hand, this thesis would not have been possible. I would also like to give special thanks to Danika Wellington, Chris Haberle, and Nathan Williams for their assistance with this project. And thank you to Jake Adler, Kristen Bennett, Lauren Edgar, Craig Hardgrove, and countless others who have made life in the desert so enjoyable.

I never had to worry about any technical issues thanks to Austin Godber keeping our group's servers (and coffee machine) running smoothly 24/7. I am also grateful for his ability to inject some light-heartedness into the office whenever it was needed. Stephanie Holaday demonstrated the utmost kindness and patience in making my life as a graduate student as easy as possible.

I would never have gotten the opportunity to study at ASU in the first place if it weren't for the support of Professors Josh Bandfield, Darrel Cowan, and Bruce Nelson, who all helped inspire me to pursue my graduate degree.

And finally, I give enormous thanks to my dear parents Alan and Melissa and my brother Jared, who have loved and supported me long before I started graduate school. Their frequent phone calls to provide whatever help they could were always appreciated.

TABLE OF CONTENTS

| | Page |
|-----------------------|------|
| LIST OF TABLES | vi |
| LIST OF FIGURES | vii |
| MOTIVATION..... | 1 |
| BACKGROUND..... | 2 |
| METHODOLOGY..... | 6 |
| RESULTS..... | 22 |
| DISCUSSION..... | 94 |
| CONCLUSIONS..... | 126 |
| REFERENCES..... | 128 |

LIST OF TABLES

| Table | Page |
|--|------|
| 1. List of TES Dust Cover Index Quality Fields | 7 |
| 2. Spectral Library Used for TES Deconvolution | 20 |
| 3. Areas of Interest Yielding Positive Mineralogical Detections | 27 |
| 4. MARCI Lambertian albedo values for areas of interest in Tharsis | 103 |

LIST OF FIGURES

| Figure | | Page |
|--------|--|------|
| 1. | Identifying “Windows” Using the Dust Cover Index | 8 |
| 2. | Identifying “Windows” Using MARCI | 10 |
| 3. | Detector Join Alignment Correction | 15 |
| 4. | OMEGA Data Processing Sequence..... | 16 |
| 5. | Global Map of Candidate “Windows” | 23 |
| 6. | Age and Surface Type Distribution of Candidate “Windows” | 25 |
| 7. | Arsia Mons OMEGA Results | 29 |
| 8. | Arsia Mons OMEGA Results During Dusty Season | 30 |
| 9. | Arsia Mons TES Results | 32 |
| 10. | OMEGA Spectra of Tharsis Volcanic Constructs | 34 |
| 11. | Williams Crater Context Images | 37 |
| 12. | Williams Crater OMEGA Results | 38 |
| 13. | Williams Crater TES Results | 39 |
| 14. | Pettit Crater OMEGA Results | 44 |
| 15. | Pettit Crater Splotch CTX Image | 45 |
| 16. | Pettit Crater Splotch CTX Image | 46 |
| 17. | Elysium Crater #1 Context Images | 48 |
| 18. | Elysium Crater #1 OMEGA Results | 49 |
| 19. | Elysium Crater #1 Western Streak OMEGA Results | 51 |
| 20. | Elysium Crater #1 TES Results | 52 |

| Figure | Page |
|---|------|
| 21. Aeolis West Context Images | 55 |
| 22. Aeolis West OMEGA Results | 56 |
| 23. Aeolis West TES Results | 57 |
| 24. Aeolis East Context Images | 60 |
| 25. Aeolis East OMEGA Results | 61 |
| 26. Aeolis East TES Results | 62 |
| 27. Cerberus Context Images | 65 |
| 28. Cerberus West OMEGA Results | 67 |
| 29. Cerberus West OMEGA Results, cont. | 68 |
| 30. Cerberus West TES Results | 69 |
| 31. Cerberus Crater OMEGA Results | 72 |
| 32. Cerberus Crater TES Results | 73 |
| 33. Gusev Crater OMEGA Results | 75 |
| 34. Gusev Crater TES Results | 76 |
| 35. Gale Crater OMEGA Results | 79 |
| 36. Gale Crater TES Results | 80 |
| 37. Arabia Crater #1 Context Images | 83 |
| 38. Arabia Crater #1 OMEGA Results | 84 |
| 39. Arabia Crater #1 TES Results | 85 |
| 40. Arabia Crater #2 Context Images | 89 |
| 41. Arabia Crater #2 OMEGA Results | 90 |

| Figure | Page |
|---|------|
| 42. Arabia Crater #2 TES Results | 91 |
| 43. Pyroxene Phase Diagrams | 97 |
| 44. Spectral Classes of Low-Albedo Surfaces on Mars | 98 |
| 45. Spectral Class Type Areas Near Arsia Mons | 100 |
| 46. Spectral Class Type Areas Near Elysium Planitia | 113 |
| 47. Aeolis West: OMEGA Spectra vs. Laboratory Spectra | 119 |
| 48. Spectral Class Type Areas Near Arabia Terra..... | 124 |

MOTIVATION

Mineralogical studies of martian bedrock have been hindered by the presence of a thin and often spectrally opaque dust layer that covers much of the planet (*e.g.*, Palluconi and Kieffer, 1981; Ruff and Christensen, 2002; Bell, 2008). This dust substantially increases the albedo of underlying surfaces, masking the spectral features used to interpret compositional details of low albedo bedrock materials (*e.g.*, Bandfield, 2002; Mustard, 2005; Christensen, 2008). Many of Mars' most interesting surface features are located within these bright dusty regions, including the largest volcanoes on the planet: Olympus Mons, the Tharsis Montes, Alba Patera, and Elysium Mons. As a result, our understanding of the composition of these features is limited. Dusty regions are typically excluded from mineral distribution maps derived from near-infrared and thermal infrared spectrometers on orbiting spacecraft. The goal of this project is to better characterize the mineralogy of the underlying substrate within the classically dusty regions of Mars by identifying and analyzing small areas within those regions that are relatively free of dust cover. By assessing the mineralogy of the bedrock and sand deposits exposed by these “windows” through the dust, this work can provide a more complete understanding of the composition of dust-covered regions on Mars and further constrain the evolution of the martian surface.

BACKGROUND

Near-IR and Thermal- IR Remote Sensing of the Martian Surface

A wealth of studies in the preceding two decades has contributed to the current understanding of Mars' general surface composition. For example, surface emissivity data from the Thermal Emission Spectrometer (TES) aboard Mars Global Surveyor (MGS) were used to identify two general lithologies (Bandfield *et al.*, 2000). Surface type 1 (ST1), detected mostly in the heavily cratered southern highlands, is inferred to be compositionally similar to a terrestrial flood basalt while surface type 2 (ST2), found in both hemispheres but predominantly in the younger northern lowlands, is comparatively more silica-rich. ST2 was initially thought to consist of basaltic andesite to andesite (Bandfield *et al.*, 2000) or weathered basalt, which implies substantial potential input from smectite clays (Wyatt and McSween, 2002). Subsequent studies have largely ruled out the clay hypothesis, however (Michalski *et al.*, 2004; Ruff and Christensen, 2007). More recently, the silica-rich component of the ST2 lithology has been hypothesized to be widespread weathered iron-bearing glass deposits (Horgan and Bell, 2012). Rogers and Christensen (2007) further discriminated compositions of low albedo regions using TES data. Eleven distinct spectral shapes were identified among these regions, which were then grouped into four spectral classes based on common modal mineralogy.

The Observatoire pour la Mineralogie, l'Eau, les Glaces et l'Activité (OMEGA) instrument on the Mars Express spacecraft identified the presence of high- and low-calcium pyroxene (HCP and LCP) and olivine in low albedo regions of Mars using near-infrared (NIR) reflectance spectroscopy (*e.g.* Bibring *et al.*, 2005; Mustard *et al.*, 2005).

HCP is inferred to be most commonly associated with dark Hesperian-aged volcanic terrain, sand dunes, and crater ejecta, especially in the southern hemisphere. LCP is less prevalent on the martian surface, but the highest concentrations are located in highly-cratered Noachian terrain. Olivine was found to be primarily localized to areas where older crust has been exposed at the surface, including cratered terrain and impact basins. Olivine has also been detected as in-place layered rock in the walls of Nili Fossae (Hamilton and Christensen, 2005; Mustard, 2007) and as bedrock outcrops and dikes in Valles Marineris (Edwards *et al.*, 2008; Flahaut *et al.*, 2011).

Dust Mantling

Despite the numerous mineralogical and petrological studies of the martian surface, extensive regions remained uncharacterized due to dust mantling. The spectral flattening effect of bright dust limited the TES compositional study conducted by Bandfield *et al.* (2000) to the low-albedo regions of Mars, which cover only about half of the planet's total surface area. An additional global TES mineralogical study found that bright dust-covered regions were strongly associated with anomalously high RMS errors, representing greater uncertainty in estimated modal abundances of minerals (Bandfield, 2002, Christensen *et al.*, 2008). OMEGA mineralogical studies faced a similar problem: spectral signatures indicative of mafic mineralogy were observed to be weak to absent due to the presence of surface dust (*e.g.* Mustard *et al.*, 2005; Bibring *et al.*, 2006; Bell *et al.*, 2008).

The presence of widespread dust on the martian surface has been recognized since the first spacecraft-based observations of Mars. Infrared radiometry data from Mariner 9 and the Infrared Thermal Mapper (IRTM) aboard Viking Orbiter revealed a strong anticorrelation between albedo and particle size (Kieffer *et al.*, 1973, 1977). The high thermal inertia values measured by IRTM suggested that these regions were covered with dust-sized particles. Christensen (1986) characterized the ubiquitous dust cover using thermal measurements from IRTM along with data from the Viking Landers. Arabia, Elysium, and Tharsis were observed to have thermal inertias of $\sim 2\text{-}3 \text{ J m}^{-2} \text{ sec}^{-1/2} \text{ K}^{-1}$ (compared to an average value of ~ 30 for rock), which suggests that the uppermost surface layer consists of very fine particles less than $40 \mu\text{m}$ in diameter. Thermal, radar, and visible images constrain the thickness of this dust mantle to 0.1 to 2 m in the aforementioned regions (Christensen, 1986). The mineralogy of the globally homogenous dust is thought to consist primarily of palagonitic basalt and nanophase ferric oxides with a significant plagioclase component (*e.g.*, Bell *et al.*, 2000; McSween and Keil, 2000; Ruff and Christensen, 2002; Bandfield and Smith, 2003). Johnson *et al.* (2002) coated basaltic rocks with a martian dust approximate in the laboratory and measured the resulting effects on thermal infrared spectra, demonstrating that spectral features diminish substantially after a 10 to $20 \mu\text{m}$ thick layer has accumulated.

The goal of this study is to infer the substrate (potentially bedrock) mineralogy of bright dust-covered regions that have largely been ignored due to the spectral masking effects of dust. While previous studies have demonstrated that broad regional-scale mineralogical surveys of bright surfaces return spectrally bland results with high RMS

error, this work identifies small localized areas within these regions that are relatively free of dust cover. These areas can serve as “windows” through the bright dust, allowing for the analysis of the underlying bedrock mineralogy or locally-derived sand that has been exposed. If many of these dust-free surfaces are analyzed over a broad spatial distribution, more confident mineralogical characterizations of the bedrock beneath classical bright regions on Mars can be made, from the sub-kilometer scale up to the regional scale.

METHODOLOGY

Identification and Characterization of Dust-free Surfaces

Dust Cover Index. Gaps in the dust cover were identified using a number of remote sensing tools collectively. The first is the Dust Cover Index (DCI) developed by Ruff and Christensen (2002). The DCI uses TES surface emissivity in the 1350 to 1400 cm^{-1} wavenumber region (~ 7.1 to 7.4 μm wavelength) as a proxy for dust cover. Interference from atmospheric effects is minimal within this particular spectral range, and thus the particle size of silicate minerals is the dominating contributor to variations in emissivity between high and low-albedo regions. Assuming that the bright dust cover is responsible for producing the high-albedo regions on Mars, and that the Martian surface is compositionally dominated by silicates, the 1350 to 1400 cm^{-1} emissivity may be used to determine both the spatial extent and the relative amount of dust cover.

TES spectra with data constraints matching those of the DCI were projected onto a global map in the Java Mission-planning and Analysis for Remote Sensing (JMARS) software (Christensen *et al.*, 2009). These constraints only include spectra taken during daytime hours within the mapping phase of the mission, with minimal dust and ice opacity in the atmosphere. A complete list of DCI constraints is provided in Table 1. To prevent bright areas from being classified, an additional constraint on maximum Lambertian albedo (<0.20) was added. Any location covered with TES pixels that satisfied both the DCI and the additional albedo constraint was tabulated for further analysis. Figure 1 shows Williams Crater, an example of a dust-free surface identified using the DCI and one that will be further discussed in subsequent sections of this work.

Table 1

List of TES Dust Cover Index quality fields

| Quality field | Value | Explanation |
|-----------------|--------------|---|
| Algor_risk | 0 | Low risk of algor phase inversions in the spectral data |
| Det_mask | 7 | Spectral data from the six detectors are downlinked as individual spectra, rather than being co-added |
| Emission | 0 – 3.0 | Emission angle (degrees), where 0° is nadir |
| Incidence | 0 – 80 | Solar incidence angle (degrees). This range corresponds to daytime observations. |
| Lambert_alb | 0 – 0.2 | Lambertian albedo. For some areas of interest, the maximum allowed albedo was increased to no more than 0.25 in order to allow a workable number of spectra past the constraints. |
| ock | 1563 – 26183 | Includes orbits from the start of the TES mapping phase until the end of the mission |
| Phase_inversion | 0 | Data does not contain major phase inversions |
| Scan_len | 1 | Data contains only single-length scans (10 cm ⁻¹ wavenumber spacing) |
| Spectral_mask | 0 | Spectral data containing all wavelength bands are used |
| Target_temp | 250 – 300 | Derived temperature of the observed target |
| Tot_dust | 0 – 0.3 | Dust opacity at ~9 μm |
| Tot_ice | 0 – 0.07 | Ice opacity at ~11 μm |

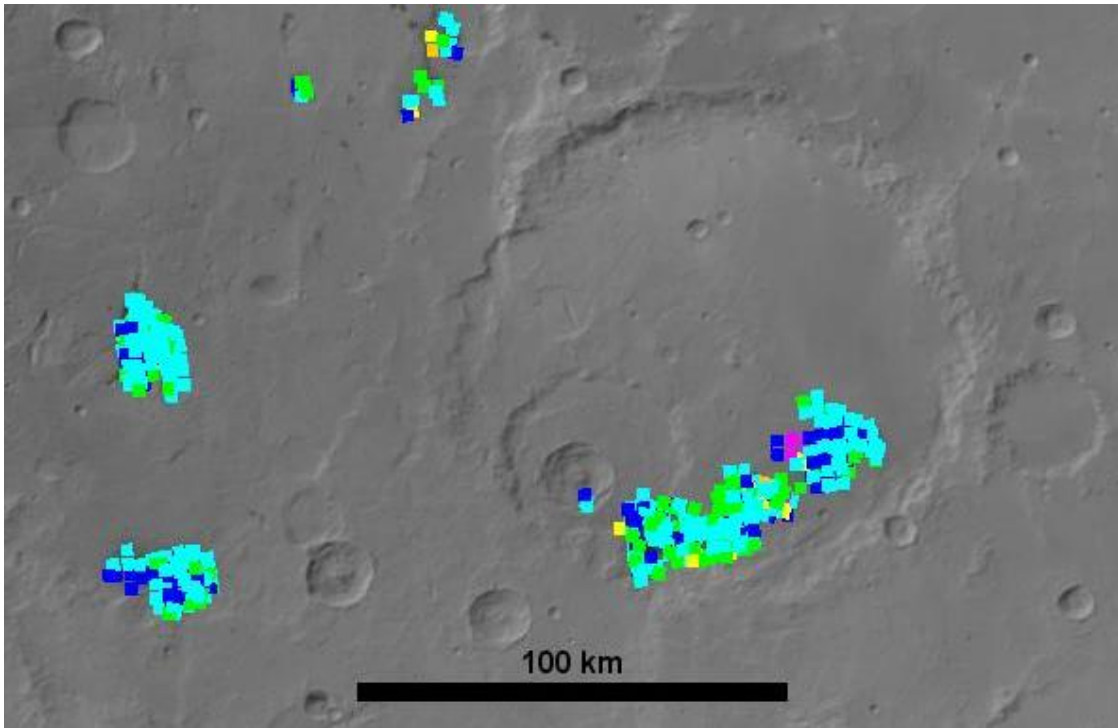


Figure 1. Thermal Emission Spectrometer (TES) spectra flagged as having low dust cover by the Dust Cover Index (DCI) in and around Williams Crater (18.3°S, 196°E). Background image is a global Mars Orbiter Camera (MOC) mosaic. Image credit: NASA/JPL/ASU

MARCI. Data from the Mars Reconnaissance Orbiter (MRO) Mars Color Imager (MARCI) were used to look for instances where bright dust had been removed from the surface to expose the darker underlying substrate. MARCI is a color imaging camera that captures wide-angle multispectral images at 1 to 10 km/pixel resolution (Malin *et al.*, 2008; Bell *et al.*, 2009). MARCI has made repeated planet-wide observations for most of the past five martian years, which is ideal for identifying holes in the dust cover that exist for only short time scales.

Individual MARCI images from the same time frame (within 20° of L_S^*) were mosaicked by region into quadrangles (Wellington and Bell, 2013). This process resulted in more than 60 region-wide mosaics for each quadrangle, spanning from the start of the MARCI science mission in 2005 to the present day. These sequences allowed for easy identification of locations that underwent a substantial decrease in albedo and flag them as potential windows through the dust. Figure 2 shows an example of a darkening event that occurred on Arsia Mons over a period of $\sim 60^\circ L_S$ during the beginning of spring of Mars Year (M.Y.) 29.[†]

This study is not intended to be a complete survey of dust-free “windows” on Mars. The DCI and MARCI methods were used to target as wide of a spatial sampling as possible within the three classical high albedo regions of Mars. Volcanic edifices were selected with particular interest. In some cases, prominent volcanoes were classified as areas of interest even when the albedo changes observed by MARCI were less discernable than usual (*e.g.*, Alba Patera and Elysium Mons). Areas of interest located

* L_S is the aerocentric longitude of the Sun, or the season on Mars. $L_S = 0^\circ$ is defined as the start of northern spring.

[†] Mars Year 1 was defined to begin in Earth time on 11 April 1955. M.Y. 29 began on 9 December 2007.

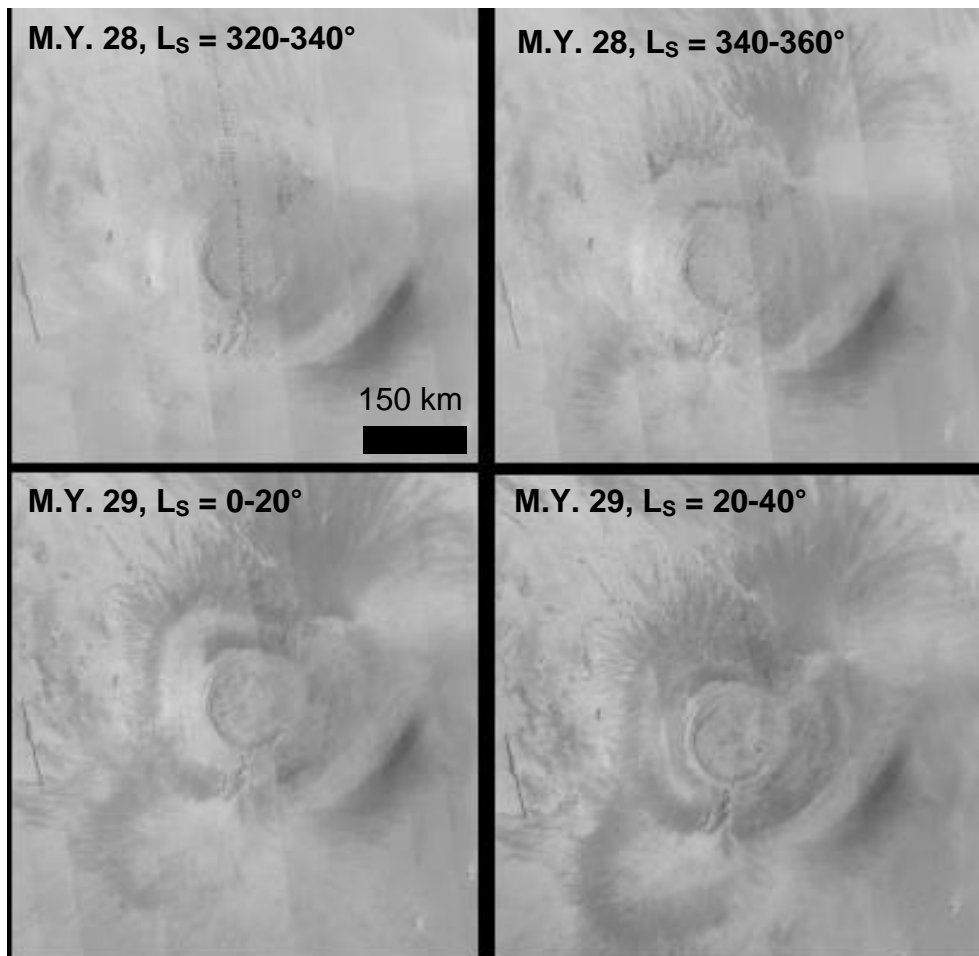


Figure 2. Successive Mars Color Imager (MARCI) mosaicked images show the darkening of the flanks of Arsia Mons over $60^\circ L_S$ during the start of spring, M.Y. 29.

towards the interiors of the great high albedo regions were favored, where the dust cover is the brightest and presumably thickest. Some areas of interest were excluded due to their close proximity and continuity with regional low-albedo features. Additionally, the landing sites of rovers that carried near-IR and thermal-IR spectrometers onboard were included: Gale Crater, the landing site of the Mars Science Laboratory mission and Curiosity rover; and Gusev Crater, the landing site of the Spirit rover of the Mars Exploration Rovers mission. Their proximity to the boundary between the large-scale low- and high albedo regions excluded them from being included in the tabulation of “windows” through the dust, but provided the rare opportunity to corroborate remote sensing interpretations to in-situ mineralogical and petrological results.

THEMIS. This study is especially interested in holes in the dust cover that expose bedrock rather than sand, which may not be representative of the local mineralogy due to the possibility of mobilization. Thus, the ability to differentiate between holes in the dust cover that are located over bedrock and those overlying sediment is required. For this purpose, the Mars Odyssey mission’s Thermal Emission Imaging System (THEMIS; Christensen *et al.*, 2003) night/day global map was used qualitatively to estimate the grain size of surface materials. Because geologic materials with larger particles will retain more heat at night compared to those with smaller particles, this relationship allows ratioed THEMIS night and day temperature measurements to be used as a proxy for grain size (Christensen, 1986). Relatively warm objects are interpreted to be rock while progressively cooler objects represent sand down to fine-grained dust.

Morphology. For each flagged area, high-resolution visible images were used to observe the local geomorphology. The MRO Context Camera (CTX) was the primary dataset used for morphological observations due to the instrument's nearly planet-wide coverage and 6 m/pixel spatial resolution (Malin, 2007). CTX allows for the identification of features such as sand dunes and layered bedrock, which provide important contextual information about how dark materials are expressed on the surface. These surface expressions may imply various processes for how they were exposed and whether they are representative of local bedrock or transported from another location. For example, the presence of dark sand deposits at the base of a massive scarp might imply that the sediments were locally derived from the rocks that compose the scarp face, especially if stratigraphic layers of varying brightness are visible. In such a case, the close proximity between the locations would potentially make the sediments a relatively pristine, unaltered representation of the local bedrock. Additionally, MGS Mars Orbiter Camera (MOC) mosaics are occasionally used for context images due to their global coverage (Malin and Edgett, 2001). The MRO High Resolution Imaging Science Experiment (HiRISE) has extremely high spatial resolution, but its comparatively lesser coverage of the martian surface limited the ability to make extensive use of that dataset.

The MGS Mars Orbiter Laser Altimeter (MOLA) collected altimetry data from the entirety of the martian surface (Zuber *et al.*, 1992). MOLA data provides important contextual topographic data when assessing morphology and was most commonly used to determine the presence and dimensions of topographic highs and lows that could potentially act as sources or traps for dark sediment.

Mineralogical Analysis

OMEGA. OMEGA is a hyperspectral imaging spectrometer that operates at visible and near-IR wavelengths (Bibring *et al.*, 2004). 191 channels cover the 0.36 to 2.5 μm wavelength region at 7-14 nm spectral resolution, while the images used in this study have a spatial resolution of about 1 km/pixel. NIR spectroscopy is ideal for detecting mafic minerals due to their abundance of transition elements, especially iron (Fe). In particular, pyroxene spectra exhibit diagnostic absorption bands at 0.9-1.05 μm and 1.8-2.3 μm , while olivine has three absorptions near 1 μm that overlap to produce a single broad band at 1.05 μm (*e.g.*, Adams, 1968; Adams, 1974a; Cloutis and Gaffey, 1991; Clark, 1995). These features are the result of crystal field absorptions by ferrous iron (Fe^{2+}), the most common transition element in mafic minerals (Burns, 1970).

The OMEGA dataset consisted of ~ 1 km/pixel images that were calibrated and mosaicked onto a series of quadrangles covering the entirety of the martian surface (Bell *et al.*, 2012). Once a candidate window was selected for near-IR analysis, the atmospherically-corrected OMEGA image associated with that particular location and timeframe was pulled from the quadrangle. Because OMEGA consists of two separate detectors, each operating within the visible or infrared parts of the instrument's 0.36 to 2.5 μm spectral range, the two resulting segments are often offset at the wavelength where the detectors meet. An alignment function is introduced that calculates the average of the slopes between the two data points immediately to the left and right of the detector join for every spectrum and positions the two segments such that the two points adjacent to the join are offset by the calculated average slope. Following alignment, the data were

ratioed to bright dusty pixels from within the same image in order to amplify spectral features indicative of mineralogy, continuum removed using either a polynomial or linear fit, and smoothed. A series of plots representing the various steps along this processing sequence is shown in Figure 3.

Some of the OMEGA data exhibited an artifact in the wavelength region corresponding to the join between the visible and infrared detectors positioned between channels 80 and 81. Reflectance is upturned on both sides of the detector join, which produces a peak near $0.96 \mu\text{m}$ despite the use of a detector alignment function. To address this issue, a simple correction function was introduced. This function removes the affected data points and replaces them with a straight line between the points on each side of the artifact range. An example of this artifact along with the resulting correction is shown in Figure 4.

For areas of interest identified using MARCI images, OMEGA data sets that matched the corresponding MARCI observation time were preferentially selected. In instances where time-correlated images were not available, OMEGA data that were taken from the same season as the MARCI observations were selected instead, based on the observation that many quadrangles used for this study show surface-darkening events that occur with remarkable regularity (Wellington and Bell, 2013). This phenomenon is most notable in Tharsis where much of the flanks and surrounding plains of the Tharsis Montes undergo substantial darkening beginning at approximately 340°L_S of the previous year, reach the maximum extent and intensity at 40°L_S , and diminish by 140°L_S . Previous studies have also noted the annual repeatability of meteorological events such as cloud

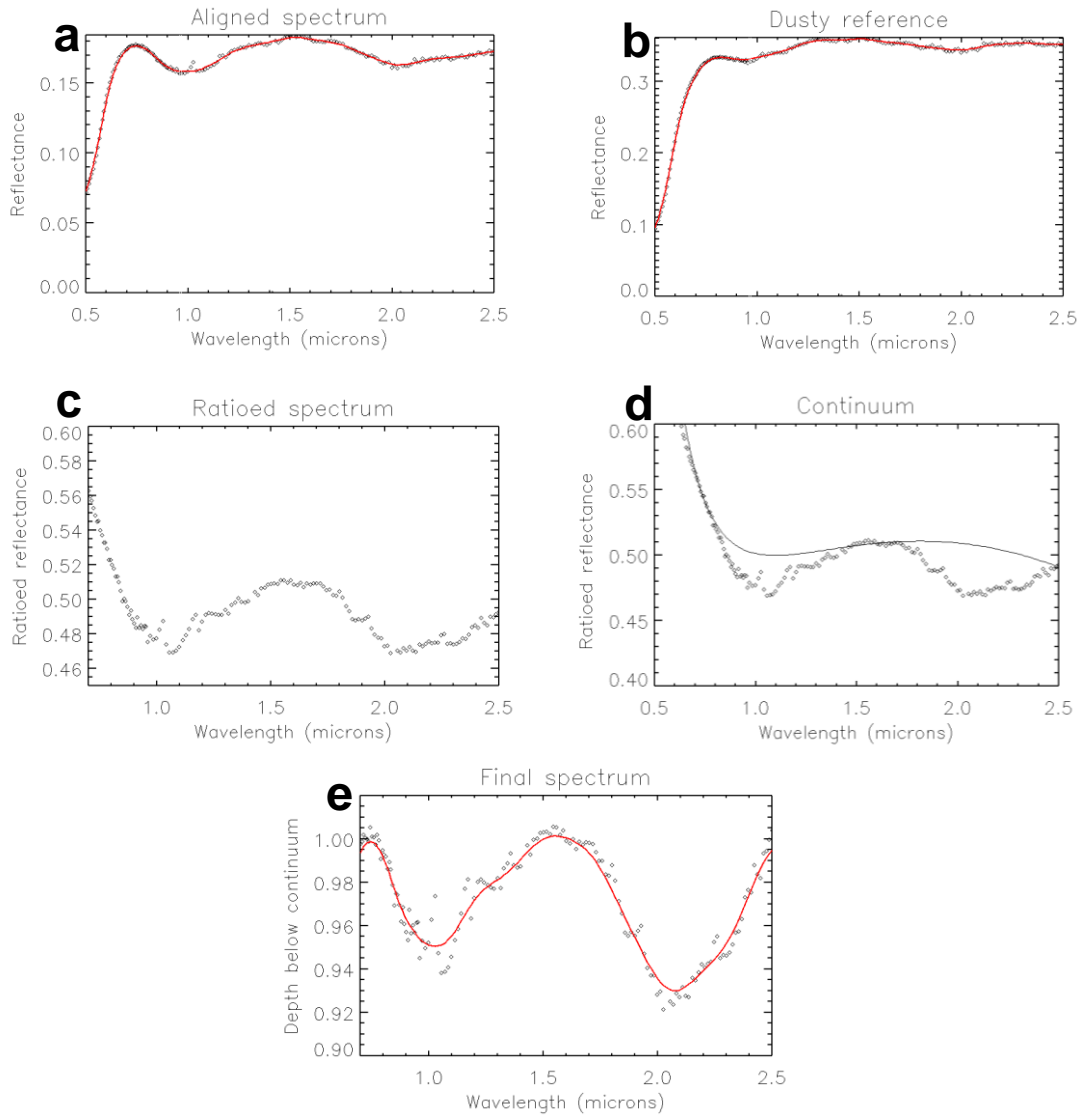


Figure 3. A series of plots showing the steps in processing OMEGA data. (a) Align the VIS and NIR channels at the detector join ($\sim 0.96 \mu\text{m}$) for the target spectrum. (b) Create an averaged spectrum representative of a bright dusty region within the same image as the area of interest. (c) Ratio the target spectrum with the dusty reference spectrum. (d) Fit a continuum to the ratioed spectrum and divide it out. (e) The final spectrum.

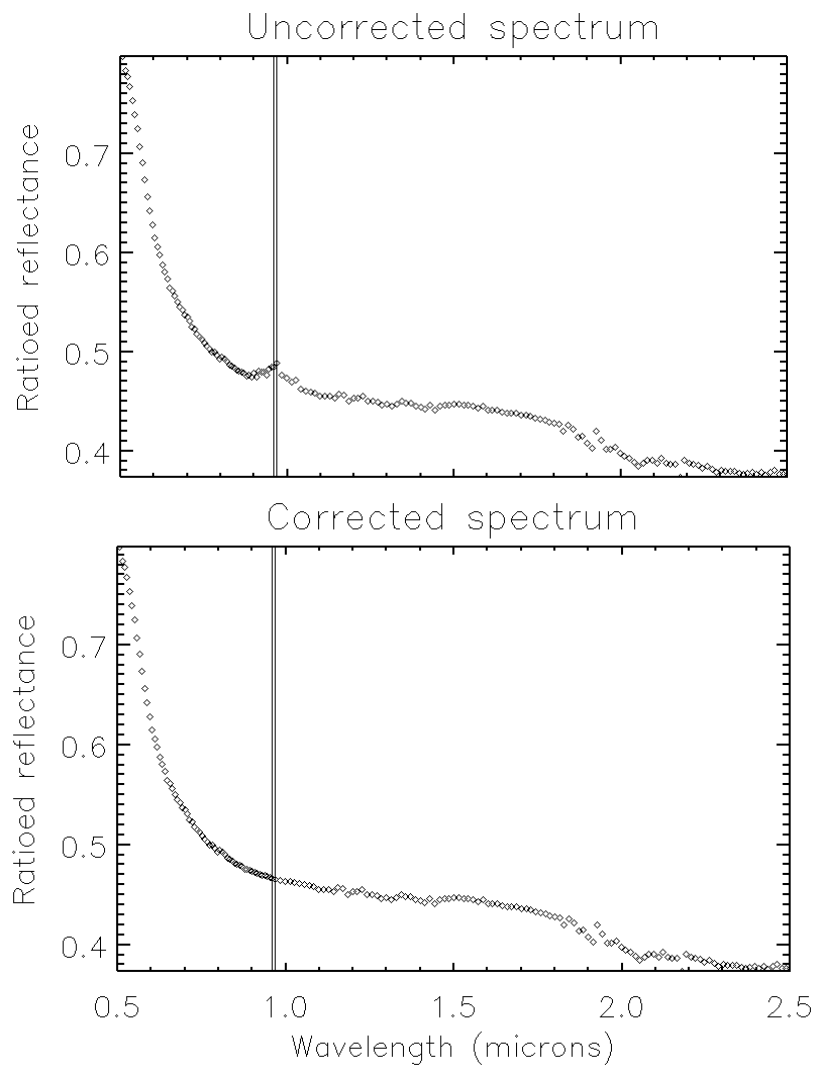


Figure 4. (top) An aligned and ratioed OMEGA spectrum from Eddie Crater exhibiting an upturn in reflectance at the detector join between the VIS and NIR regions ($\sim 0.96 \mu\text{m}$) due to an instrument artifact. (bottom) The same spectrum after artifact correction.

cover, dust storms, and dust devils over periods as narrow as $16^\circ L_S$ (*e.g.*, Cantor *et al.*, 2002).

Diagnostic spectral features were parameterized and mapped to produce mineral distribution maps. An absorption band at $1 \mu\text{m}$ is common to the classes of mafic minerals expected to occur in the martian crust, including high- and low-calcium pyroxene, olivine and iron-bearing glass. The band 1 center parameter borrowed from Horgan *et al.* (2014) is the wavelength position of the minimum of a fourth-order polynomial that is fit to the $1\text{-}\mu\text{m}$ absorption band; this formula is more accurate than simply using the wavelength position corresponding to the minimum value within the $1\text{-}\mu\text{m}$ band. The band 1 center parameter thus serves as a way to broadly identify mafic mineralogy. In the band 1 parameter maps shown in this study, only spectra that have a $1\text{-}\mu\text{m}$ band center with greater than 2% depth below the continuum are mapped. Other index parameters are then used to discriminate between mineral groups. These parameters estimate the presence of minerals by calculating band depths at the wavelength positions where they are expected to occur for a particular mineral. Identification of pyroxene is based on the presence of dual absorption bands at both 1 and $2 \mu\text{m}$. HCP and LCP can be differentiated by determining the precise location of the band centers, as increasing calcium content will shift the $1 \mu\text{m}$ band to longer wavelengths (*e.g.*, Adams, 1974a; Singer, 1981). In this study, the HCPINDEX and LCPINDEX parameters derived by Pelkey *et al.* (2007) are used to classify HCP and LCP, respectively. The olivine parameter OLINDEX2, adapted from Salvatore *et al.* (2010) detects the characteristic single broad absorption at $1 \mu\text{m}$. Weathered iron-bearing glass is identified based on the

presence of a broad, shallow 1- μm absorption located between 1.06 and 1.2 μm (*e.g.*, Adams *et al.*, 1974b; Minitti *et al.*, 2002; Horgan and Bell, 2012).

TES. Positive near-IR results from OMEGA were corroborated with TES thermal infrared data. TES contains a Fourier transform Michelson interferometer spectrometer that operates in the 1700 to 200 cm^{-1} (~6 to 50 μm) range (Christensen *et al.*, 1992, 2001). For geologic materials, spectral features within this range result from the vibrational energies of molecular bonds within the crystal lattice of a mineral (Christensen *et al.*, 1992 and references therein). This effect contrasts with the electronic crystal field absorptions of transition elements that the near-IR is sensitive to, producing an alternative physical measurement for characterizing mineralogy.

TES spectra were selected that matched with areas showing positive mineralogical signatures as revealed by OMEGA. It is also preferred that areas of interest surveyed from MARCI images are time-correlated to TES spectra; however, the very brief duration of the overlap between the two missions means that one-to-one observations are extremely limited.* Data from each instrument were therefore matched by season since dust-clearing events in these study areas tend to occur annually during the spring ($L_S = 0-60^\circ$) (Cantor *et al.*, 2002). Additionally, the same data selection constraints as those from Rogers *et al.* (2007) were applied to return the highest quality TES data. In general, these constraints allow for only relatively warm spectra taken during the TES mapping phase with limited contribution from atmospheric dust or water ice. Rogers *et al.* (2007) and similar TES-based global compositional studies were

* MRO/MARCI entered into Mars orbit in March 2006, while contact with Mars Odyssey/TES was lost in November 2006. The MRO primary science phase did not begin until five days after the TES mission ended.

specifically targeted at large low-albedo regions, excluding the classical bright regions that are the focus of this work. In some cases, it was necessary to increase the maximum allowed albedo from the ~0.15 value used in the aforementioned studies in order to for any spectra to pass through the data selection filters at all. In such instances, the maximum albedo was raised in 0.01 increments until TES spectra covering the area of interest were made available, up to a maximum of 0.25.

Thermal emission spectra of geologic materials can be modeled as the sum of each component mineral endmember spectrum in proportion to its areal percentage (Ramsey and Christensen, 1998). If the spectrum of each endmember is known, a linear deconvolution process can be used to unmix TES spectra and estimate the modal mineralogy. The selected spectra are first combined into a single average spectrum. Emission from the atmosphere is removed from the spectrum using an atmospheric spectral library, leaving behind the surface component only. The resulting spectrum is then deconvolved using a mineral spectral library containing 44 endmembers, which are listed in Table 2. This library is borrowed from a recent compositional study of Tyrrhena and Iapygia Terrae, which are regions in the southern highlands that have been noted for their mineralogic and morphologic diversity, and are likely representative of typical martian highlands material (Rogers and Fergason, 2011). Derived modal abundances for each mineral endmember are rounded to the nearest 5%, due to the 5 to 10% error associated with TES. Additionally, any minerals modeled at less than 5% modal abundance are grouped into a miscellaneous “Other” category.

Table 2

Spectral Library used for TES Deconvolutions

| # | Endmember | # | Endmember |
|----|-----------------------|----|------------------|
| 1 | Quartz | 23 | Olivine |
| 2 | Alkali feldspar | 24 | Olivine |
| 3 | Plagioclase | 25 | Olivine |
| 4 | Plagioclase | 26 | Olivine |
| 5 | Plagioclase | 27 | Olivine |
| 6 | Plagioclase | 28 | Olivine |
| 7 | Plagioclase | 29 | Phyllosilicate |
| 8 | Plagioclase | 30 | Phyllosilicate |
| 9 | Plagioclase | 31 | Phyllosilicate |
| 10 | Plagioclase | 32 | Phyllosilicate |
| 11 | Plagioclase | 33 | Glass |
| 12 | Plagioclase | 34 | Glass |
| 13 | Plagioclase | 35 | Amorphous silica |
| 14 | Plagioclase | 36 | Amorphous silica |
| 15 | Orthopyroxene | 37 | Zeolite |
| 16 | Orthopyroxene | 38 | Zeolite |
| 17 | Orthopyroxene | 39 | Oxide |
| 18 | Low-Ca clinopyroxene | 40 | Sulfate |
| 19 | High-Ca clinopyroxene | 41 | Sulfate |
| 20 | High-Ca clinopyroxene | 42 | Carbonate |
| 21 | High-Ca clinopyroxene | 43 | Carbonate |
| 22 | High-Ca clinopyroxene | 44 | Carbonate |

This mineralogical information, when combined with the context of how each area is spatially related to the nearest type regions for the various spectral classes, facilitates the ability to make broad inferences about the nature of bedrock within these regions. The modeled modal mineralogy of each area of interest was compared to the four compositional groups introduced in Rogers and Christensen (2007). Deconvolved TES spectra from any low-albedo surface on Mars can be classified into one of these groups based on the relative amounts of high-calcium pyroxene, low-calcium pyroxene, olivine, plagioclase, and high-silica phases present. The type areas for the groups are: Northern Acidalia - Solis (Group 1), Syrtis (Group 2), Tyrrhena - Cimmeria - Hesperia - Meridiani (Group 3), and Aonium - Mare Sirenum (Group 4).

RESULTS

Description of Areas of Interest

63 areas of interest were identified using the DCI and MARCI images and are mapped on a global albedo map of Mars in Figure 5. All three classical bright regions on Mars are represented. Arabia Terra contains the fewest number of potential dust-free “windows” tabulated in this study, and the few that are selected are associated with low-albedo intracrater deposits. The majority of the areas of interest in the Elysium Planitia region are concentrated in the plains southeast of Elysium Mons, centered near the Cerberus Fossae. The potential “windows” through the dust within Elysium general fall into two morphological varieties: those associated with intracrater low-albedo deposits and others that appear to be albedo features on the plains that persist throughout the course of a Mars Year. Several other potential “windows” through the dust are spread along the southern boundary of Elysium Planitia, straddling the northern lowlands-southern highlands dichotomy boundary. Two areas of interest that were targeted due to their status as rover landing sites, Gale and Gusev Craters, are among these “boundary” areas; the rest appear as low-albedo material at the base of kilometer-scale high cliffs. Nearly all areas of interest in the Elysium region were classified as having low surface dust by the DCI. Candidate “windows” in Tharsis were identified almost entirely using MARCI images. The three and a half Mars Years of MARCI observations used for this work revealed that nearly all of the volcanic constructs in Tharsis, as well as much of the adjacent plains, undergo substantial darkening periods that peak at 20 to 40° L_S every year. The resulting low-albedo areas are often continuous across hundreds of kilometers,

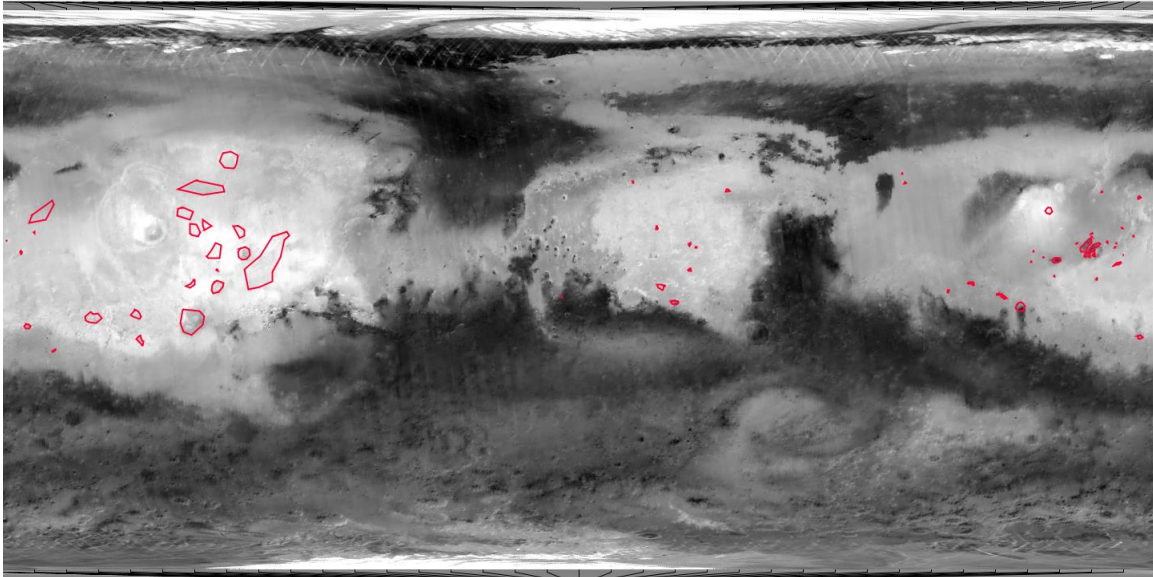


Figure 5. A TES global albedo map with the 63 candidate dust-free “windows” for this study denoted by red polygons. The large bright regions that dominate the northern hemisphere are Tharsis, Arabia Terra, and Elysium Planitia from west to east.

especially on the plains between the volcanoes. Thus, the areas of interest tabulated in Tharsis are far more extensive compared to those in Arabia Terra and Elysium Planitia.

Geologic Context

The geologic map of Mars by Skinner *et al.* (2006), a digital update and renovation of earlier maps constructed primarily using Viking Orbiter and Mariner 9 images (Scott and Tanaka, 1986; Greeley and Guest, 1987) was used to define the geologic unit and age of each area of interest. Figure 6 shows the resulting distributions for each parameter across all 63 areas. Not surprisingly, the most common units are those associated with the three classical bright regions of Mars that were targeted for this study: Arabia Terra, Elysium Planitia, and Tharsis. The extensive units corresponding to these regions are the Plateau Sequence, Elysium Formation, and Tharsis Montes Formation, respectively. The Elysium and Tharsis Montes Formations are both lava flow units that formed during the Amazonian; their fresh, broad, and unfractured surfaces are indicative of their relatively young ages. Other units of volcanic origin were also found to host areas of interest but at lesser frequency: the Alba Patera, Arcadia, and Olympus Mons Formations. The Plateau Sequence was emplaced during the Noachian and is distinguished by its heavily cratered surface and lava flow fronts (Scott and Tanaka, 1986). Many regions within the plateau sequence that host candidate windows are within the dissected unit, which is cut by channels. The lava flows of the Alba Patera, Arcadia,

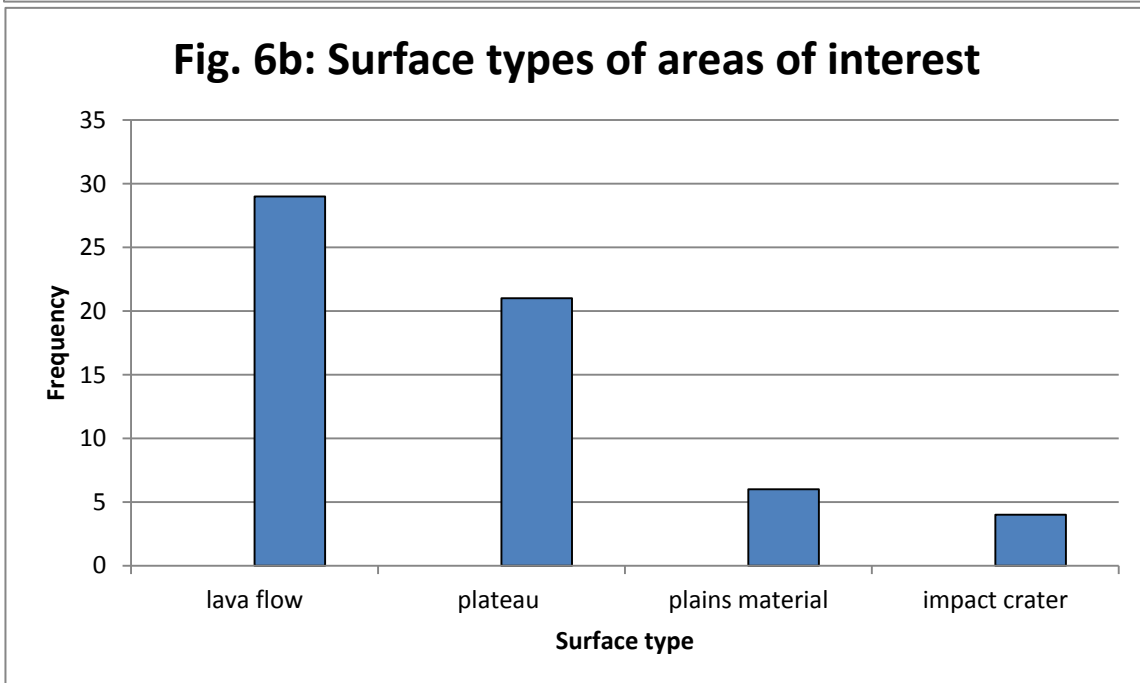
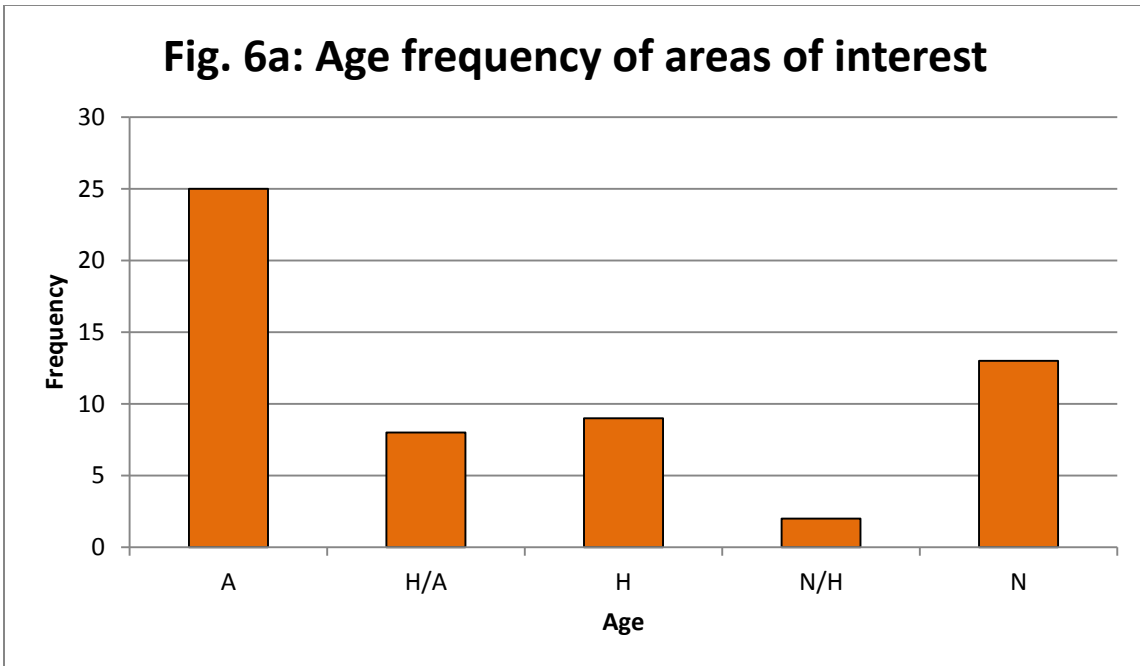


Figure 6. Graphs showing the (a) distribution of ages and (b) surface types for the 63 areas identified as candidate “windows” through the dust cover. Ages and surface type interpretations are from Scott and Tanaka (1986) and Greeley and Guest (1987).

and Olympus Mons Formations were also found to host areas of interest for this study, but at a lesser frequency.

Other map units commonly showing potential windows through the dust include the Knobby Plains and Undivided Material. The Knobby Plains are of Amazonian age and consist of mostly smooth plains interspersed with hills and knobs of erosional and possibly volcanic origin. This material makes up areas of interest in northern Arabia and Elysium. Undivided Material is of Noachian to Hesperian age and consists of closely-spaced conical hills larger than those in the Knobby Plains unit and eroded from ancient cratered terrain (Greeley and Guest, 1987). Areas of interest associated with Undivided Material are located in northeastern Arabia and the volcanic plains and southern boundary of Elysium. Apart from the general impact crater material and the depositional Vastitas Borealis Formation, no other unit was tabulated more than once.

Mineralogy

All 63 areas of interest identified as potential “windows” through the dust using the DCI and MARCI observations were analyzed using OMEGA near-IR data. Of these 63 areas, only 12 exhibited spectral features consistent with mafic mineralogy. A list of these areas is given in Table 3. All three classical bright regions of Mars are represented in this group. The OMEGA and TES data from each area of interest is discussed in detail below.

Arsia Mons. Arsia Mons is the southernmost of the Tharsis Montes. MARCI observations reveal that the flanks of the volcano, as well as some of the surrounding

Table 3.

Areas of Interest Yielding Positive Mineralogical Detections

| Name | Coordinates | Area (km²) | Type | Region | OMEGA stamp | OMEGA observation time | Geologic unit |
|----------------------|--------------------|----------------------------------|----------------|---------------|------------------------|-----------------------------------|---------------------------------------|
| Pettit Crater | 12.4N, 186.1E | 1,000 | splotch | Elysium | ORB3262_3 | MY 28, L _S 83° | impact crater |
| Cerberus west | 15.5N, 159.5E | 4,500 | plain | Elysium | ORB1445_2 | MY 27, L _S 169° | Elysium Formation |
| Cerberus crater | 11.1N, 159.3E | 7,000 | splotch/plain | Elysium | ORB3643_3 | MY 28, L _S 132° | Elysium Formation |
| Elysium crater #1 | 9.4N, 150E | 9,000 | splotch/streak | Elysium | ORB1533_3 | MY 27, L _S 183° | Elysium Formation |
| Aeolis west | 2.2N, 122.5E | 3,000 | cliff | Elysium | ORB0329_2 | MY 27, L _S 23° | Undivided Material |
| Aeolis east | 2S, 133E | 3,000 | cliff/crater | Elysium | ORB0469_3 | MY 27, L _S 42° | Undivided Material |
| Arsia Mons | 10.5S, 240.5E | 10,000 | flank | Tharsis | ORB3342_4 | MY 28, L _S 93° | Tharsis Montes Fm. |
| Williams Crater | 19S, 196E | 1,000 | splotch | Elysium | ORB1408_4 | MY 27, L _S 163° | Plateau Sequence |
| Gusev Crater | 14S, 175.5E | 500 | splotch | Elysium | ORB3328_4 | MY 28, L _S 91° | older channel and chaotic material |
| Gale Crater | 6S, 138E | 20,000 | splotch | Elysium | ORB0436_2 | MY 27, L _S 37° | Plateau Sequence |
| Arabia crater #1 | 1.2N, 26.5E | 9,500 | splotch/streak | Arabia | ORB0558_3 | MY 27, L _S 53° | Plateau Sequence |
| Arabia crater #2 | 3.5S, 30.2E | 8,000 | splotch/streak | Arabia | ORB1428_1 | MY 27, L _S 166° | Plateau Sequence |

plains, undergo substantial darkening during the last 20° L_S of M.Y. 28 and into the spring of M.Y. 29. Although smaller-scale albedo variations occur within and around these areas, the overall darkening persists until approximately L_S 140° of M.Y. 29. The darkening event repeats in M.Y. 30 and 31 and its L_S bounds exhibit remarkable similarity on an annual cycle.

The OMEGA data used in this analysis of Arsia Mons were taken on M.Y. 28, L_S 90° (product ID ORB3342_4). Although MARCI quadrangles do not cover this exact instance in time, the L_S of the observation falls well within the observed annual darkening period. The band 1 parameter maps pixels with spectra that exhibit a 1 μm band absorption greater than 2% below the continuum (for band depths less than that, spectral features cannot be confidently characterized). For Arsia Mons, the band 1 parameter map shows good spatial correlation with dark surfaces exposed during the annual major dust-clearing event (see Figure 7a). The average ratioed spectrum of the densest cluster of highlighted pixels contains two distinct absorption bands at 1 and 2 μm (band 1 and band 2), which can be seen in Figure 7c. Additionally, signatures from both the HCPINDEX and LCPINDEX parameters are weak, as seen in Figure 7b (detections above 5% abundance are rare, and none occur above 10%).

Additional OMEGA data were taken from approximately the same location on Arsia Mons at M.Y. 28, 272° L_S (product ID ORB4505_2) and are shown in Figure 8. MARCI images from this time reveal that the flanks have a higher albedo compared to the springtime observation, likely due to the presence of a thicker dust cover layer. Low-albedo areas are especially difficult to resolve during the M.Y. 28, L_S 280-300° time

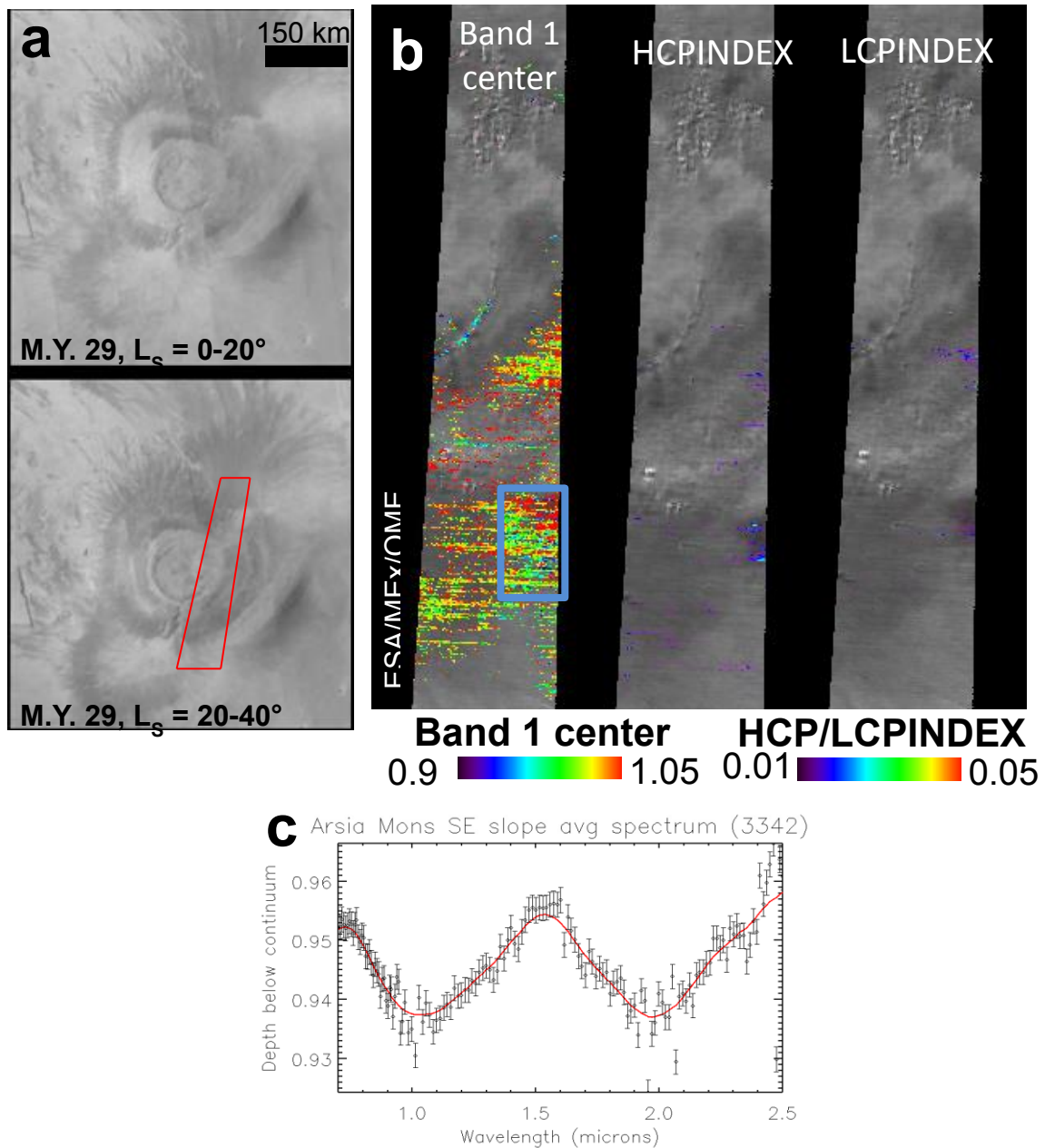


Figure 7. (a) The final two MARCI frames from Fig. 2 showing the exposure of dark material on the flanks of Arsia Mons in northern spring of M.Y. 29. The red box denotes the position of images in 7b. (b) Band 1 center, HCPINDEX, and LCPINDEX parameters from OMEGA stamp ORB3342_4 mapped on the southeastern flank of Arsia Mons. The blue box denotes the area from which spectra were averaged to produce the plot shown in 7c. (c) Averaged spectrum of the strongest cluster of band 1 center signatures on the SE flank of Arsia Mons, indicated by the blue box in 7b.

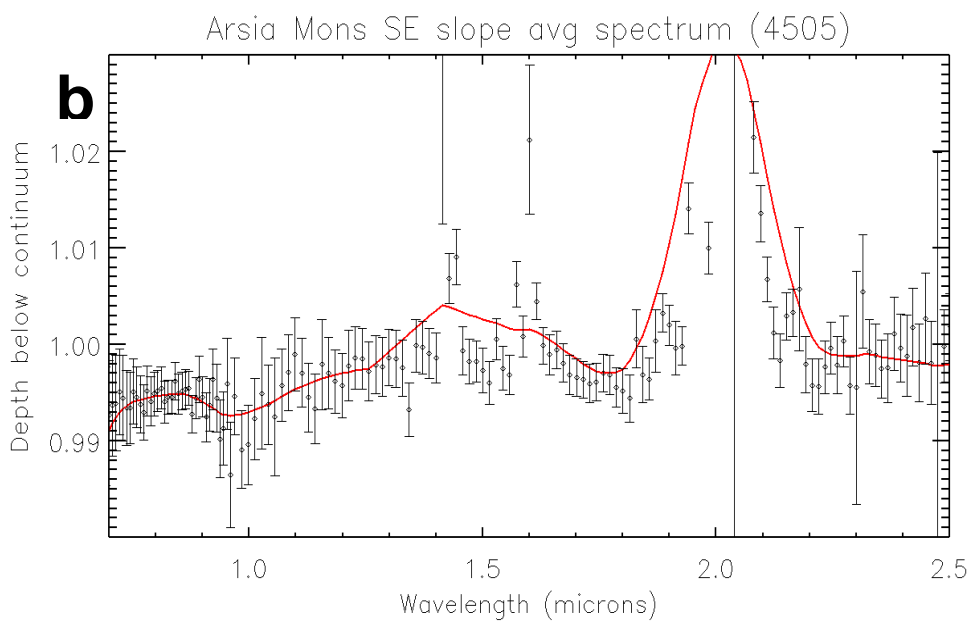
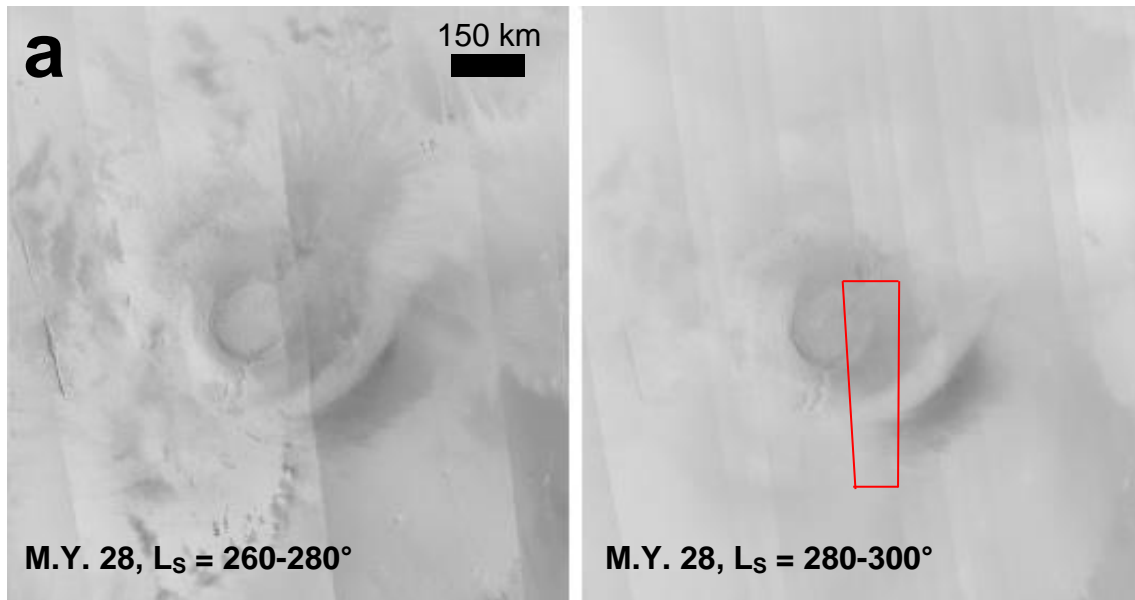


Figure 8. (a) Successive MARCI images taken of Arsia Mons during the beginning of northern winter of M.Y. 28, one of the dustiest times of the year at this location. The red box denotes the position of OMEGA stamp ORB4505_2, which is analyzed in 8b. (b) Averaged spectrum of the same location used to produce the spectrum in 7c. Note the lack of distinct absorption features at 1 and 2 μm compared to 7c, in addition to the larger error bars.

period, with the exception of the dark area in the plains just to the southeast of Arsia Mons.* The averaged spectrum of the southeastern flank of Arsia Mons following the dust-clearing event of spring M.Y. 29, shown in Figure 8b, does not exhibit the 1- μ m band absorption or the distinct spectral shape visible in Figure 7c.

No high-quality TES spectra were highlighted when applying the same selection constraints used in Rogers *et al.* (2007). Instead, the maximum allowed albedo was raised from 0.20 to 0.25, after which a number of pixels from the flanks of Arsia Mons were highlighted, primarily on the southeastern slopes and adjacent plains. TES data from orbit count clocks (ocks) 4585 and 4673 were taken at $L_S = 235^\circ$ and 240° , respectively. Although these seasons correspond to the dusty period, the TES spectra represent the highest quality data available as defined by the constraints used here.

The spectra from ock 4585 correspond to the western end of the low-albedo feature on the smooth plains immediately to the southeast of Arsia Mons. This feature remains relatively dark throughout the Martian year, even during periods when the rest of the region is ubiquitously bright due to dust cover. Spectra from ock 4673 are located on the southeastern flank itself, which corresponds to the same position as the area over which OMEGA spectra were averaged in Figure 7. The deconvolved TES spectra for both these ocks are shown in Figure 9. The flank spectrum (ock 4673) deconvolves to an estimated modal mineralogy of 35% high-silica phase, 35% feldspar, and 20% pyroxene that bears similarity to the Group 1 class from Rogers and Christensen (2007), a composition rich in high-silica phases and depleted in pyroxene that is present mostly in

* This albedo feature persists year-round, even during dusty seasons, but is not the same surface analyzed using OMEGA product ORB3342_4, which resides on the actual flank of the volcano. TES results for this feature are discussed below, but no OMEGA data from the appropriate season were available.

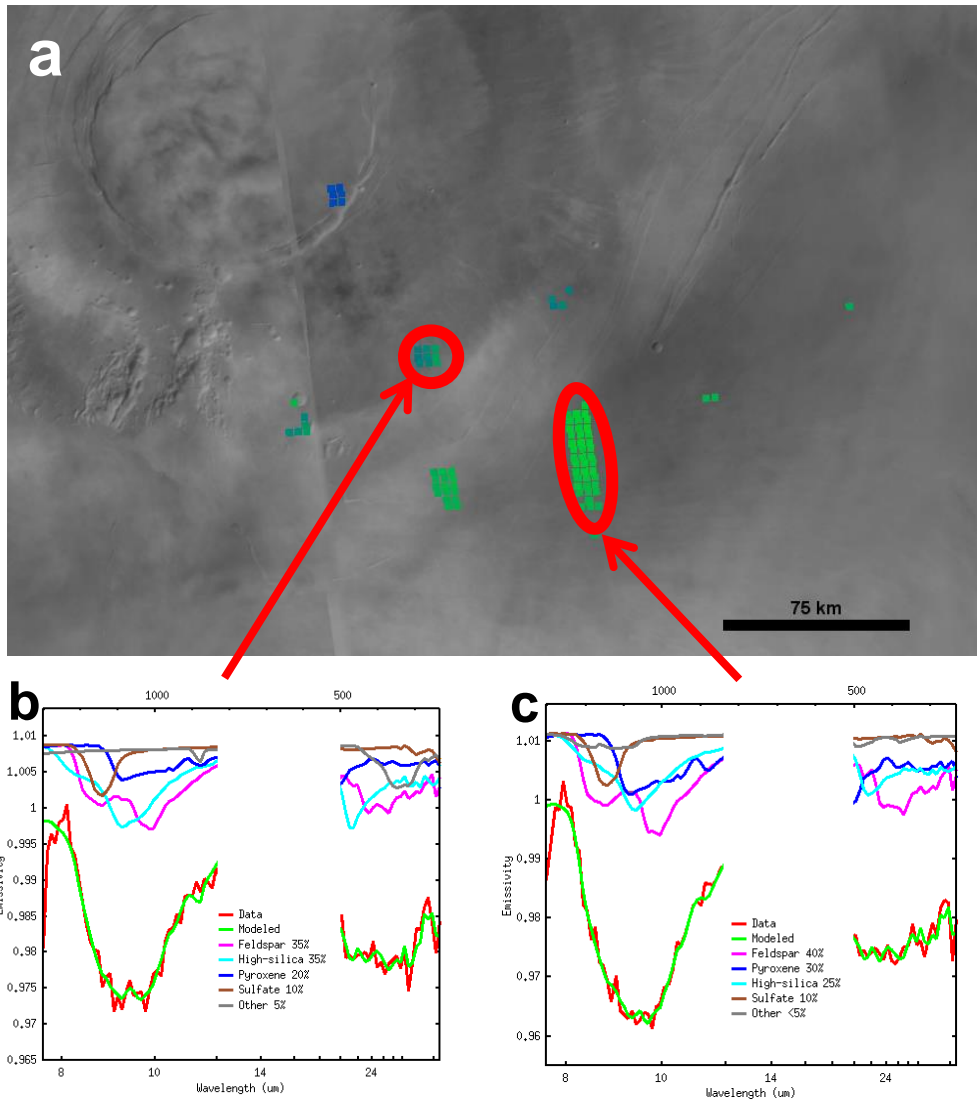


Figure 9. (a) MOC mosaic of southeastern Arsia Mons. Colored boxes are TES spectra that satisfy the quality constraints used for this study. Red ellipses denote the spectra deconvolved in 9b and 9c. (b) Deconvolution of a TES spectrum averaged from the pixels indicated in 9a. These pixels spatially coincide with the area analyzed in Fig. 7 using OMEGA data on the southeastern flank. (c) Same as 9b, but for pixels located on the plains immediately to the southeast of Arsia Mons.

the northern plains. None of the three most abundant phases (pyroxene, feldspar, and high-silica phase) differ from the defined spectral class by more than 5%, which is the typical error associated with TES data. The plains spectrum deconvolution (ock 4585) exhibits different results: the modal mineralogy of 40% feldspar, 30% pyroxene, and 25% high-silica matches best with the plagioclase-rich Group 4 composition characteristic of Aonium and Mare Sirenum. Pyroxene and feldspar concentrations are within 5% of Group 4 values, while high-silica phase is modeled at slightly higher amounts than the expected amount for Group 4 (25% versus 19%).

Other Tharsis volcanoes. Attempts were made to analyze the surface compositions of other volcanic edifices in Tharsis using the same techniques as for Arsia Mons. These locations included the flanks and surrounding plains of Alba Patera, Ascraeus Mons, Ceranius Tholus, Pavonis Mons, Tharsis Tholus, and Ulysses Tholus. All of these locations were identified as potential dust-free surfaces due to observed seasonal albedo variations from MARCI data. Although these darkening events are most prominent on the Tharsis Montes, more limited variations do exist at these smaller scales. The results of the NIR mineralogical analysis of the Tharsis region are shown in Figure 10. The 1 μm band center, the primary spectral feature used to infer bedrock mineralogy in these data, is not distinguishable in any of the spectra. All of the examples analyzed have a flat featureless spectrum with the exception of minor absorptions at 1.6 and 2.0 μm that are likely due to residual uncorrected atmospheric carbon dioxide and possibly water vapor.

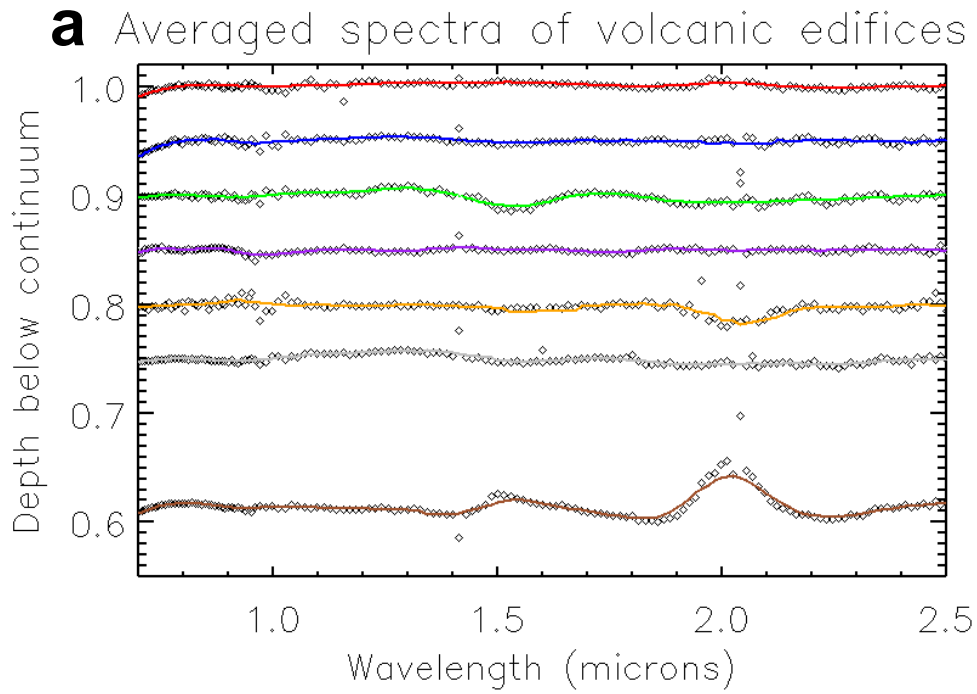


Figure 10. (a) OMEGA spectra of various surfaces associated with volcanic edifices in the Tharsis region. Each surface was flagged as potentially dust-free using MARCI images. Colors correspond to stars in (b), which denote the locations from where each spectrum was taken from.

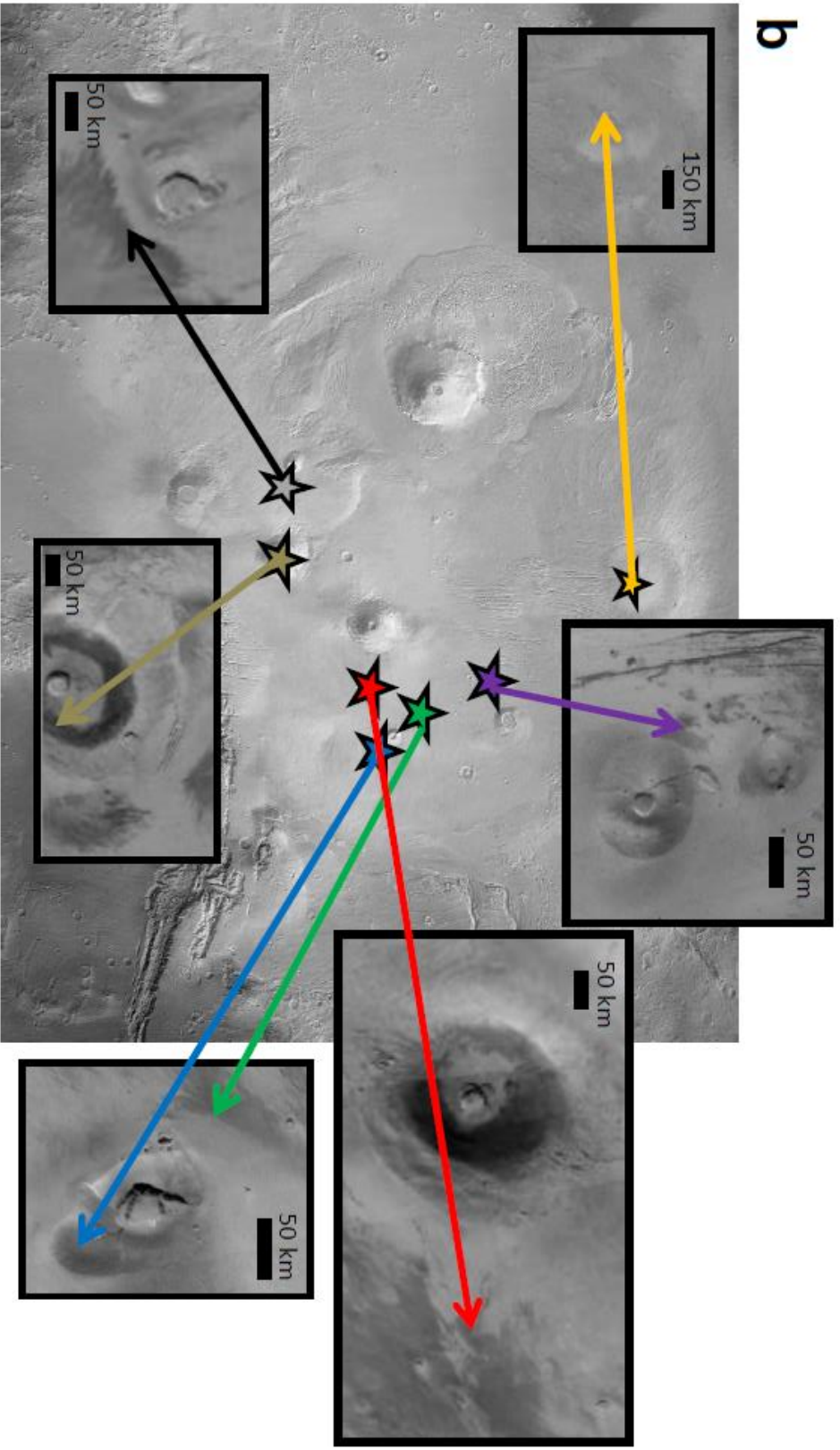


Figure 10. (b) TES albedo over MOLA elevation map of Tharsis. Insets show the MARCI observation used to identify potential dust-free surfaces.

Elysium Planitia. Most areas of interest located in the Elysium Planitia region exhibit similar OMEGA spectral features. The 1- μm bands from Aeolis west, Aeolis east, Cerberus west, Cerberus crater, Elysium crater #1, and Wiltz Crater, the primary feature used to infer mineralogy for each respective area, share similar characteristics. The most notable similarity is their shape, which appears to be a composite of three overlapping bands. The central band is typically easy to distinguish individually from the rest of the composite band and is most prominent in the averaged spectra from Aeolis west and Cerberus crater. The other two overlapping bands appear as shoulders on either side of the central band: one is located near 0.85 to 0.9 μm while the other is located in the 1.3 to 1.4 μm range. The longer-wavelength shoulder is more prevalent and is observed in all the aforementioned areas in Elysium Planitia at varying degrees. The shorter-wavelength shoulder tends to be more subtle and is not present at all in some spectra. The most apparent example of this shoulder is in the Aeolis west spectrum while, conversely, there is no such feature in the Cerberus west spectrum and the shorter-wavelength absorption edge of the 1- μm band appears linear. The wavelength position of this composite band center varies across different areas. The most common position is ~ 1.09 μm . Significant outliers are Aeolis west with a 1- μm band center beyond 1.10 μm , and Aeolis east with a 1- μm band center at 1.05 μm .

Williams Crater. Williams Crater is a ~ 120 -km diameter crater located between Elysium and Tharsis just north of the dichotomy boundary (18.5°S , 196°E). A low-albedo splotch is present along the SSW wall of the crater, which extends for about 60 km towards the northeast and becomes brighter with increasing distance (Figure 11). This

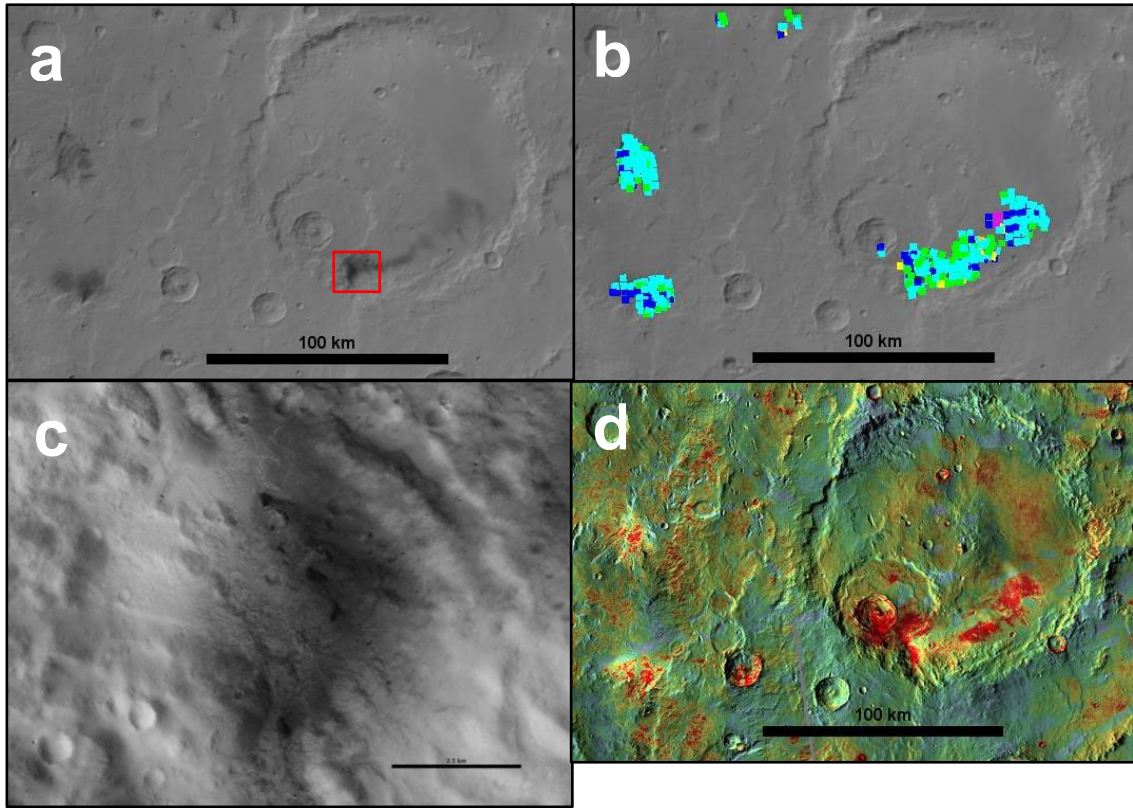


Figure 11. (a) MOC image showing the low-albedo splotch along the southern floor of Williams Crater. The red box denotes the location of Fig. 11c. (b) Colored boxes denote TES spectra classified as having low dust cover by the Dust Cover Index (DCI) in and around Williams Crater. Background image is a MOC global mosaic. (c) CTX image of the closed depression that corresponds with the lowest albedo area within Williams Crater. Scale bar is 2.5 km. (d) THEMIS night over day mosaic over the same area. Warm colors represent surfaces with higher thermal inertia, which implies a material with larger particle size.

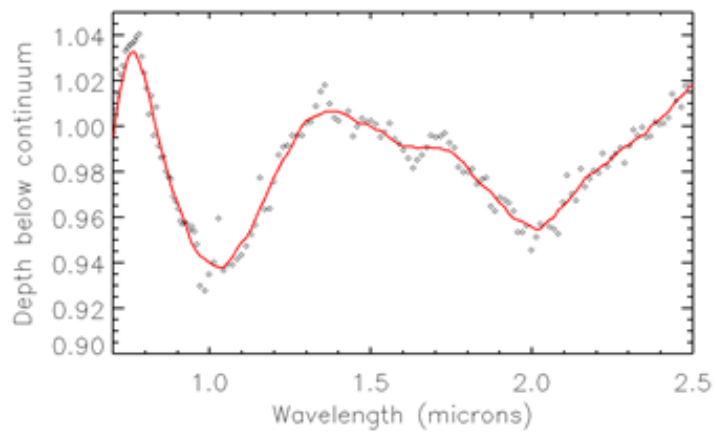
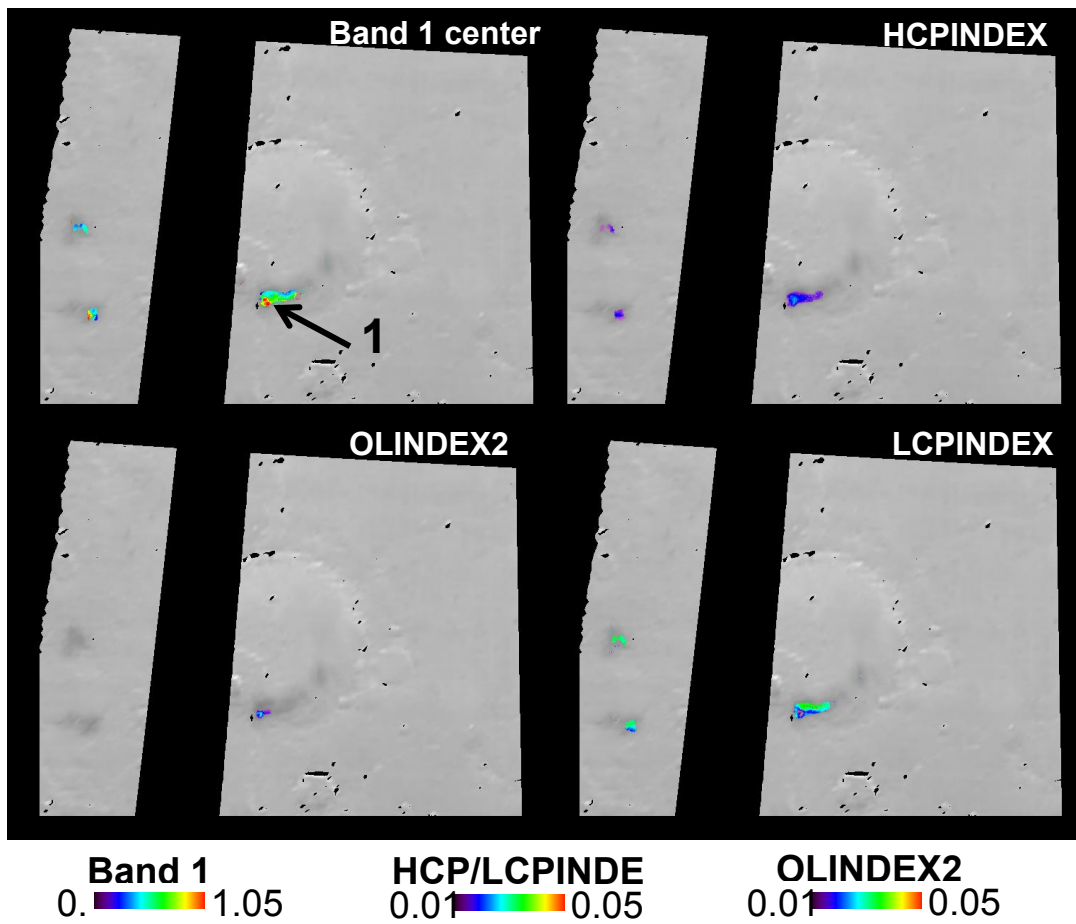


Figure 12. OMEGA mineral parameter maps for Williams Crater. Background image is a stretched OMEGA visible image. The labeled arrow in the Band 1 center map denotes the location of the CTX image shown in Fig. 11.

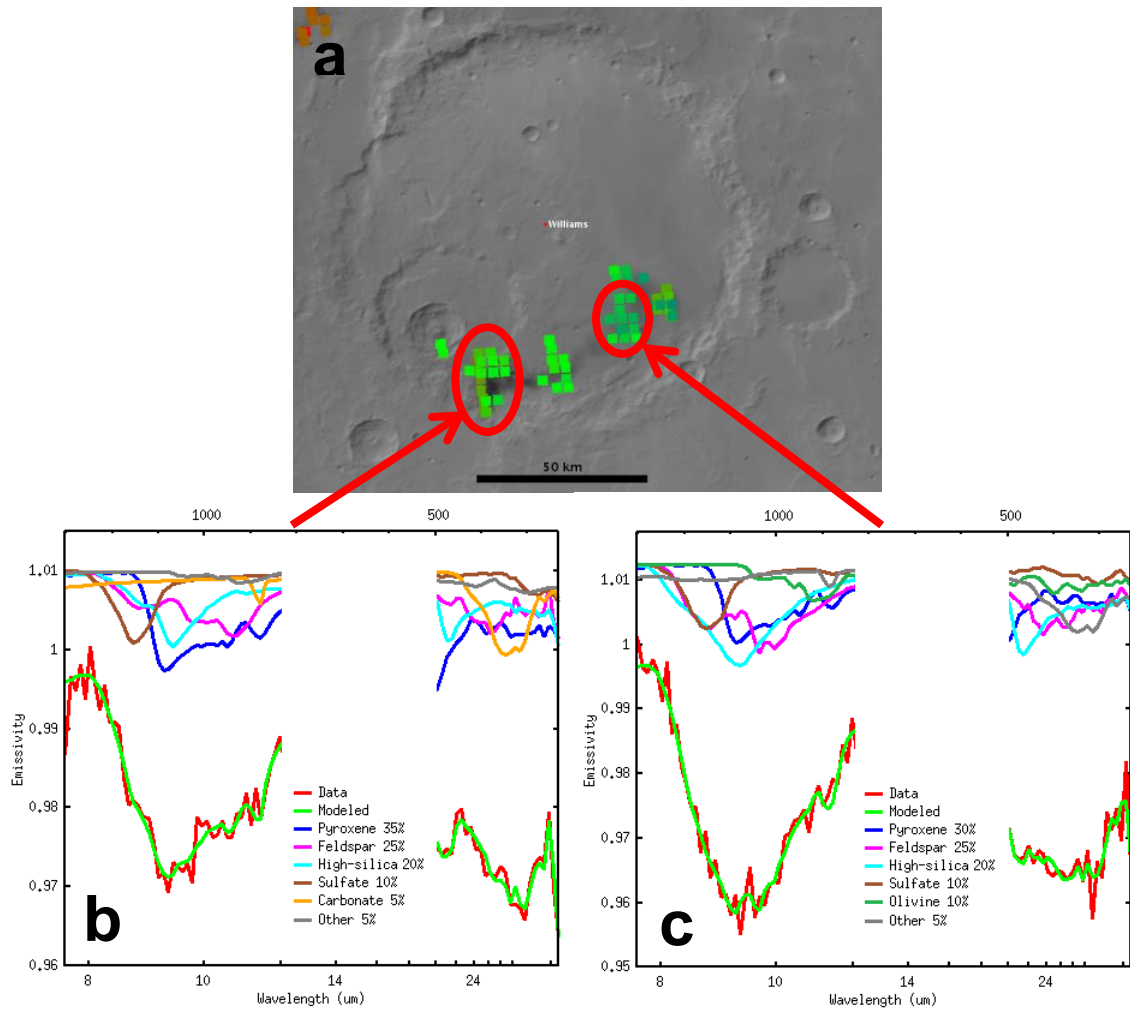


Figure 13. (a) MOC mosaic of Williams Crater (18.5°S, 196°E). Colored boxes are TES spectra that satisfy the quality constraints used for this study. Red circles denote the spectra deconvolved in 10b and 10c. (b) Deconvolution of the TES spectrum averaged from the pixels indicated in 10a, corresponding to the western end of the intracrater low-albedo splotch. (c) Same as 10b, but for pixels located on the eastern end of the splotch.

splotch was identified by the DCI as a surface with low dust cover, while the THEMIS night over day contrast global mosaic reveals that it also spatially correlates well with a high thermal inertia signature within the crater. The band 1 center, HCPINDEX, LCPINDEX, and OLINDEX2 parameters mapped in Williams Crater and the surrounding terrain are shown in Figure 12. The band 1 parameter is limited to the southernmost portion of the splotch. The band center position ranges from 0.96 to 1.02 μm with the exception of a number of pixels indicating a position of $\sim 1.05 \mu\text{m}$. CTX images and MOLA topography data reveal that these pixels correspond to a closed depression within the south crater wall (Figure 11c). The western side of the depression appears to expose layered rocky material. These layers exhibit a rugged or scalloped texture indicative of significant erosion but which appear more competent than the adjacent layers. Located along the base of the closed depression are a number of discrete dark deposits which appear to be piles of sand based on CTX image observations, the largest of which are 250 to 400 m across. No ripple morphology is visible within these localized deposits at the resolution of CTX. The walls of this closed depression may act as a local source for the dark material in Williams Crater, as evidenced by the deposits with lowest albedo being concentrated at this location and the observed diminishing of the splotch with increasing distance from the depression toward the northeast. Although this depression is a localized topographic low, an impact crater ~ 40 km in diameter within Williams Crater is only about 5 km to the north and lies at 100 m lower elevation.

Further east along the splotch in Williams Crater, the topography is more subdued. The terrain is considerably smoother in comparison to the aforementioned

closed depression, and dune forms are not visible in CTX images except on the floors of small impact craters. The overall slope of this part of the Williams Crater floor is towards the southeast. One particular low-albedo patch within the splotch is 4.5 km across and is located at 19°S, 196.1°E. Numerous dark streaks that trend NW-SE are visible within the patch. The patch occurs in a trough extending from the crater wall that is ~10 km wide at its base and slopes down toward the northeast. However, the patch does not correspond to a local topographic low within the trough; rather, it is located several kilometers upslope of where the trough flattens out to the northeast, which corresponds to an elevation difference of ~30 m.

The averaged spectrum for the closed depression is shown in Figure 12. The spectrum contains a deep, narrow absorption at ~1.05 μm and a shallower broad absorption at 2.0 μm . The maximum between the two bands is positioned near ~1.35 μm . The minor absorption at 1.6 μm is likely an effect residual atmospheric CO_2 . The band 1 parameter returns signatures from a ~30-km wide area in Williams Crater within the low-albedo splotch along the southern wall (Figure 12). While HCP detections are minor in this area overall, the highest observed parameter values (~0.02) are associated with the depression. The olivine index is strongest at this location as well, although detections overall are more limited in spatial extent. LCP is detected in slightly greater amounts than either HCP or olivine, reflected by LCPINDEX values of 0.03 to 0.04. HCP and olivine display fairly good spatial correlation within Williams Crater, most notably with peak index values overlapping with the closed depression. Although the overall spatial distribution of LCPINDEX signatures is very similar to that of the HCPINDEX,

variations in index strength within the area of detection are noticeably different. The lowest mapped LCPINDEX values occur above the closed depression, corresponding to values at or below the lower index limit. Higher LCPINDEX values are found along the northern part of the dark splotch, further away from the south crater wall. Two isolated localized depressions ~75 km to the west of Williams Crater also contain strong signatures in the band 1 parameter index and are visible in Figs. 11 and 12.

Unmixed TES spectra from the low-albedo splotch are shown in Figure 13. Spectra from ock 3090 correspond to the dark western end of the streak near the closed depression, while ock 3832 corresponds to the comparatively brighter central to eastern portion. Although the averaged spectra from each ock exhibit discernable visual differences, the derived modal mineralogy from each location is largely similar. The western spectra yield a modal mineralogy of 35% pyroxene, 25% feldspar, and 20% high-silica phases, while the spectra from the central to eastern streak exhibit 30% pyroxene, 25% feldspar, and 20% high silica-phases. The primary difference between the two results is the detection of olivine in the eastern spectra at concentrations near the TES detection limit.

Pettit Crater. Pettit Crater is a 90-km diameter crater located in central Amazonis Planitia, approximately midway between Elysium Planitia and Tharsis. Pettit hosts a large low-albedo splotch along its southwestern wall that sources a dark streak extending as far as 250 km onto the surface toward the southwest. Barchan dunes dominate the morphology of the dark floor deposits in Pettit Crater, which are evident in the CTX mosaic shown in Figure 14. The DCI classified the intracrater splotch only as a surface

with low dust cover (Figure 15a), which correlates well with a high thermal inertia unit observed in the THEMIS night over day global mosaic.

The band 1 parameter is mapped in Pettit Crater in Figure 15b. Spectra with greater than 2% band depths are localized to the low-albedo splotch and portions of the adjacent crater wall. The low-albedo deposits resting on the crater floor exhibit band 1 centers ranging from 0.94 to 0.98 μm . An averaged spectrum of these floor deposits is shown in Figure 15c. This spectrum has primary absorptions at $\sim 1 \mu\text{m}$ and 2.15 μm and a reflectance maximum between the two bands at $\sim 1.7 \mu\text{m}$. The 1- μm band center position increases to 1.05 μm along the crater wall and onto the surface streak. The HCPINDEX parameter is mapped in Figure 15c and represents the dominant mineral signature detected in Pettit Crater. The strongest signatures have near-perfect spatial correlation with the portion of the low-albedo splotch that consists of dunes. In contrast, LCPINDEX signatures are present on the dark material associated with the crater wall but the dune field is devoid of LCP detections. Olivine is detected in very minor concentrations, most notably on the lower crater wall, but no other spatial trends are observed.

TES deconvolution results from two different locations within the intracrater splotch are shown in Figure 16 and indicate a mineralogy consisting of approximately equal parts pyroxene, feldspar, and high-silica phases. Spectra from the low-albedo streak $\sim 50 \text{ km}$ to the southwest of the crater rim exhibit higher concentrations of high-silica phase ($\sim 40\%$) at the expense of pyroxene and feldspar, although it should be noted that the observed 8 to 12 μm silica absorption is noisier than those from the intracrater spectra despite the greater amount of spectra available and likely represent lower quality data.

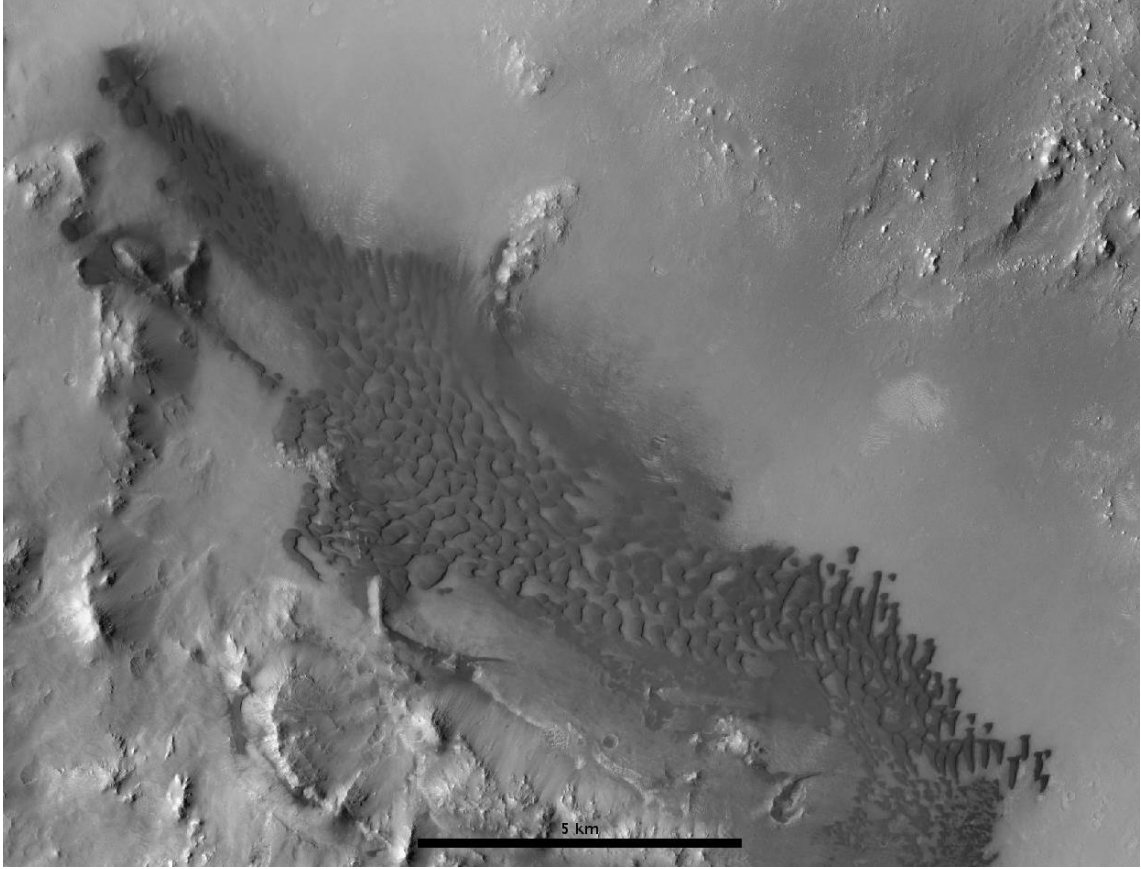


Figure 14. CTX image of the low-albedo sand deposits on the floor of Pettit Crater exhibiting dune morphology. Scale bar is 5 km.

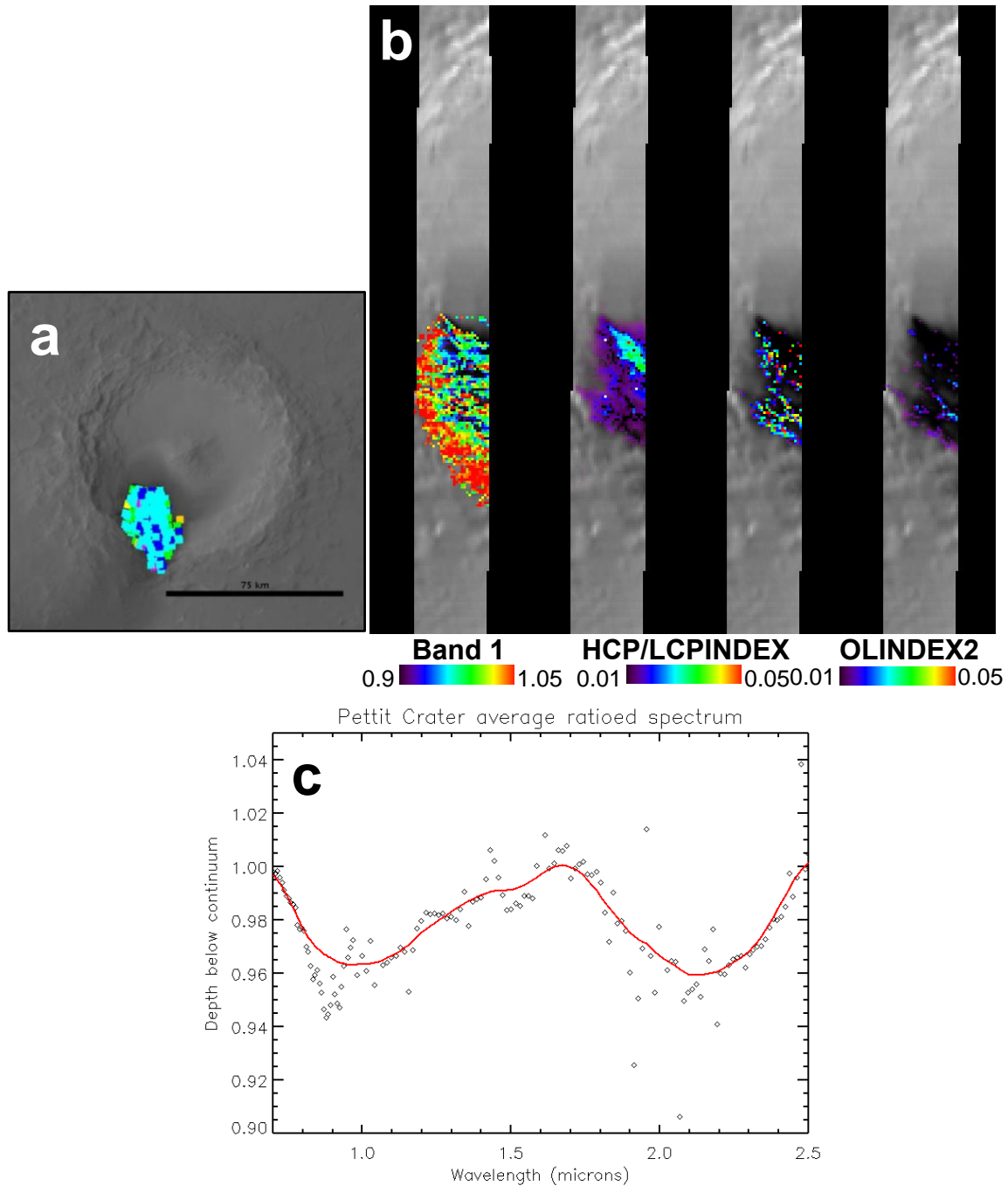


Figure 15. (a) Colored boxes denote TES spectra classified as having low dust cover by the DCI in Pettit Crater. Background image is a MOC mosaic. Scale bar is 75 km. (b) Parameter maps for the 1- μ m band center position, high-calcium pyroxene, low-calcium pyroxene, and olivine. (c) Averaged OMEGA spectrum for the low-albedo floor deposits, which correspond to shorter 1- μ m band centers.

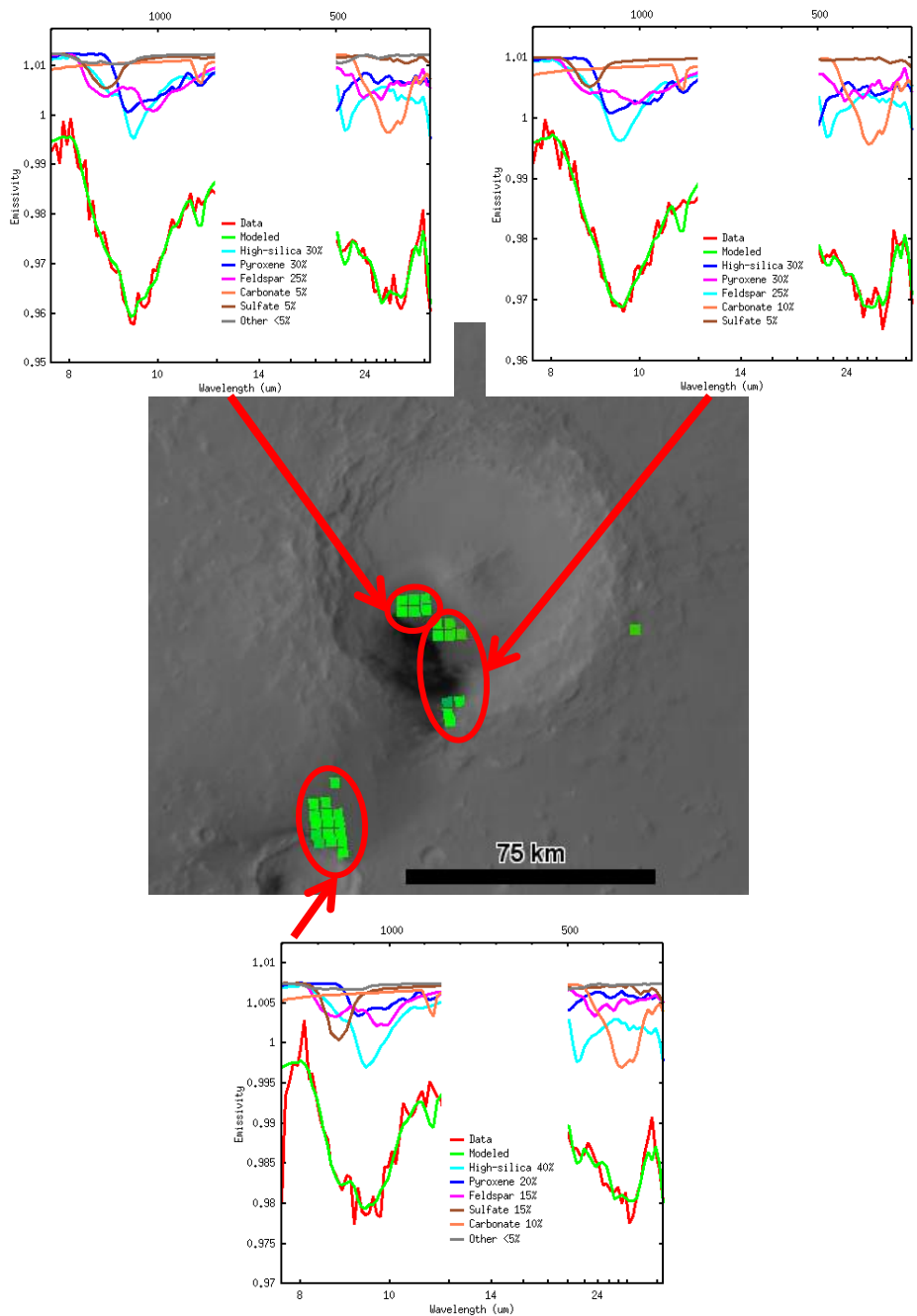


Figure 16. TES deconvolution results for Pettit Crater. The upper two plots are from the intracrater splotch while the lower plot is from the dark streak. Red ellipses denote the spectra that were averaged and unmixed to produce each plot. Background image is a MOC mosaic.

Elysium crater #1. An unnamed 50-km diameter crater in central Elysium Planitia (9.5°N, 150°E) contains a low-albedo splotch that occupies about half of the crater floor's total surface area (Figure 17). A large low-albedo streak extends to the west for ~80 km from the crater rim and is ~50 km wide. A number of smaller craters <5 km are visible within the streak; these are easily distinguishable by their own bright streaks that extend toward the southwest. A smaller isolated low-albedo area is located ~40 km further west of the end of the primary streak. The DCI classified the dark intracrater material and the entirety of the streak, including the isolated portion, as having low dust cover. MARCI images reveal that the splotch and streak remain distinctly darker than the surrounding plains throughout the entire Mars Year (Figures 17a and 17b). Although the features do brighten during the dusty period of the northern hemisphere corresponding to late autumn to early winter, there is enough contrast with the bright plains such that the splotch and streak are clearly apparent year-round. The albedo of the western isolated area is much more variable and is occasionally indistinguishable from the brighter surrounding plains.

OMEGA data from the Elysium crater #1 streak (ORB1533_3) are shown in Figure 18. The averaged spectrum from the east-central portion of the streak is dominated by absorption features at 1 and 2 μm that are characteristic of pyroxene. The 1- μm feature is centered at ~1.05 with corresponding reflectance maxima at 0.75 and 1.7 μm . This absorption band is asymmetric; the area to the right of the band center is noticeably larger than that at shorter wavelengths. Much of this asymmetry can be attributed to a minor absorption at ~1.5 μm that appears as a shoulder on the right edge of the band. The 2- μm

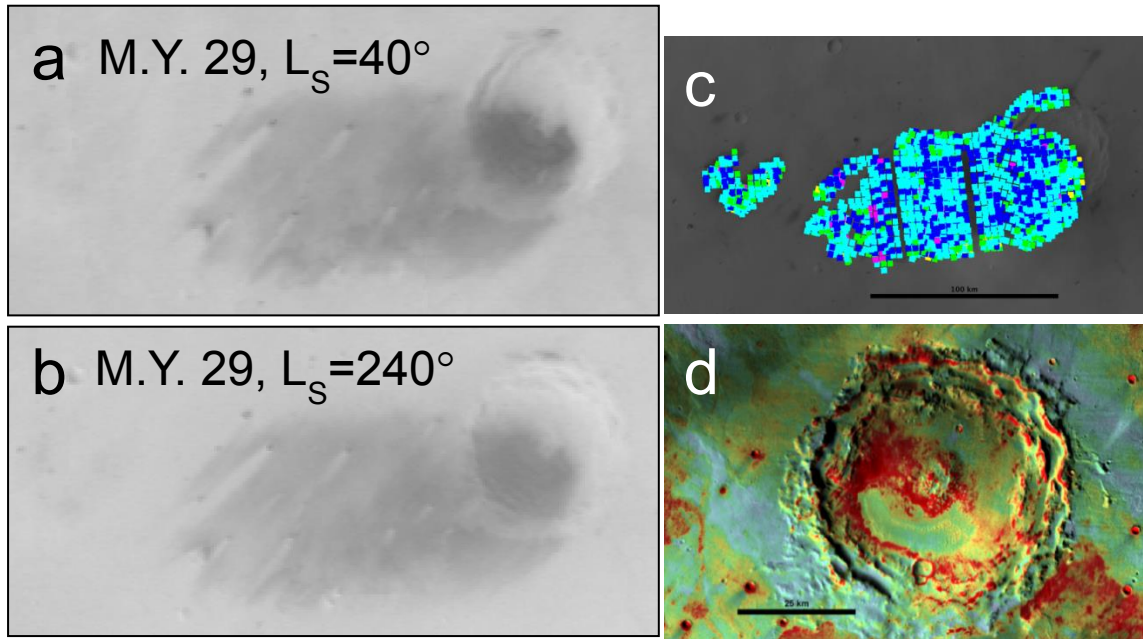


Figure 17. (a) MARCI mosaic of an unnamed crater in Elysium Planitia (9.5°N , 150°E) during spring in the northern hemisphere. (b) The same observation area as 15a, but during the peak of the dusty period in the northern hemisphere. Note that the low-albedo features in 15a are still visible during the dusty season. (c) Colored boxes denote TES spectra classified as having low dust cover by the Dust Cover Index (DCI) in and around Williams Crater. Background image is a MOC mosaic. Scale bar is 100 km. (d) THEMIS night over day mosaic of Williams Crater. Warm colors represent surfaces with higher thermal inertia, which implies a material with larger particle size. Scale bar is 25 km.

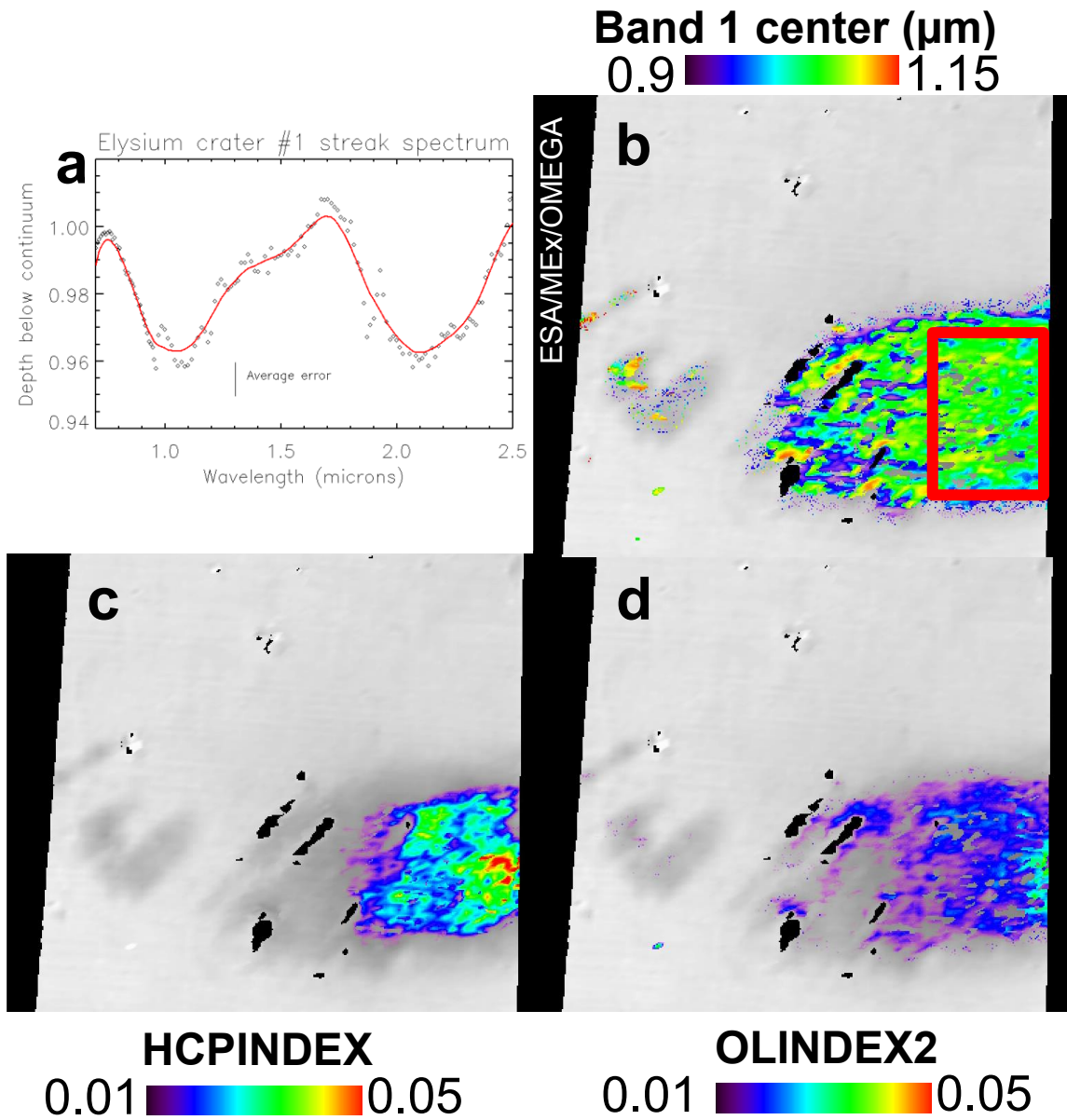
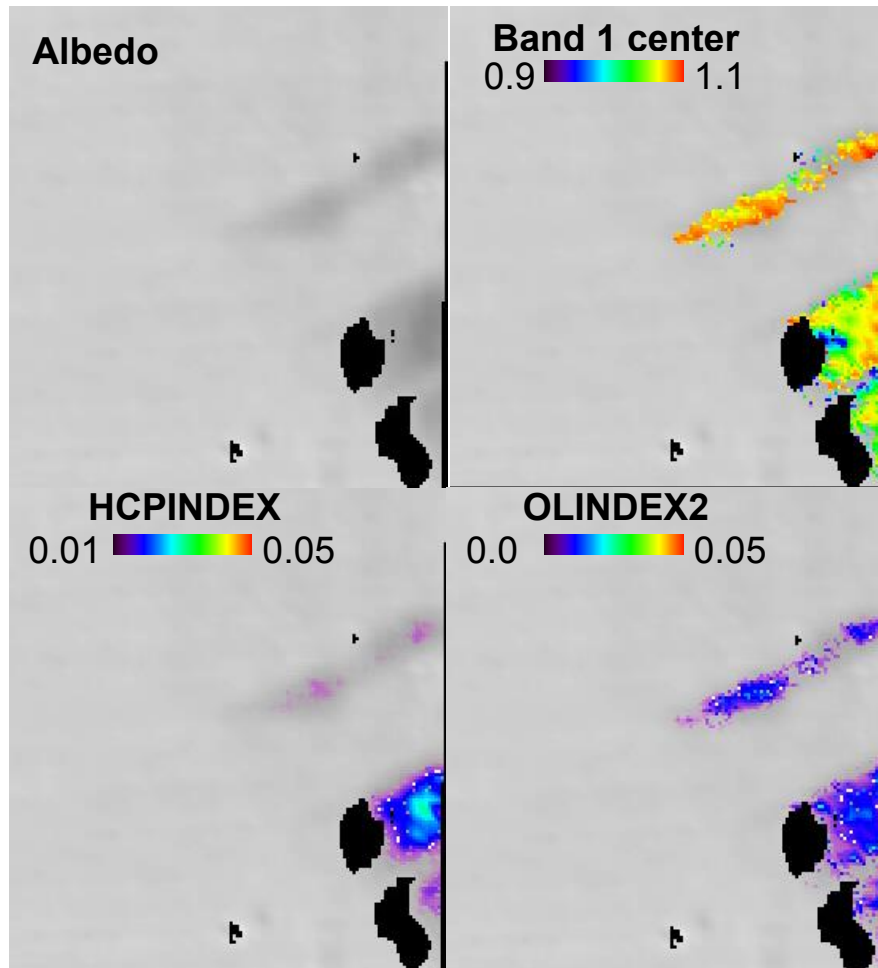


Figure 18. (a) Averaged OMEGA spectrum for the central low-albedo streak of Elysium crater #1, marked by the red box in 18b. (b-d) Index parameters for the 1- μm band center position, high-calcium pyroxene, and olivine. The red box in 18b indicates the area from which the spectrum in was calculated from.

feature is a broad, symmetrical absorption band centered at 2.1 μm with maxima at 1.7 and 2.5 μm . This band is has roughly the same depth as the 1- μm feature.

Parameters maps for Elysium crater #1 are shown in Figure 18b-d. The band 1 center index shows signatures over the entirety of the streak, with the exception of the isolated low-albedo region to the west. ~ 1.05 μm band centers dominate the eastern part of the streak. Spectra from the western end display a higher diversity of 1- μm band centers, generally ranging from 0.95 to 1.05 μm . Smaller occurrences of >1.10 μm band centers are present in the western half of the streak as well; these tend to be located in close proximity to the north to northwestern rims of impact craters. The HCPINDEX parameter has signatures in the eastern half of the streak only. The greatest concentrations of HCP appear in discrete pockets ~ 20 km across. Olivine parameter values appear to be highest within the crater and diminish with increasing distance westward along the streak. OLINDEX2 signatures are primarily localized to the eastern streak with the exception of two very minor occurrences surrounding the northern rim of impact craters. The greatest signatures within the streak are on the eastern edge of image ORB1533_3, in close proximity to the crater itself. No LCPINDEX signatures were observed.

Part of the isolated dark deposits located to the west of the Elysium crater #1 streak are analyzed in Figure 19 using data from ORB0371_3. The band 1 center parameter shows signatures that spatially correlate with dark surfaces revealed in the OMEGA visible image. The typical 1- μm band center position for this area is ~ 1.1 μm . Two localized areas with apparent lower-wavelength band centers are visible in the parameter map. These areas correspond to a pair of ~ 1.5 -km diameter impact craters



Elysium crater #1 western streak

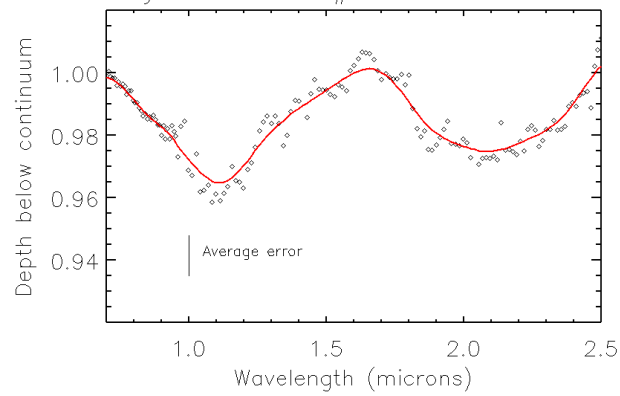


Figure 19. (a) OMEGA parameter maps and averaged spectrum of the isolated intermittent low-albedo area to the west of Elysium crater #1 seen in Figs. 17 and 18.

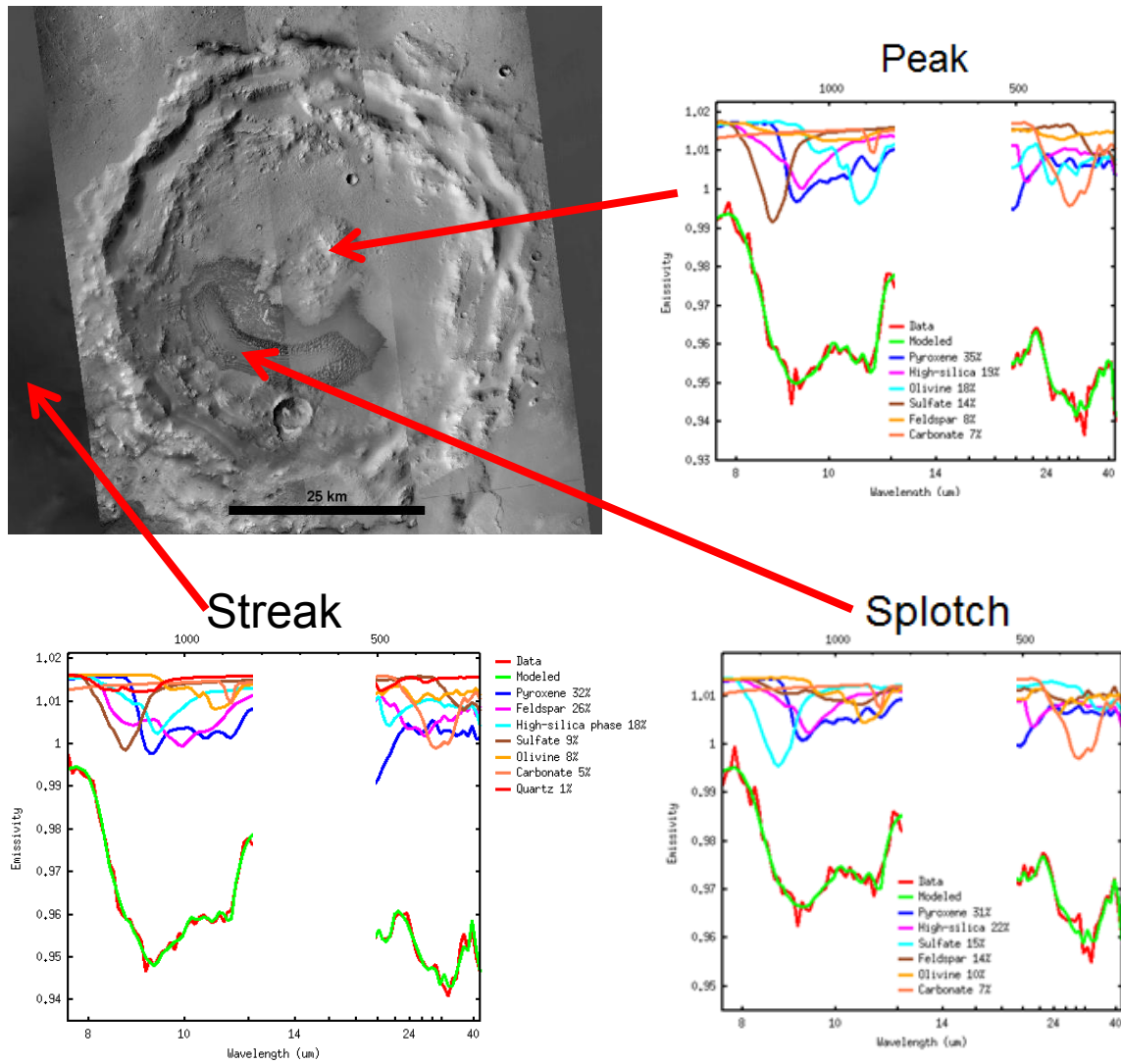


Figure 20. At upper left is a CTX mosaic of Elysium crater #1. Plots are deconvolved TES spectra from various locations in and around the crater. The “Streak” plot comes from the central streak to the west of the CTX mosaic, spatially coincident with the area over which OMEGA spectra were averaged in 17a. “Peak” corresponds to the central peak of the crater. “Splotch” corresponds to the dark splotch.

within the low-albedo deposits and their bright wind streaks. Their spectra are noisier and have 1- μm band depths barely meeting the 2% qualification, which may be a result of dust accumulation within the streak. Both HCPINDEX and OLINDEX2 signatures are distributed throughout the low-albedo deposits but are uniformly below 3% index values.

TES unmixing results from Elysium crater #1 are congruent with the mineral distribution trends observed in the OMEGA data and are presented in Figure 20. Spectra from ock 3582 are located in the south-central part of the low-albedo streak. The derived mineralogy from the streak of 35% pyroxene, 25% feldspar, and 20% high-silica phase matches well with the Group 3 composition from Rogers and Christensen (2007); pyroxene is over estimated by 5% by comparison, but feldspar and high-silica phase concentrations match the corresponding defined values. Although the 5% olivine concentration returned by deconvolution is relatively high when compared to other dark streaks analyzed in this study and is consistent with Group 3 being the olivine-rich spectral class, this amount is below the nominal ~10% detection limit of TES and so must be interpreted with caution.

Spectra from the central peak and dark splotch of the crater, both originating from ock 4085, were unmixed separately. Deconvolution results from the crater interior show significant deviation from that of the streak material and are displayed in Figure 20. For the central peak, the most notable difference is the increase in olivine (20%) to concentrations well above the detection limit, coupled with a dramatic decrease in feldspar (10%) to concentrations near the detection limit. The concentrations of pyroxene and high-silica phase remain the same as the streak. Elevated olivine concentration with

closer proximity to the crater interior is thus observed in both the OMEGA near-IR and TES thermal IR data. Unmixed TES spectra from the dark splotch exhibit the same general trends as the peak, but to a lesser magnitude. For instance, pyroxene and high-silica phase concentrations of the splotch do not differ from the streak by more than 5%, and the remarkable depletion of feldspar observed in the central peak results is also seen in the splotch (15% at this location). These results also exhibit an increase in olivine abundance to concentrations near the TES detection limit of 10%.

Aeolis west. The areas of interest in the Aeolis region are located at the dichotomy boundary and have the same morphological expression. Both consist of low-albedo material at the base of a ~2-km-high cliff. The material is not continuous along the entire cliff but rather exists as individual ~100-km-long segments. Two of these segments will be discussed here as “Aeolis west” and “Aeolis east”. The low-albedo deposits are expressed as both a uniform dark “blanket” of material in some areas and as discrete dune forms in others, which can be observed in the CTX mosaic in Figure 21. Apart from a dark band present along the uppermost section of the cliff face, no layering in the wall is discernable.

The parameter maps and averaged OMEGA spectrum from Aeolis west are shown in Figure 22. Data was taken from OMEGA image ORB0329_2. Band 1 signatures show good spatial correlation with the low-albedo deposits and generally exhibit 1- μm band centers at higher wavelengths overall. The majority of the signatures have 1- μm band centers positioned in the 1.05 to 1.15 μm region. Lower-wavelength band centers are present south of the dark deposits near the edge of the cliff, represented

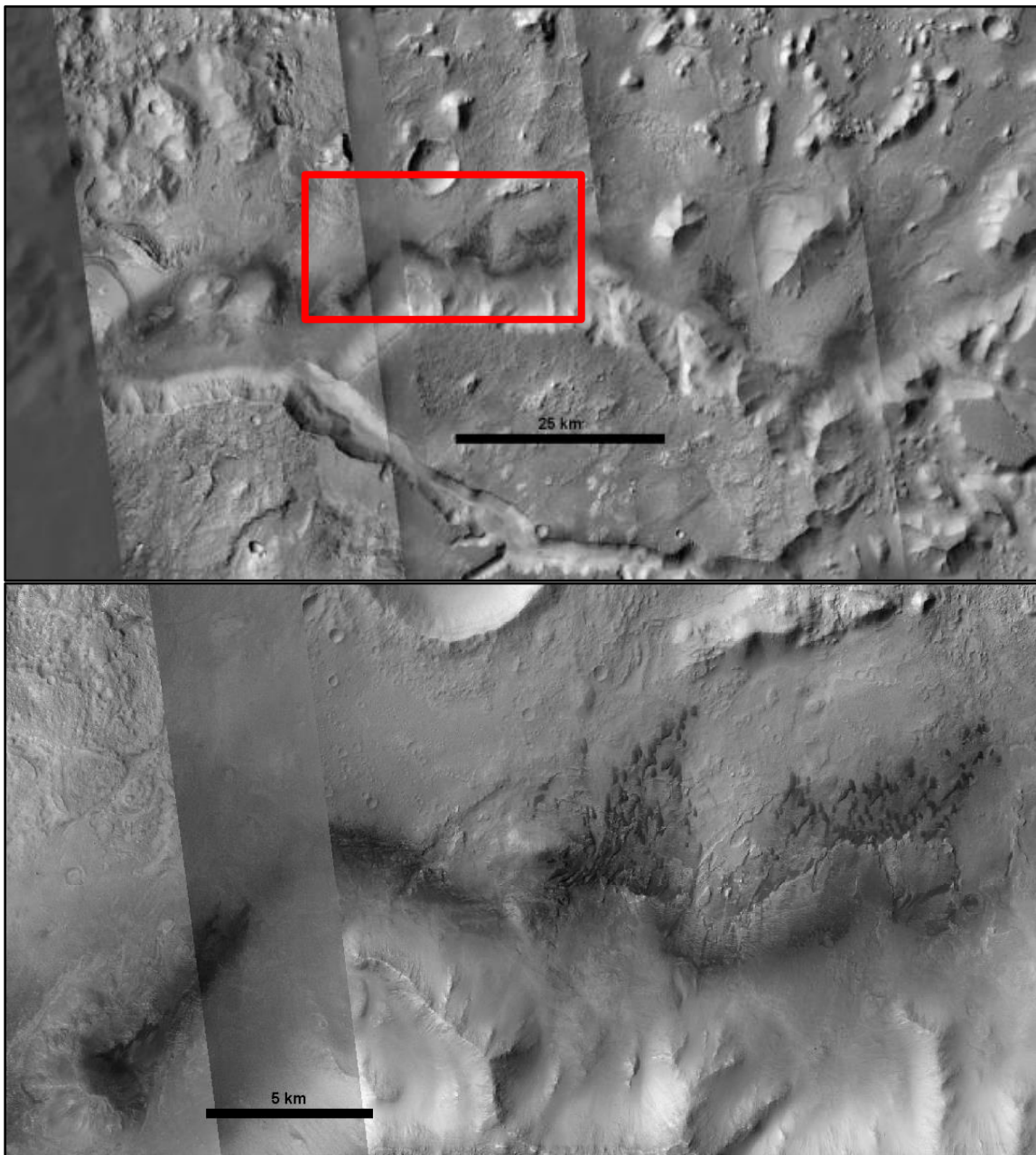
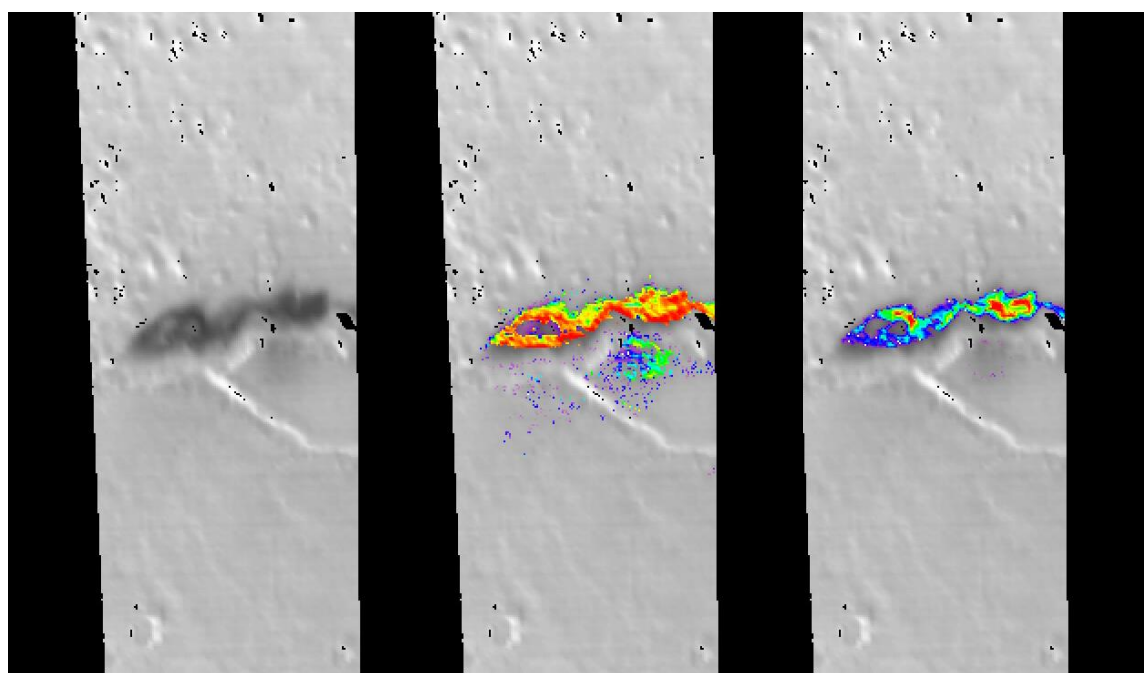




Figure 21. (top) CTX mosaic of the Aeolis west area of interest. Red box denotes the location of 20b. (bottom) Low-albedo deposits located at the base of a 2-km high cliff. The deposits at the eastern part of the image display discrete dune forms, while similar morphology is not seen in the western end.



Albedo

Band 1 center

OLINDEX2

0.90  1.10 0.01  0.05

Aeolis west spectrum

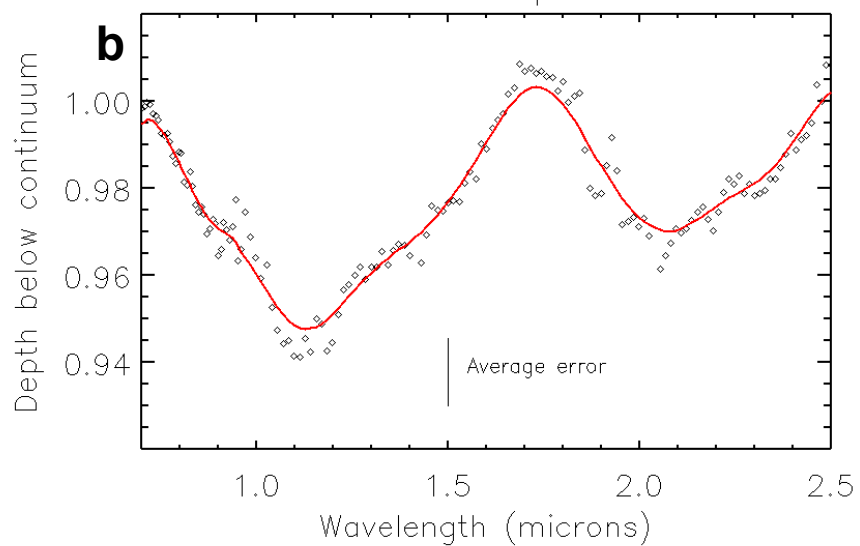


Figure 22. (a) OMEGA parameter maps for the 1- μ m band center position and olivine. (b) Averaged OMEGA spectrum for the central low-albedo streak of Aeolis west.

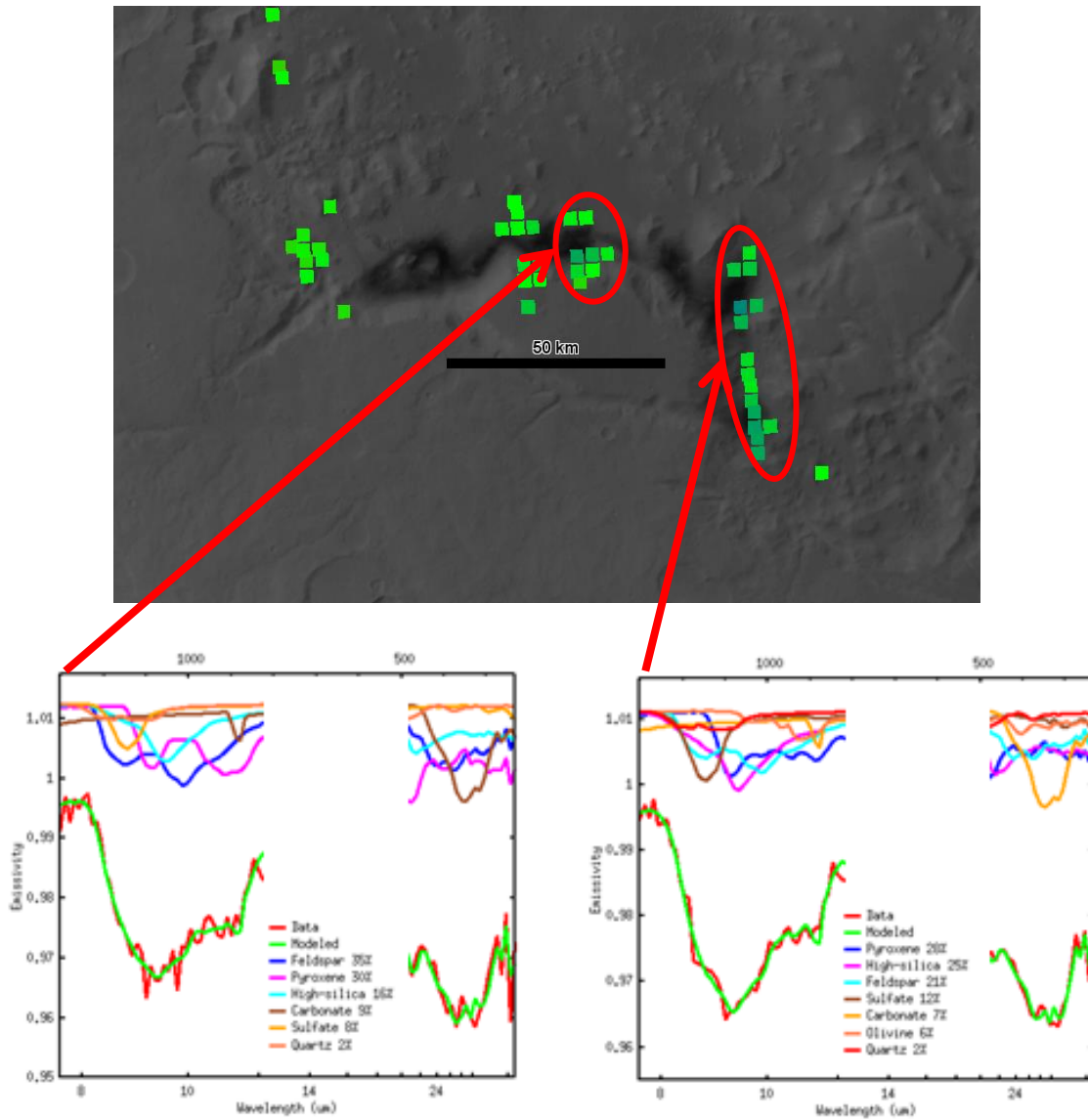


Figure 23. TES deconvolution results for Aeolis west. The left plot is approximately spatially coincident with the area analyzed in Fig. 20 while the right plot corresponds to an area beyond the eastern edge of OMEGA product ORB0329_2, at the base of the now east-facing cliff. Red ellipses denote the spectra that were averaged to produce each plot. Background image is a MOC mosaic.

by blue to green pixels in the band 1 center map in Figure 22; however, the spectra of these pixels have substantial noise that prevented any meaningful analysis and are interpreted to represent bad (*i.e.*, dusty) data. The rest of the index parameters returned a particularly notable result: both HCP and LCP signatures were not detected at any significant amount. OLINDEX2, the only parameter to show exhibit signatures in Aeolis west, is detected throughout the low-albedo deposits at parameter values that exceed 5% in some areas. The primary feature in the averaged OMEGA spectrum is a broad 1- μm absorption band centered at 1.1 μm with shoulders at 0.9 μm and 1.4 μm . The 2- μm band is centered at 2.05 μm and has a large shoulder at 2.4 μm . The reflectance maximum between the two bands is positioned at 1.75 μm .

The TES deconvolutions for Aeolis west are shown in Figure 23. ock 6224 corresponds to the central part of the low-albedo deposits, while ock 3759 corresponds to the eastern deposits at the base of the 2-km high cliff, which faces eastward. The central deposits exhibit a modal mineralogy of 35% feldspar, 30% pyroxene, and 15% high-silica phase. Olivine was not modeled above zero percent. The eastern deposits yield a notably different modal mineralogy of 30% pyroxene, 25% high-silica phase, and 20% feldspar, with olivine modeled at the approximate detection limit of TES.

Aeolis east. The Aeolis east region is located 600 km east-southeast of Aeolis west. It shares much of the same characteristics, in particular consisting of low-albedo deposits located at the base of a 2-km-high cliff. Knobel and Robert Sharp Craters, located 100 km to the south, also exhibit low-albedo surfaces; however, these surfaces are continuous with the dark terrain that characterizes much of the southern highlands of

Mars. Although these craters therefore do not fall under this study's definition of a "window" since they are not absolutely located *within* a dust-covered region, OMEGA data from their deposits are presented here due to their close proximity and comparatively darker surfaces to the nominal Aeolis east area of interest.

The most notable difference from Aeolis west is the apparent lack of dunes within the dark deposits. Ripple morphology is present in some locations at small scales, but these appear to be primarily erosional features that are etched into the bedrock rather than piles of mobile sand. Figure 24c shows such an example where ripples have been eroded into the bedrock in the center of the image. The low albedo material in the image is a smooth mantling unit that appears to drape over the lighter-toned surfaces and cover the topography, including the ripples. Some of this dark material appears to emanate from topographic features such as impact craters and small hills (Figure 24b), indicating transport from north to south.

OMEGA spectra of the Aeolis east region are shown in Figure 25 (ORB0469_3). Multiple low-albedo areas are discernable in the OMEGA visible image: the area of interest identified by the DCI in the north, some darker and more extensive material 100 km to the south in Robert Sharp Crater, and additional dark deposits along floor of the southern wall of nearby Knobel Crater. The latter two areas were not considered as candidate areas of interest for this study due to their proximity and continuity with the extensive low-albedo feature of Hesperia. However, their inclusion in the OMEGA image investigated here means that it is possible to analyze their compositions nonetheless and compare them with that of the targeted area of interest. The band 1 center parameter

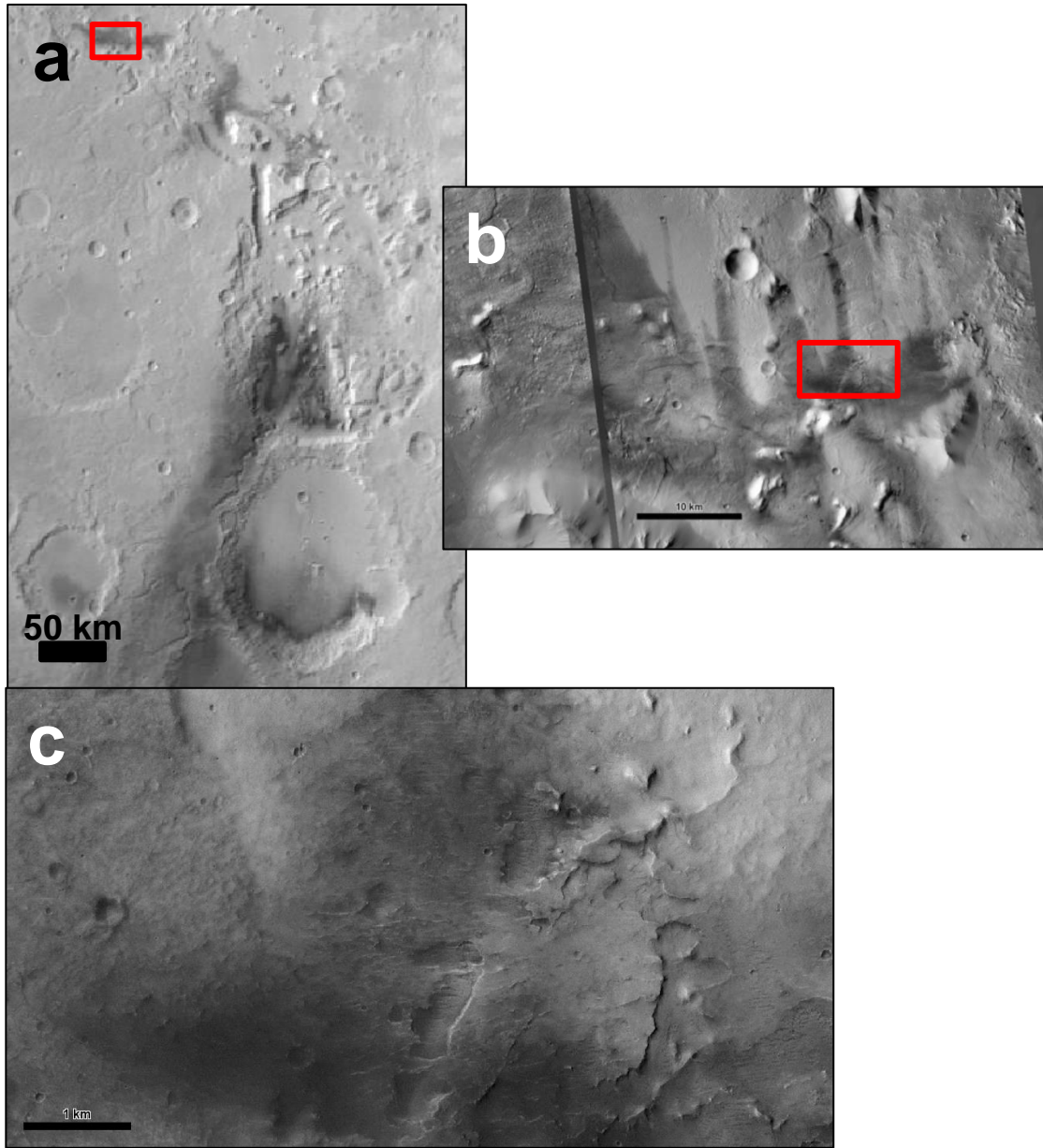


Figure 24. (a) MARCI mosaic of the Aeolis east region. The low-albedo deposits at the northern part of the image make up the nominal area of interest. The darker surfaces in the central to southern part of the image are continuous with the low-albedo southern highlands. The red box denotes the location of the CTX image in 24b. (b) CTX mosaic showing the low-albedo surfaces of Aeolis east in greater detail. The red box denotes the location of the CTX image in 24c. (c) CTX mosaic showing erosional ripple morphology within Aeolis east. The ripples appear to be etched into the lighter-toned surface, which is blanketed by the smooth dark material.

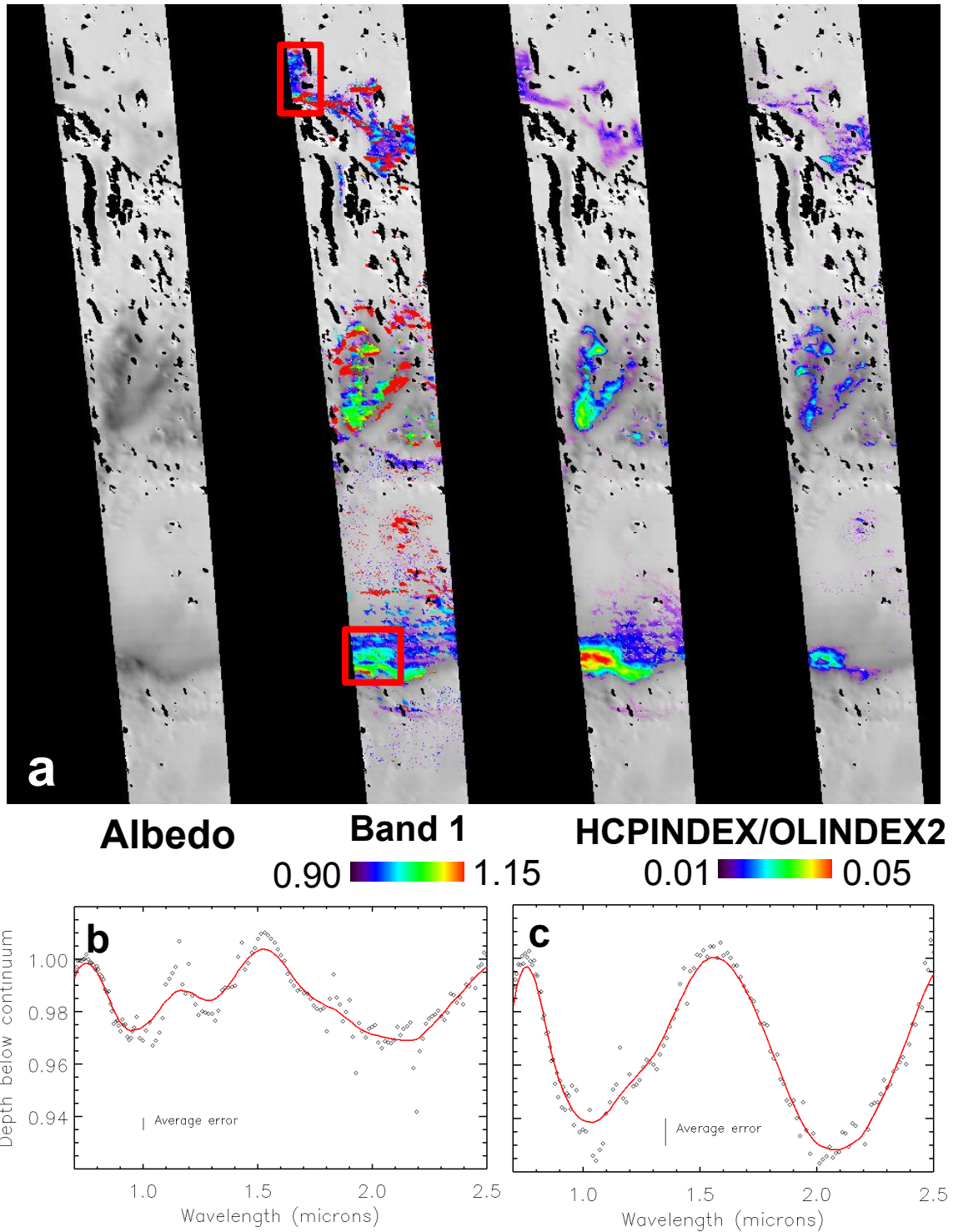


Figure 25. (a) OMEGA parameter maps for the 1- μ m band center position, HCP, and olivine in Aeolis east. Red boxes in the band 1 center map denote the spectra averaged to produce the plots below. (b) Averaged OMEGA spectra from the upper red box in 25a. (c) Averaged OMEGA spectra from the lower red box in 25a.

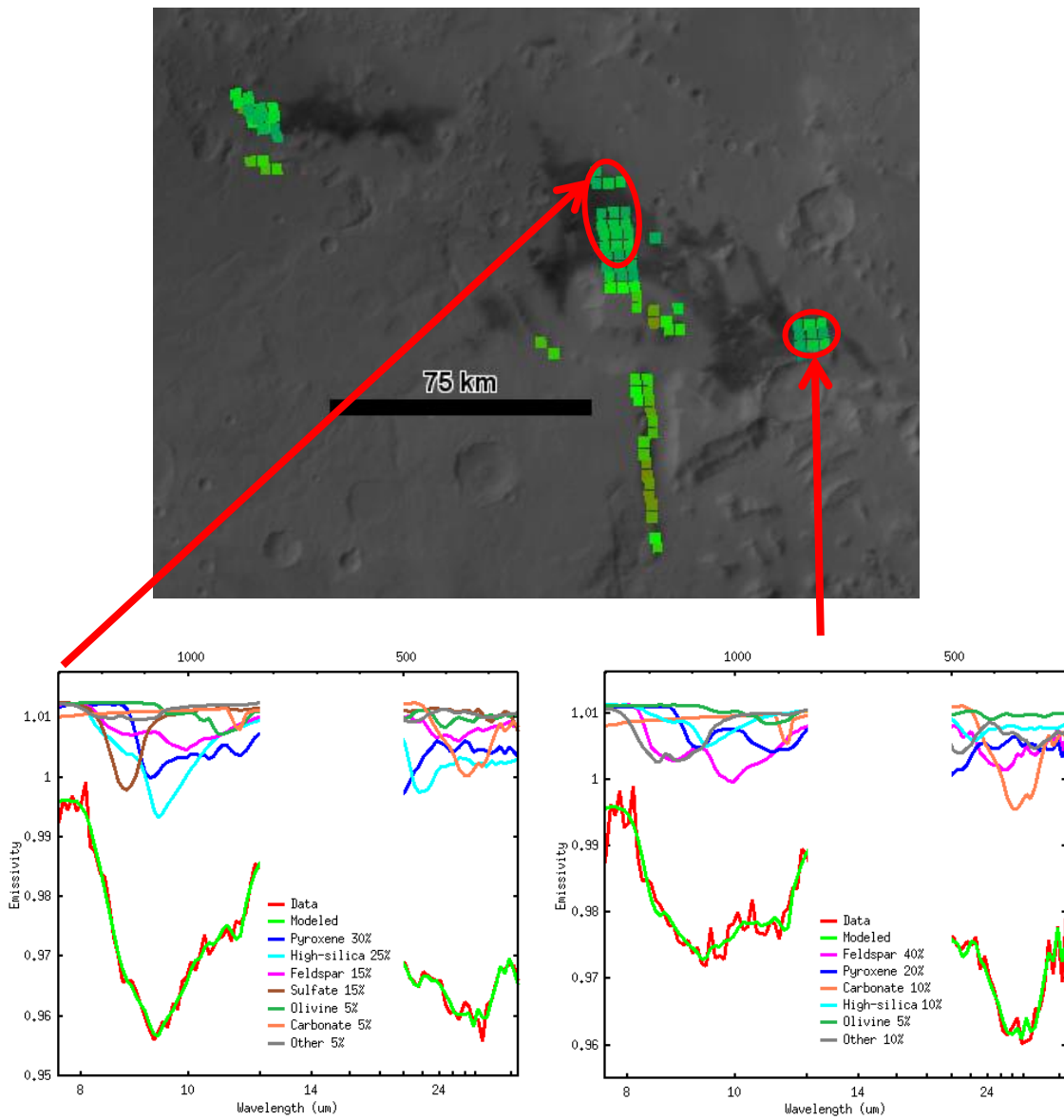


Figure 26. TES deconvolution results for Aeolis east. Red ellipses denote the spectra that were averaged and unmixed to produce each plot. Background image is a MOC mosaic.

reveals a relatively large diversity in band center positions in the area of interest and middle dark area, but more uniformity within the southernmost deposits. HCPINDEX signatures are remarkable in that index values are highest towards the southern part of the image and lowest in the north. These values are also significantly higher overall compared to other areas of interest; the dark deposits within Knobel Crater in particular exhibit index values greater than 15%. Parameter values in the nominal area of interest do not exceed a few percent. A similar but less pronounced trend is observable in the OLINDEX2 parameter maps. Index values are greater towards the southern deposits but are far less varied throughout the entire image.

The spectrum from the nominal area of interest most notably exhibits a narrow and deep absorption band at 1.3 μm , which is not associated with any of the mafic minerals considered in this study and is interpreted as an anomaly of the dataset. The presence of the enigmatic 1.3 μm absorption in this dataset makes characterization of the 1- μm difficult, but commonalities with the averaged spectrum from nearby Knobel Crater suggest that these two areas are spectrally similar. In particular, the band widths and position of the reflectance maximum are nearly identical to those of the nominal area of interest. Given these similarities, it would not be unreasonable to infer the mineralogy of Aeolis east using data from Knobel Crater, where the spectral features are stronger and less noisy. The 1- μm band is centered at 1.05 μm and has a shoulder at 1.3 μm , while the wide 2- μm band is centered at 2.1 μm .

TES spectra from two orbits were deconvolved and are shown in Figure 26. The first, ock 3809, covers the western end of the low-albedo area while ock 3897 covers the

eastern end. Deconvolution both sets of spectra reveals that there are two different compositions in Aeolis east. The modal mineralogy of the western area is 30% pyroxene, 25% high-silica phase, and 15% feldspar. The eastern end of the area appears to be comparatively feldspar-rich, consisting of 40% feldspar, 20% pyroxene, and 10% high-silica phase.

Cerberus. Two “windows” analyzed are located in the Cerberus region, which is located to the immediate east of Elysium Planitia. Both are part of the large albedo feature north of the Cerberus Fossae. Figure 27a and b are MARCI images taken 240° L_S apart during Mars Year 29, once during the dust clearing event observed to occur during spring in the northern hemisphere and once during the dusty season. Although the overall albedo had diminished between the two frames, the albedo feature is still clearly distinguishable from the surrounding bright plains.

Cerberus west. The Cerberus west region covers most of the western half of the Cerberus albedo feature. The surface consists of smooth plains deposits that originate from Elysium Mons (Skinner, 2006). The OMEGA albedo image used in this analysis reveals a sharp boundary between the bright plains and dark deposits. Impact craters with diameters of only a few kilometers are visible within the dark deposits and are easily discernable by bright streaks that emanate from many of the craters toward the southwest. These streaks are caused by the crater rims acting as topographic obstacles to the southwestward winds, creating a “dead zone” downwind of the crater where wind velocity is substantially decreased. These zones will receive greater amounts of settling

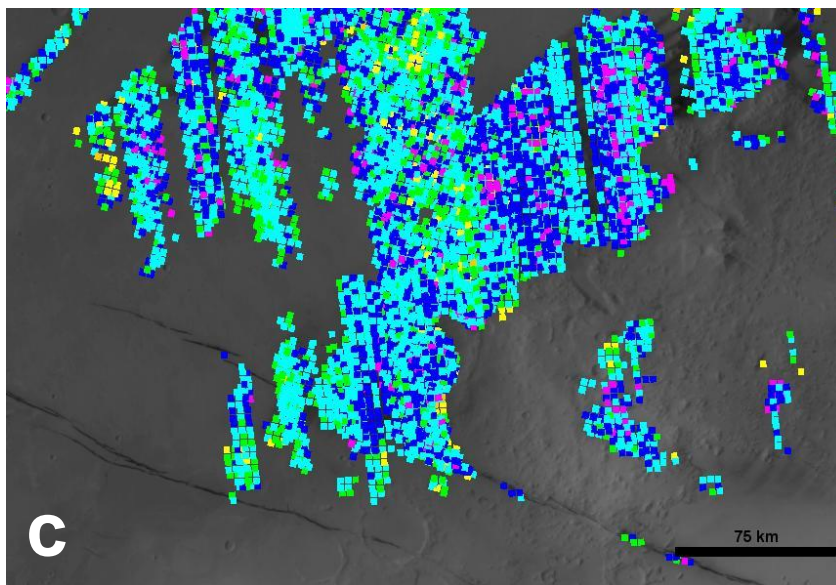
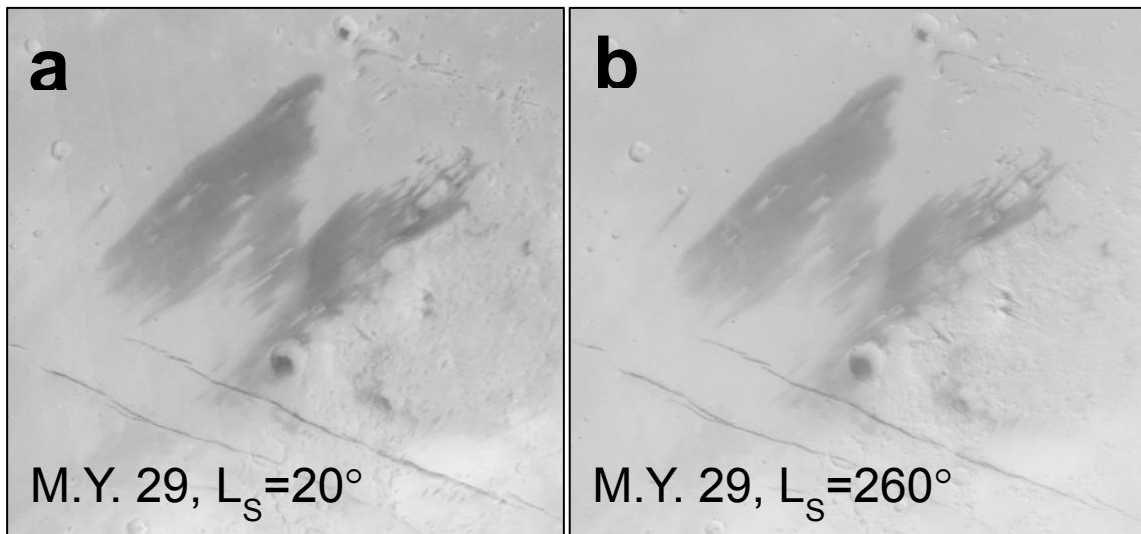


Figure 27. MARCI mosaics showing the Cerberus albedo features during (a) spring and (b) late summer in the northern hemisphere. (c) MOC mosaic with colored boxes representing TES spectra that are classified as having low surface dust cover by the DCI.

dust, as wind speeds are not capable of mobilizing dust particles (Thomas *et al.*, 1981; Peterfreund, 1981).

OMEGA results for the Cerberus west region are shown in Figure 28 and are derived from image ORB3643_3. Band 1 parameter signatures exhibit very good spatial correlation with the low-albedo surfaces seen in the OMEGA visible image. 1- μm band center positions are typically 1.10 to 1.12 μm throughout the part of the albedo feature that appears in the scene. Bright wind streaks are discernable as “holes” within the band 1 signatures in the map; spectra from the margins of these streaks tend to have 1- μm band centers at longer wavelengths. HCPINDEX and OLINDEX2 signatures are limited throughout the region. The highest parameter values are located at the northernmost part of the low-albedo deposits visible in this OMEGA image. The averaged spectrum for Cerberus west has a broad 1- μm absorption centered between 1.05 and 1.10 μm and a shoulder on its longer-wavelength edge at 1.35 μm . Another potential shoulder is present at 0.9 μm . A second broad absorption band is centered at 2.15 μm , and the reflectance maximum between the bands is located at 1.7 μm .

An additional OMEGA observation (ORB1445_2) covers the northern part of Cerberus west, which exhibited the highest parameter values of HCP and olivine in image ORB3643_3 as detected by the index parameters. Parameter maps for this area are shown in Figure 29. Band 1 center parameter values above 2% show remarkable spatial coincidence with low-albedo surfaces; the sharp contrast between the bright and dark region located at the center of the visible image is also the boundary between sub- and greater than 2% absorption bands. Furthermore, the bright wind streaks located within the

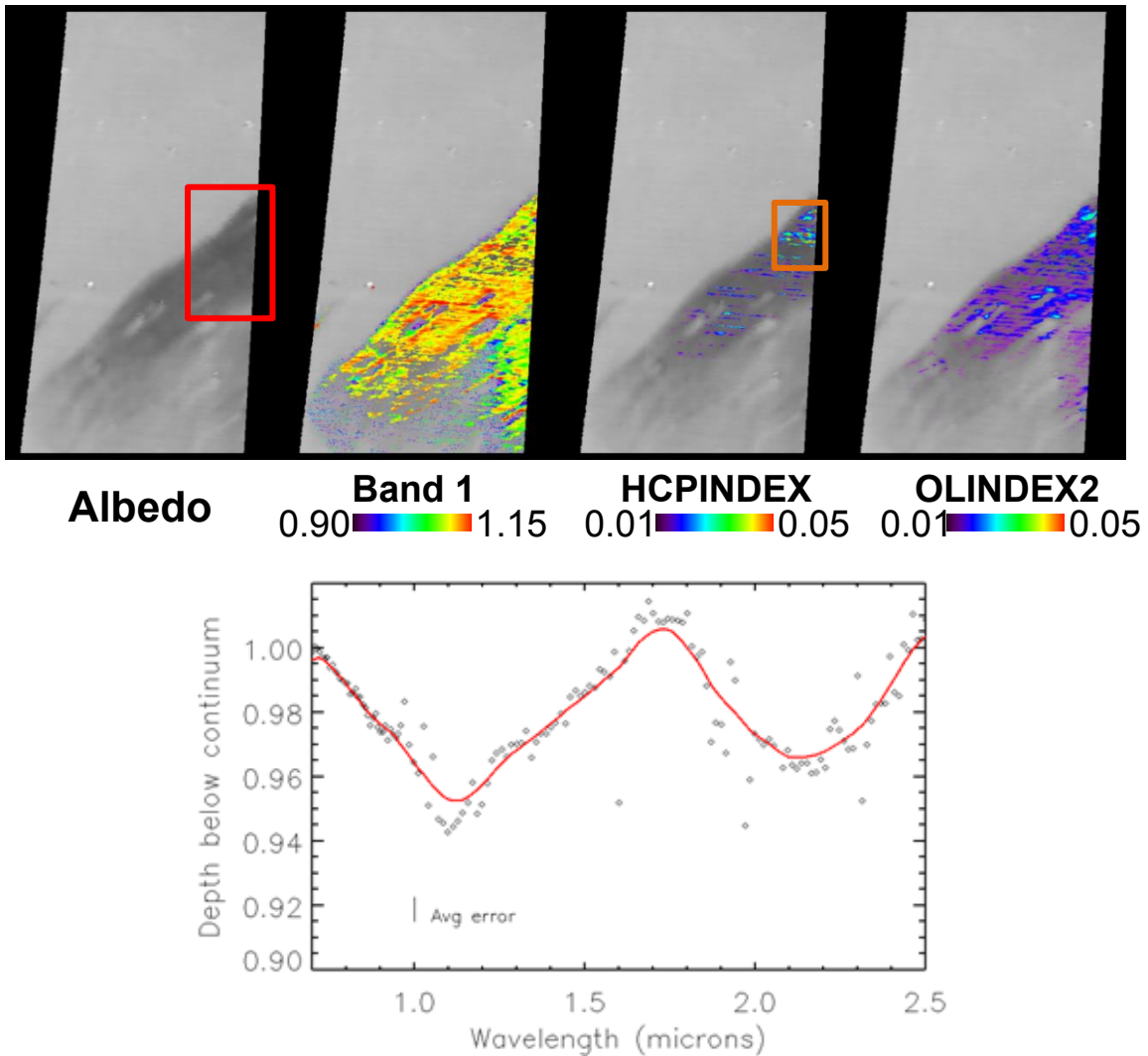


Figure 28. (top) OMEGA parameter maps for the 1- μm band center position, HCP, and olivine in broad Cerberus west area of interest. The red box denotes the approximate location from which data in Fig. 29 are analyzed. The orange box in the HCPINDEX map shows the area from which data were averaged to produce the spectrum below. (bottom) Averaged OMEGA spectrum for the Cerberus west area.

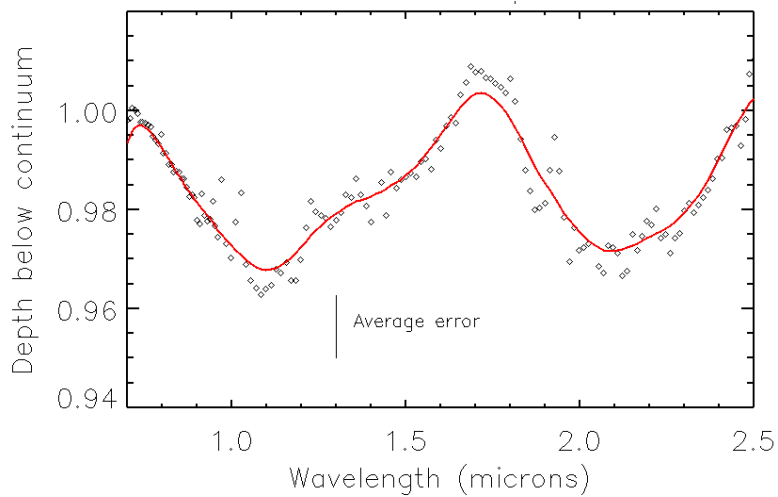
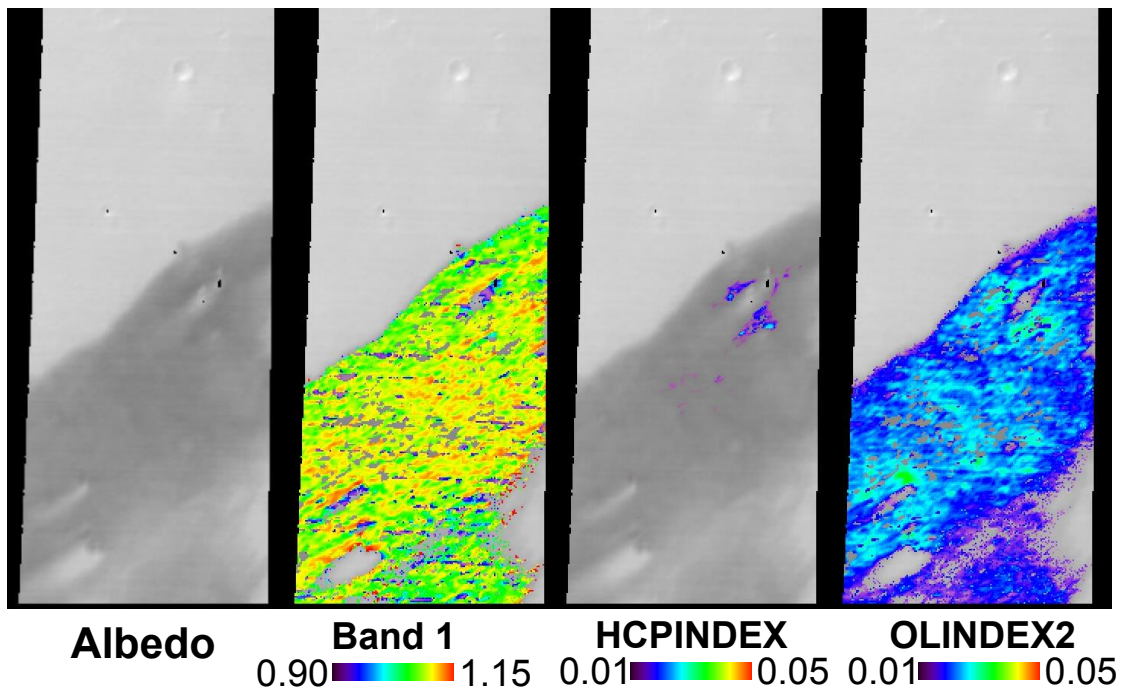


Figure 29. (top) OMEGA parameter maps for the 1- μ m band center position, HCP, and olivine in the part of Cerberus west located within the red box in Fig. 28. (bottom) Averaged OMEGA spectrum for the dark surfaces in the above image.

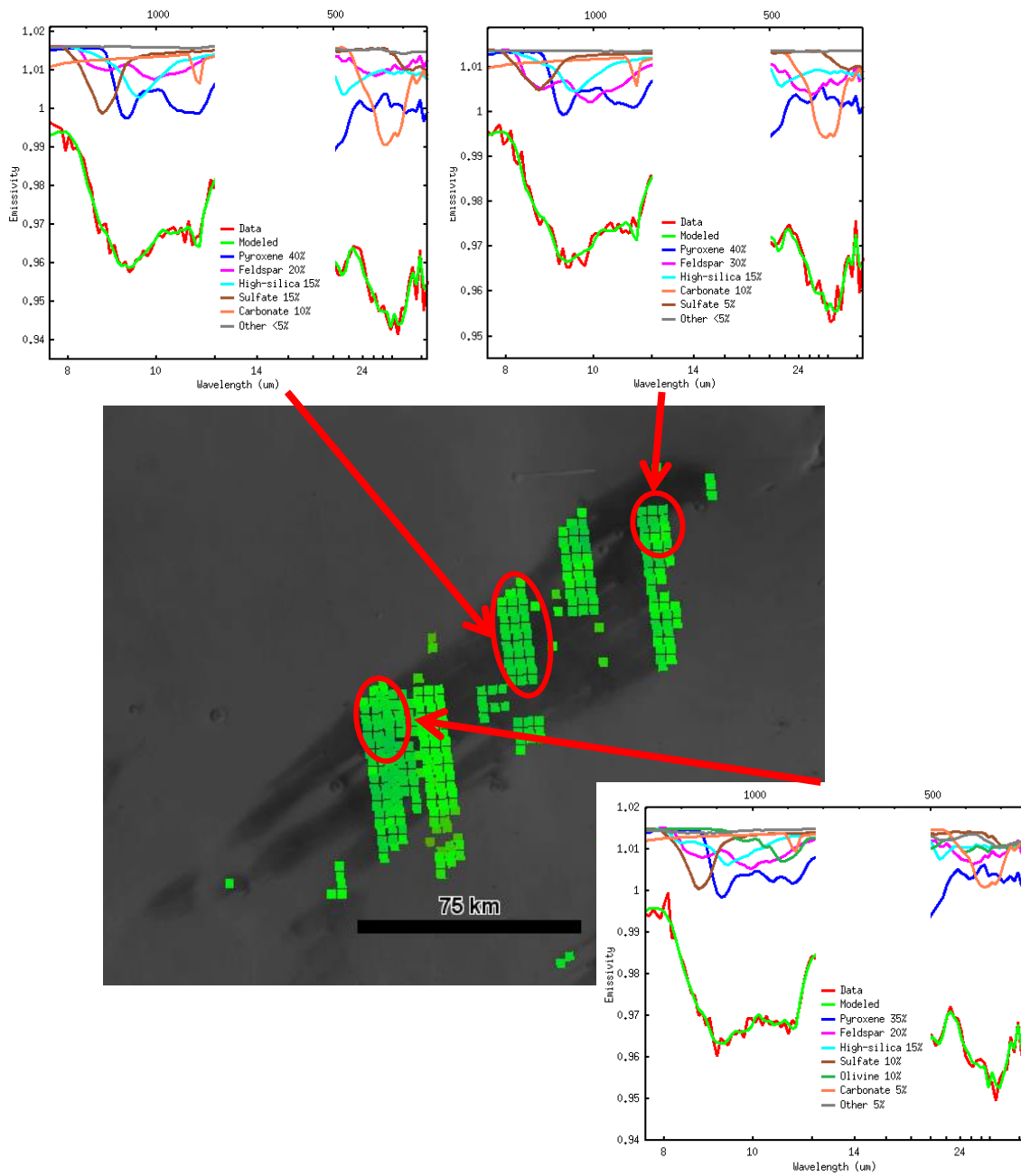


Figure 30. TES deconvolution results for the Cerberus west region. Context image is a MOC global mosaic.

albedo feature do not have spectra with reliable 1- μm absorption bands, resulting in their appearance as “holes” in the band 1 parameter map. Band center positions are fairly uniform throughout the dark deposits, the typical position being $\sim 1.10 \mu\text{m}$. Notable deviations from this value include the margins of bright wind streaks, which exhibit band centers at shorter wavelengths; however, these spectra correspond to the noisiest data and shallowest 1- μm band centers among the band 1 center signatures in the low-albedo region. Other mineral parameters are weak. HCP signatures are limited to the margins of a bright wind streak at the northern part of the albedo feature, but the data are comparatively noisy and the associated HCPINDEX parameter values are less than 3%. OLINDEX2 signatures are also weak (3% maximum) but are considerably more extensive than HCPINDEX, distributed over the entirety of the albedo feature. The LCPINDEX parameter did not return any signatures. The averaged spectrum for this focused area is largely similar to the broader Cerberus region presented in Figure 25, with what appears to be a composite 1- μm absorption band centered near $1.09 \mu\text{m}$, a 2- μm band centered in the 2.10 to 2.15 range, and a reflectance maximum between the two bands at $1.7 \mu\text{m}$.

TES deconvolution results for the Cerberus western albedo feature are shown in Figure 30, where spectra from the western, central, and eastern parts of the feature are shown. Pyroxene concentration varies from 30 to 40% throughout the feature. Feldspar is present from 20 to 30% concentrations while high-silica phase concentrations are consistently at 15%. At its highest, olivine is detected at detection-limit-concentrations (10%) in the western part of the area.

Cerberus crater. The Cerberus crater region consists of three different morphological features within the same scene, all of which appear in OMEGA data product ORB1445_2: an unnamed 30-km-diameter crater and its low-albedo splotch and streak, the nearby Cerberus Fossae to the south, and the eastern part of the Cerberus albedo feature to the north. Parameter maps and spectra for this area are shown in Figure 31. Band 1 parameter signatures correlate well with low-albedo surfaces throughout the image. Band centers are predominantly $\sim 1.12 \mu\text{m}$, while some areas such as the north to eastern rim of the unnamed crater, the margins of bright streaks emanating from smaller impact craters, and the Cerberus Fossae exhibit band centers greater than $1.15 \mu\text{m}$.

HCPINDEX signatures are localized to the low-albedo splotch within the unnamed crater only; however, the parameter values are higher ($>6-7\%$) than typical values from other areas of interest in this study. The OLINDEX2 parameter is fairly extensive, covering the unnamed crater, the Cerberus Fossae, and northern parts of the albedo feature, but the only area with index values above 3% are the northern rim of the unnamed crater and some sections of the northern fossa.

The averaged spectrum for the northern rim of the unnamed crater has a broad, asymmetric 1- μm band centered at $\sim 1.1 \mu\text{m}$ with shoulders at $0.9 \mu\text{m}$ and $1.5 \mu\text{m}$. The 2- μm band is centered at $2.05 \mu\text{m}$. The spectrum from the northern fossa is very similar in shape, with the exception of a lesser slope between 0.7 and $1.0 \mu\text{m}$. The band center positions, shoulders of the 1- μm band, and reflectance maximum are the same for both areas. The spectrum from the low-albedo splotch within the unnamed crater exhibits differences from the two aforementioned areas. Most notable is the 1- μm band center

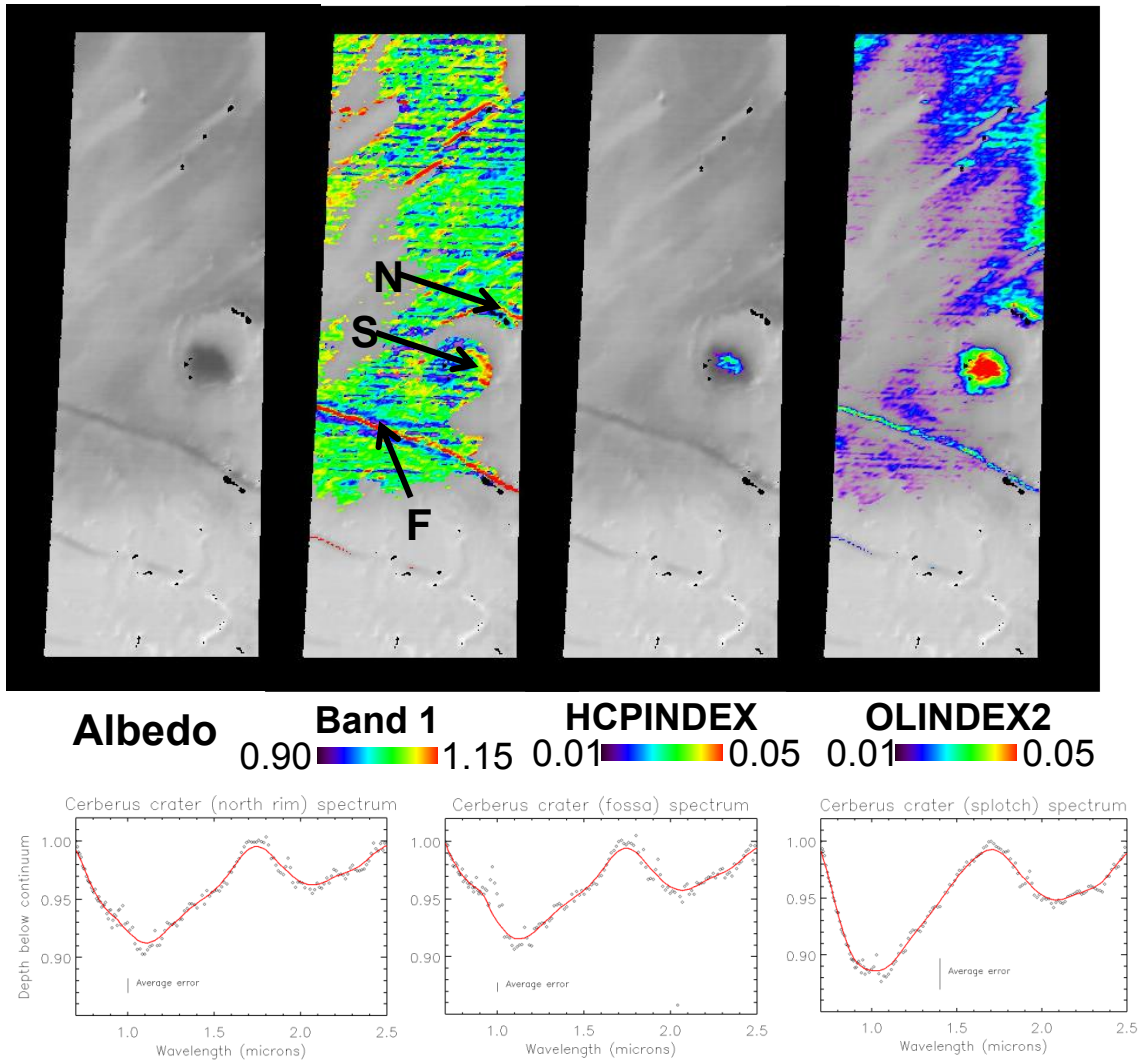


Figure 31. (top) OMEGA parameter maps for the 1- μm band center position, HCP, and olivine in the Cerberus crater area of interest. The arrow labeled “N” points to the location where the “north rim” spectrum was averaged from. “S” corresponds to the splotch and “F” corresponds to the fossa. (bottom) Averaged spectra from the (left) north rim of the crater, (center) the fossa, and (right) the low-albedo intracrater splotch.

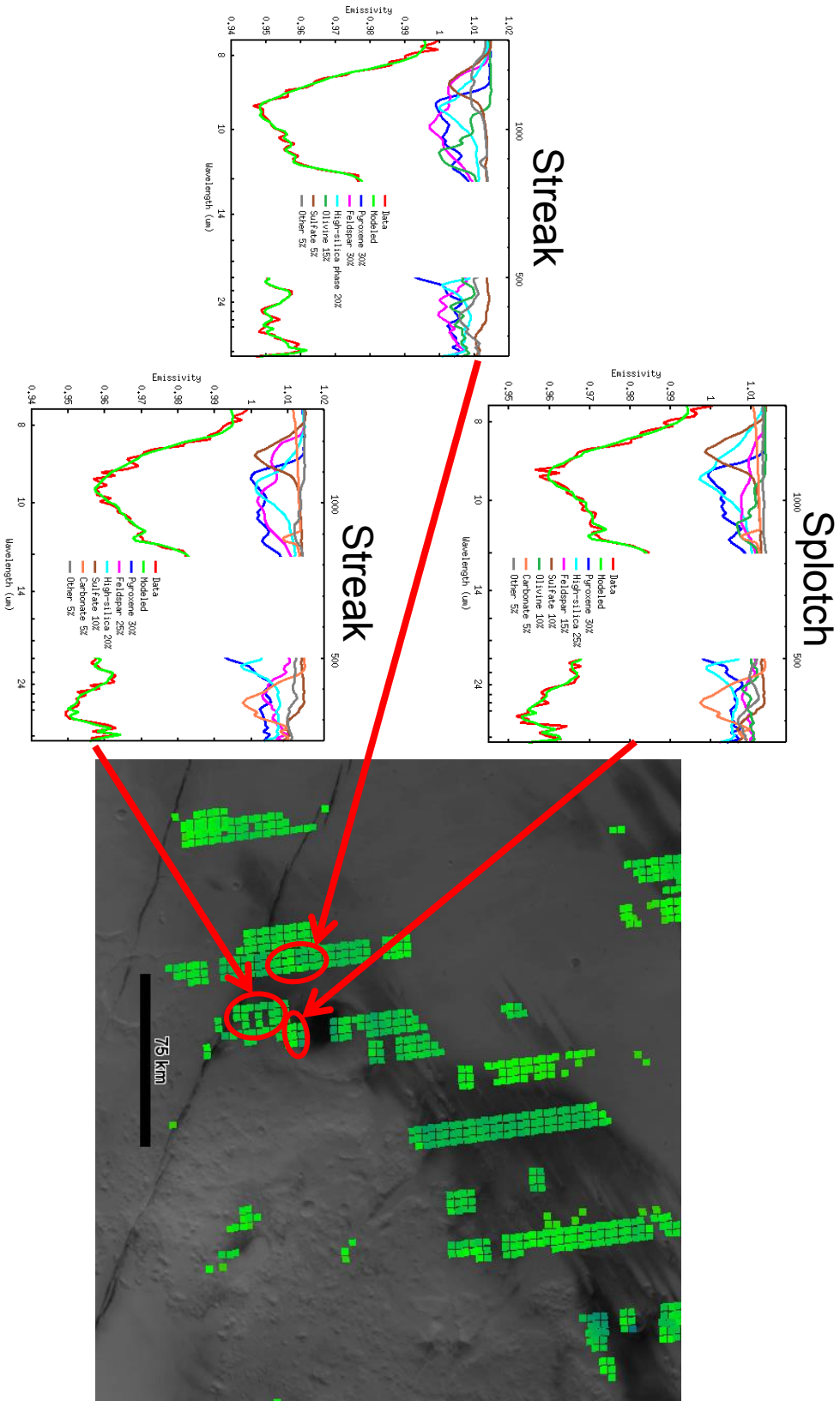


Figure 32. TES deconvolution results for the Cerberus crater area. Red ellipses denote the spectra that were averaged and unmixed to produce each plot. Context image is a MOC global mosaic.

shifting to $\sim 1.05 \mu\text{m}$ and the reflectance maximum between the two absorption band shifting from $1.75 \mu\text{m}$ to $1.65 \mu\text{m}$. The averaged splotch spectrum is also accompanied by higher errors.

TES deconvolutions were performed for both the splotch and streak of the unnamed crater and are shown in Figure 32. Spectra from two different parts of the dark streak were unmixed, and both yielded the same general mineralogy within the confidence limit of TES: 30% pyroxene, 25 to 30% feldspar, and 20% high-silica phases. One of these areas, the part of the streak to the west of the crater, exhibits exceptionally high detections of olivine at 15%. The spectra from the intracrater splotch produce results with comparable pyroxene concentration but elevated high-silica phase and decreased feldspar (32% pyroxene, 25% high-silica phase, 15% feldspar). Olivine is modeled at 10% concentration within the splotch.

Gusev Crater. Gusev Crater was the landing site of the Spirit rover, which carried the Mini-TES thermal emission spectrometer onboard. Results from Mini-TES indicated that the rocks in Gusev Crater are of uniform composition and dominated by olivine-rich basalt, which has been corroborated by other instruments onboard Spirit (Christensen *et al.*, 2004; McSween *et al.*, 2006). OMEGA data product ORB3328_4 was used to analyze the east-central floor of Gusev Crater. The image footprint covers the eastern half of the crater, which includes a NW-SE-oriented low-albedo splotch $\sim 50 \text{ km}$ in length where the Spirit landing site is located. The averaged spectrum and parameter maps derived from this dataset are shown in Figure 33.

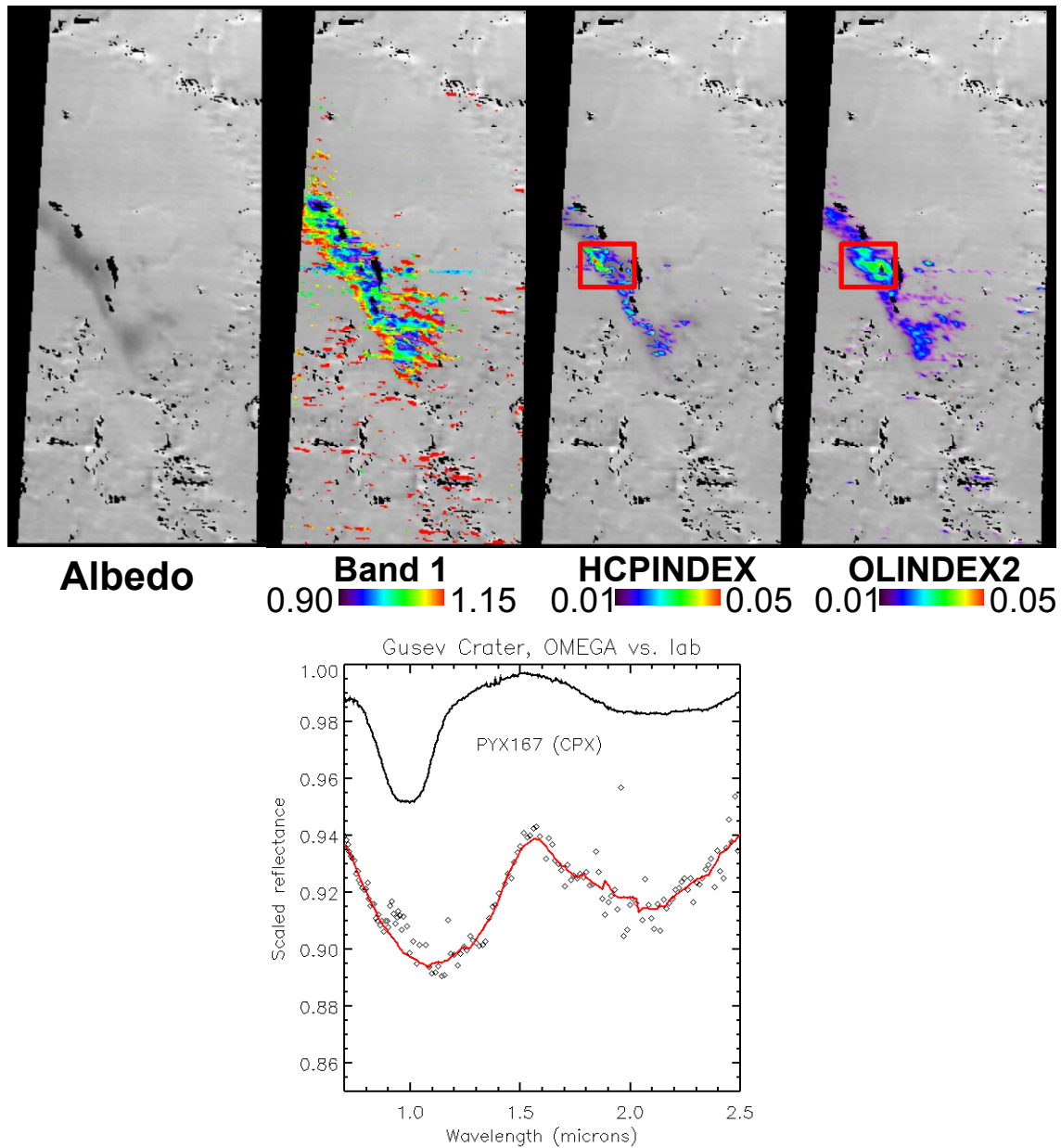


Figure 33. (top) OMEGA parameter maps for the 1- μ m band center position, HCP, and olivine in Gusev Crater. Red boxes denote the location from which the spectrum below was averaged. (bottom) Averaged spectra from the part of the splotch with highest HCP and olivine detections is plotted in red, while a laboratory spectrum of a clinopyroxene is plotted in black.

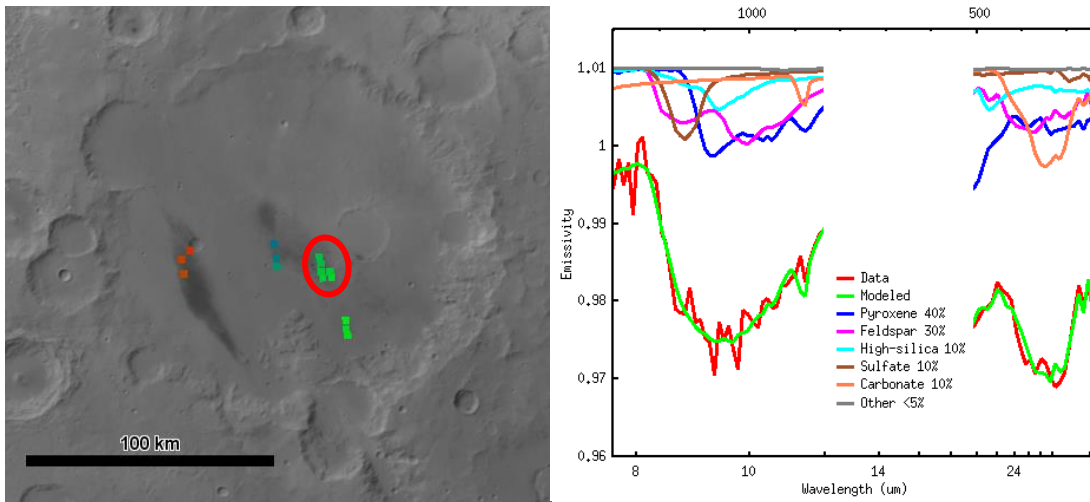


Figure 34. TES deconvolution results for a low-albedo splotch within Gusev Crater. The red ellipse denotes the spectra that were averaged and unmixed to produce the plot. Context image is a MOC global mosaic.

The band 1 center parameter map shows that the distribution of spectra with deep 1- μm band centers generally correlate very well with dark surfaces, especially the extensive low-albedo splotch. Band center positions are highly varied throughout the area surrounding splotch, distributed throughout the entire 0.9 to 1.15 μm range. Most of the low-albedo surfaces are associated with the lower-wavelength band centers ($\sim 0.95 \mu\text{m}$) while the margins of the splotch exhibit band centers at higher wavelengths. HCPINDEX signatures are also limited to the low albedo splotch but are predominantly concentrated towards the center of the feature. This area is also where the highest index values are located, as some spectra exhibit $>5\%$ abundances. Detections are relatively sparse to the north of this central area, and to a lesser extent the south as well. The distribution patterns for OLINDEX2 are largely the same as that of HCPINDEX: signatures are more numerous and higher index values are greatest at the center of the splotch and diminish toward the margins. No LCP signatures were detected at any significant amount.

The averaged spectrum shown in Figure 30 corresponds to the central portion of the low albedo splotch within Gusev Crater, where the spectral indices reported the greatest abundance of HCP and olivine signatures. The spectrum has broad 1- and 2- μm absorption bands. The deep 1- μm band is centered near 1.05 μm while the comparatively shallower 2- μm band is centered near 2.05. The reflectance maximum between the two bands, located at $\sim 1.55 \mu\text{m}$, is shifted to slightly shorter wavelengths compared to spectra from other areas of interest.

Only a few TES spectra were deconvolved from ock 3883, which corresponds to the southeastern part of the low-albedo splotch within Gusev Crater. The derived modal

mineralogy from the averaged spectrum is 40% pyroxene, 30% feldspar, and 10% high-silica phase. These data are shown in Figure 34.

Gale Crater. Gale Crater is the landing site of the Mars Science Laboratory (MSL) Curiosity rover (Grotzinger, 2012). Low-albedo material that drapes around the base of Mount Sharp, the central mound that occupies most of the crater floor, was targeted. There is also a dark streak that is continuous with the intracrater material within Gale Crater and extends to the rim of Lasswitz Crater, ~100 km to the south. OMEGA image ORB0436_2 covers roughly the eastern half of Gale Crater and its streak. The Curiosity field site is at the northwestern flank of Mount Sharp and is therefore not included in this image, although the dune field traversed by the rover is continuous with the dark materials observed here.

The averaged spectrum and parameter maps from the Gale Crater dark deposits are shown in Figure 35. The 1- μm band appears to be a composite of at least three different bands. These bands appear to be positioned near 0.92, 1.05, and 1.3 μm . The 2- μm band is centered at 2.10 μm and the reflectance maximum between the two bands at 1.6 μm . The HCPINDEX parameter map shows three discontinuous low-albedo areas with HCP signatures present. From north to south, these are the intracrater deposits in Gale Crater, the dark streak of Gale Crater, and low-albedo materials concentrated along the eastern floor of Lasswitz Crater. HCPINDEX values for both the streak and Lasswitz Crater materials are comparatively weak (~5%). Index values within Gale Crater are the highest encountered in this study. The interior of the low-albedo area directly south of Mount Sharp exhibits HCPINDEX values approaching 30%. HCP detections diminish

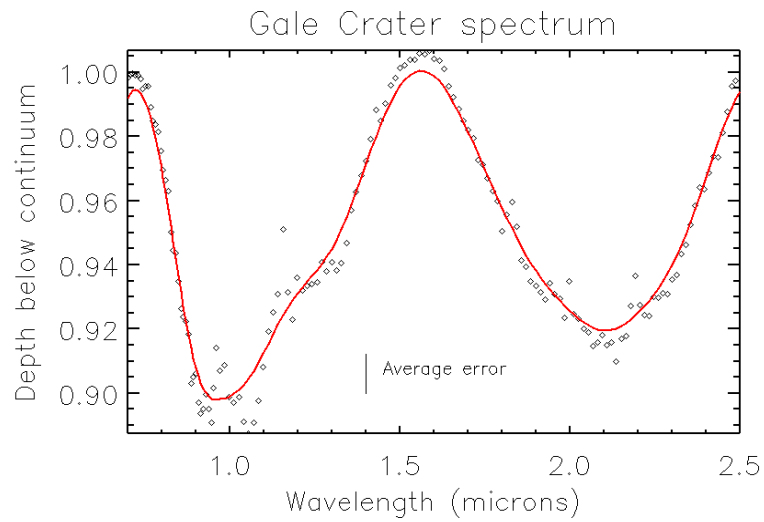
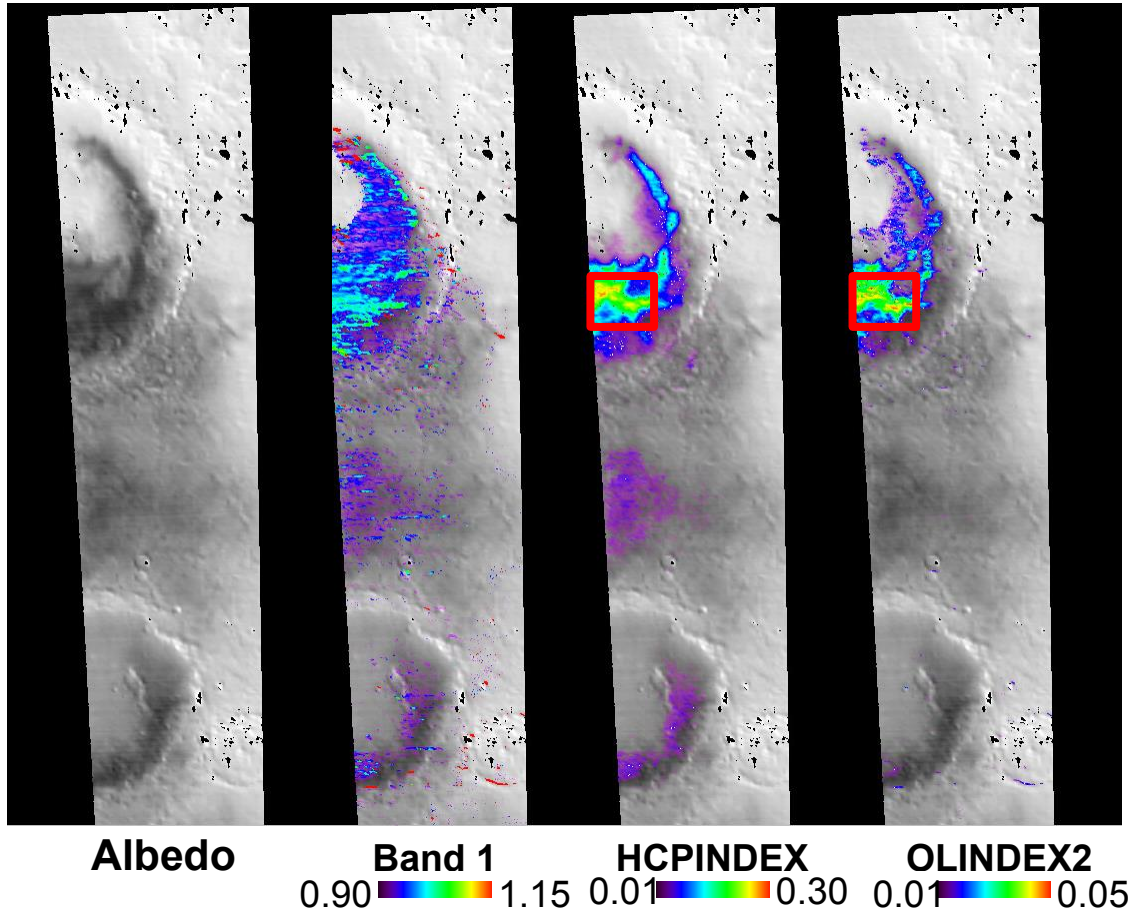


Figure 35. (top) Parameter maps for the 1- μ m band center position, HCP, and olivine in Gale Crater. Red boxes denote the location from which the spectrum below was averaged. (bottom) Averaged spectra from the part of the splotch with highest HCP and olivine detections.

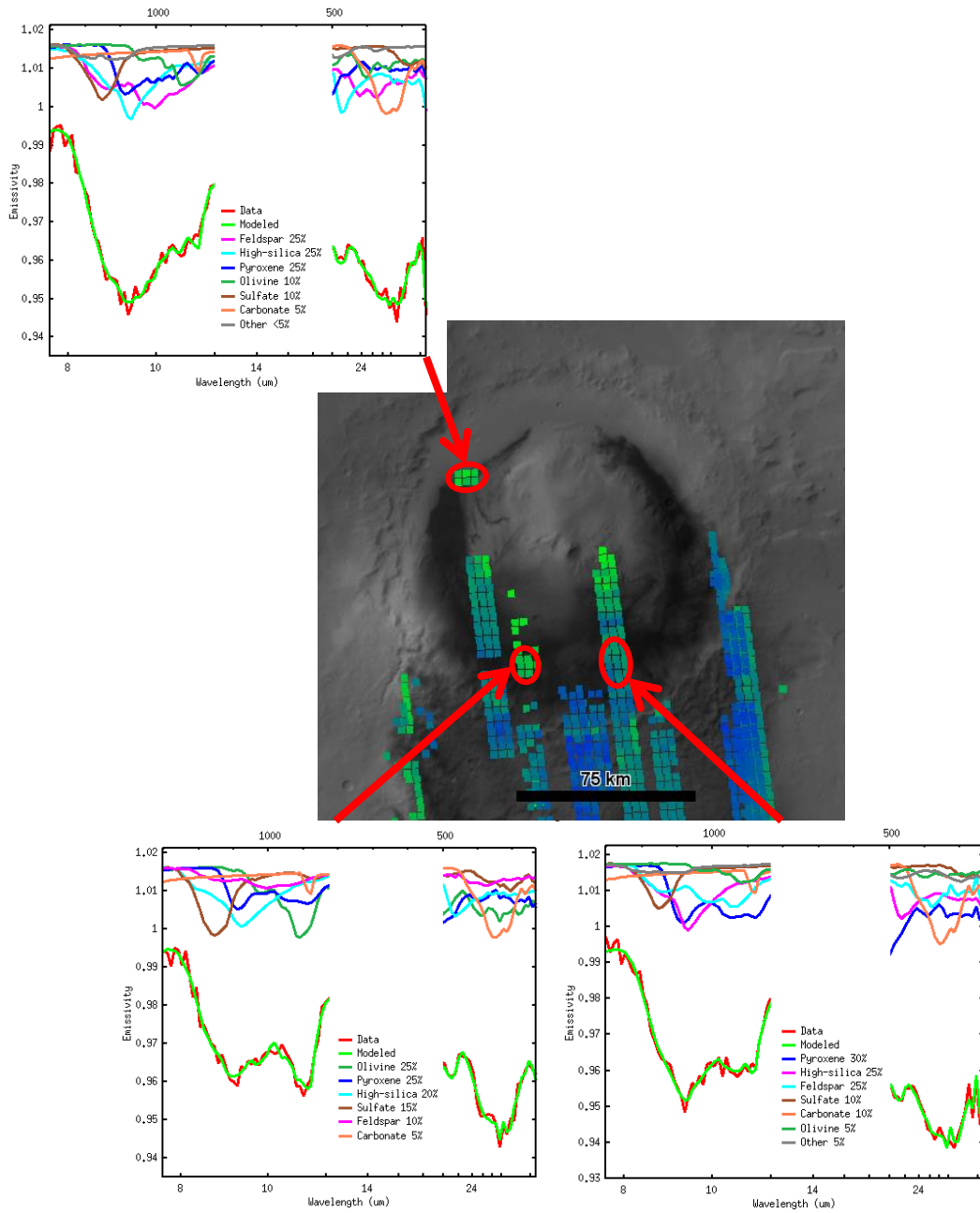


Figure 36. TES deconvolution results for the Gale Crater low-albedo materials. Red ellipses denote the spectra that were averaged and unmixed to produce each plot. Context image is a MOC global mosaic.

with increasing distance from this position, but parameter values of at least 10% are present throughout the entirety of the intracrater dark deposits.

OLINDEX2 signatures within the scene are almost entirely restricted to Gale Crater. The spatial distribution of these signatures is largely similar to that of HCPINDEX. The only notable spatial trend unique to OINDEX2 is the presence of additional signatures on the lower flanks of Mount Sharp, whereas HCP detections were limited to the dark deposits occupying the crater floor. OINDEX2 values are typically <5% and are comparable to those observed at other areas of interest. Peak values of ~4.5% occur in the same locations where the highest HCPINDEX values were recorded: the central dark deposits directly south of Mount Sharp.

TES deconvolution data for Gale Crater are shown in Figure 36. Pyroxene and high-silica phases are consistently at 20 to 30% concentrations throughout the low-albedo deposits. Feldspar is modeled at similar abundances except in the south-southwestern splotch where it drops to near the TES detection limit. This decrease in feldspar is coupled with exceptionally high olivine concentrations at 25%. Olivine is only present in other TES data in Gale Crater near the detection limit. This trend is consistent with the OMEGA data in that the most olivine-rich materials appear to the immediate south of the Mount Sharp summit.

Arabia Terra. Unlike Elysium Planitia and Tharsis, which contain most of the largest volcanic constructs on Mars, there are no obvious prominent geologic features within the comparatively heavily-cratered Arabia Terra. All dust-free locations as classified by the DCI are associated with low-albedo intracrater deposits. Many of these

deposits have a dark streak that extends onto the surface in a general south to southwestward direction, features that are also very common in nearby Oxia Palus to the west. Deposits and streaks in Arabia Terra appear to be randomly distributed as they are spread over thousands of kilometers in both the north-south and east-west directions. MARCI observations do not yield any additional areas of interest. The aforementioned low-albedo deposits and their associated streaks are the only dark features that are present throughout the sequence of MARCI images; no dust-clearing or darkening event were otherwise observed. Although slight albedo variations on the scale of several kilometers occur in the southwestern Arabia on occasion, these are interpreted as due to occasional water ice cloud cover due to their brief temporal appearance (none persist at the same location for more than a single image) and disassociation with topography.

Arabia crater #1. The first area of interest in Arabia Terra is an unnamed 90-km diameter crater located at 1.5°N, 26.5°E in the southern part of the region. A low-albedo splotch runs along the south to southwestern wall of the crater for about 45 kilometers and was classified as a surface with low dust cover by the DCI, as seen in Figure 37. On average, the western half of the low-albedo feature is about twice as wide as the eastern half (~15 km vs. ~8 km). CTX images reveal that the thinner eastern side consists of primarily smooth dark deposits lacking in obvious dune morphology. These deposits have filled a trough between the crater wall and central mound. Much of the dark material has draped over the northern wall of the trough, terminating as high as 250 meters above the floor in digitate patterns. The aforementioned wall exposes what appears to be a

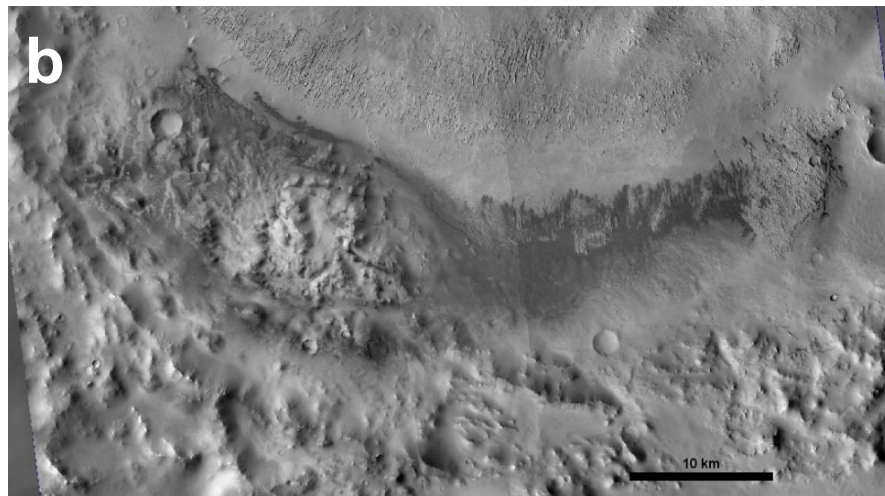
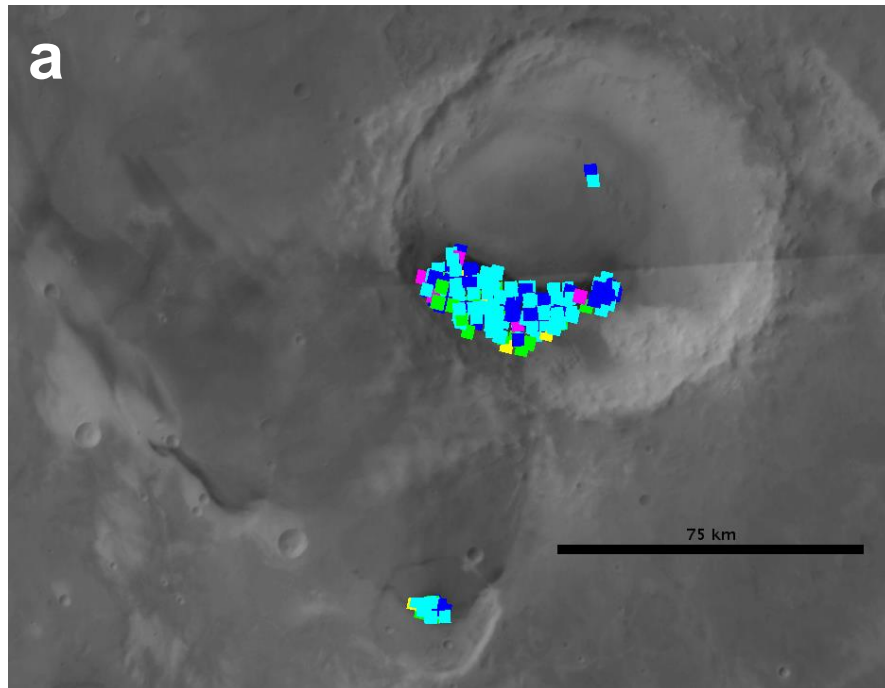


Figure 37. (a) Colored boxes denote TES spectra classified as having low dust cover by the Dust Cover Index (DCI) in and around Arabia crater #1. Background image is a MOC global mosaic. (b) CTX mosaic of the low-albedo sand deposits that form the dark splotch in the crater.

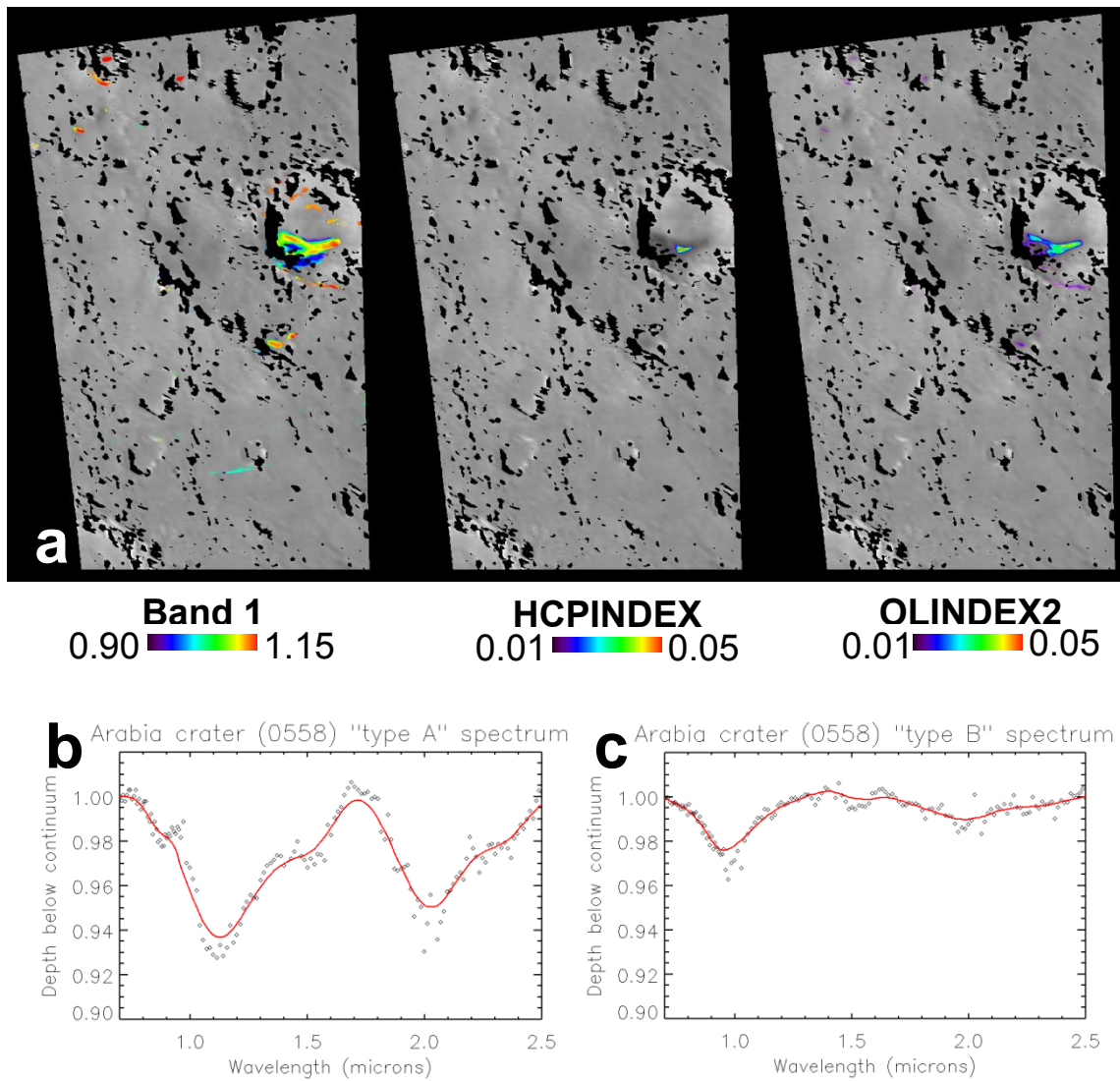


Figure 38. (a-c) OMEGA parameter maps for the 1 μm band center, high-calcium pyroxene, and olivine in Arabia crater #1. (b) Type A spectra are associated with dark sand deposits (warm-colored pixels in the band 1 center map). (c) Type B are associated with bright dustier surfaces (blues in the band 1 center map).

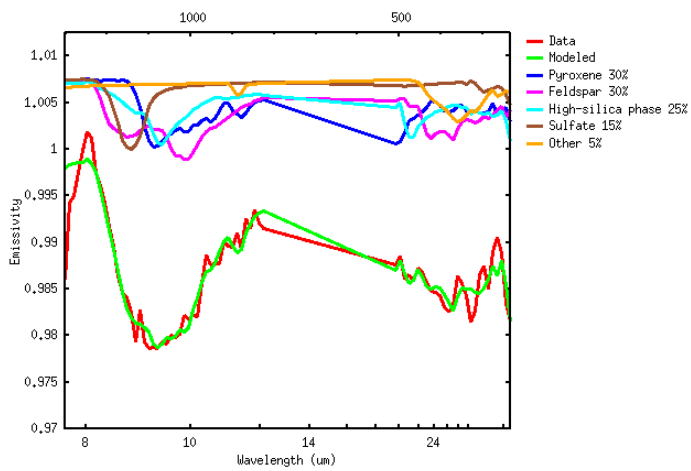
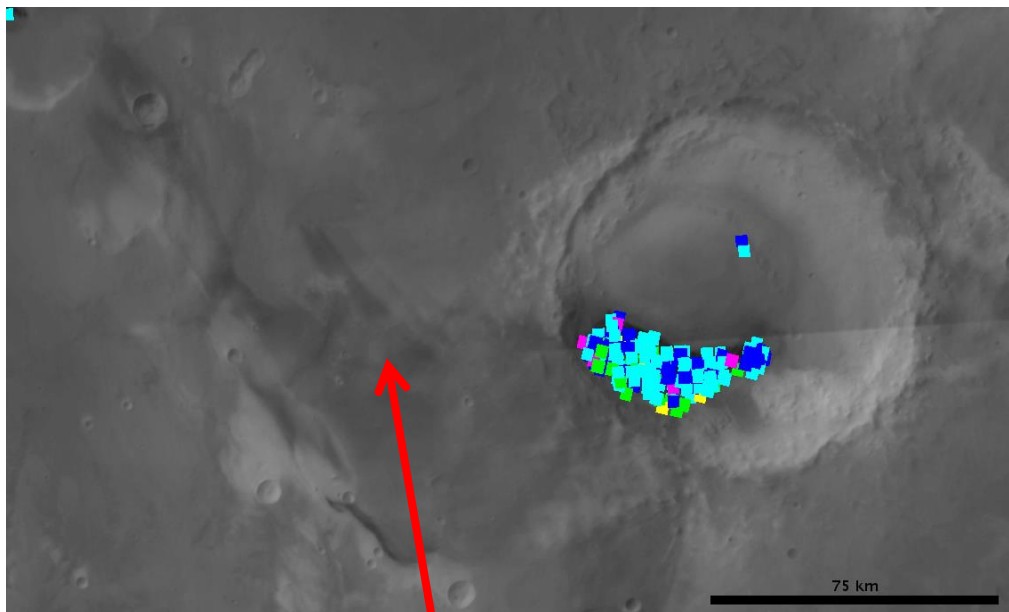


Figure 39. MOC mosaic of Arabia crater #1. No TES spectra were available from the low-albedo splotch within the crater. The deconvolved TES spectra shown are from the western part of the dark streak.

competent rocky unit with a highly eroded bulbous texture intermixed with erosional ripple surfaces. Some sections of the unit display irregular layering.

In the western half of the low-albedo feature, the dark deposits appear to diverge around a terrace that extends from the southwestern part of the crater wall (Figure 37). The deposits fill in a pair of troughs that are present above and below the terrace, leaving the local topographic high presumably sand-free and thus relatively bright. Like in the eastern streak, dark material here has a smooth texture and drapes over the preexisting bright ripple morphology.

The OMEGA NIR data from this crater are mapped in Figure 38. Spectra with a 1- μm absorption greater than 2% appear not only in the low-albedo splotch but also on parts of the adjacent crater and central mound walls, in addition to the streak that broadly extends onto the surface toward the southwest to a maximum distance of ~60 kilometers. Two spectral shapes are identified within the intracrater deposits, examples of which are shown in Figure 38b and c. The type A spectrum is characterized by a band 1 absorption near ~1.10 μm and a band 2 absorption near ~2.05 μm . This spectral shape correlates very well spatially with the observed distribution of low-albedo material that makes up the intracrater splotch and surface streak. In contrast, the band 1 absorption seen in type B spectra have a band 1 absorption that appear shallower and is positioned at shorter wavelengths (~0.98 μm). The band 2 absorption is even shallower but has extremely broad shoulders, extending from ~1.2 μm all the way out to the mid-infrared region. Type B spectra spatially correlate well with the crater walls and the rocky material exposed on the sides of the central mound. Furthermore, the terrace discussed earlier in this section is

resolvable in the band 1 parameter map in Figure 38. The higher wavelength band center signatures, represented by warm colors, diverge going east to west along the dark intracrater splotch to produce a blue “island” of lower wavelength band center signatures. This pattern highlights the strong correlation between the position of the 1- μm band center and albedo of the surface materials in this region.

HCPINDEX signatures are highest in the central part of the low-albedo deposits, where the smooth eastern sands first diverge around the relatively bright terrace. These signatures are highest at the center of the splotch and gradually grade outward to lower abundances. OLINDEX 2 signatures are much more extensive, covering the entirety of the intracrater dark deposits, as well as parts of the surface streak in very limited amounts. No LCP was detected in this area.

No high quality TES spectra were available within Arabia crater #1 despite the loosened data selection constraints used in this study. One set of spectra from the dark streak to the west of the crater was unmixed, the results for which are shown in Figure 39. The modeled modal mineralogy is approximately equal parts pyroxene, feldspar, and high-silica phases. This result is comparable with that from nearby Arabia crater #2, discussed below.

Arabia crater #2. A low albedo region within a second unnamed crater in southern Arabia also returned spectral signatures consistent with mafic mineralogy. The crater in question is 60 km in diameter and located 270 km southeast from Arabia crater #1 (3.3°S, 30.1°E; Figure 36). A fan-shaped low-albedo streak extends ~50 km to the south from an intracrater splotch. Smaller pockets of dark material exist in localized

depressions beyond the edge of the primary streak. The splotch is 25 km in length and consists of smooth low-albedo sand deposits that occupy the depression between the southern crater wall and the central peak based on CTX image observations (Figure 40). The north to western edge of the splotch has a digitate expression consistent with transport of material outward in these directions.; this observation is supported by the presence of a limited number of isolated barchan dunes on the outer fringes of the splotch and subtler dune forms closer to the interior.

The OMEGA results for Arabia crater #2 are largely similar to that of neighboring Arabia crater #1 and are shown in Figure 41. Two spectral shapes are present in the crater-streak area. Spectra from the intracrater splotch exhibit two major absorption bands centered near 1.10 and 2.05 μm . Spectra from the dark streak material have a relatively shallow single absorption at $\sim 0.95 \mu\text{m}$. The band 1 parameter has exceptionally widespread detections across the scene; signatures are most abundant within the intracrater splotch and the patchy dark material extending southwest from the fan-shaped streak. The streak itself is remarkably devoid of spectra with 1- μm bands deeper than 2%. The splotch exhibits the highest HCPINDEX values of any location analyzed in this study; the central interior portion have parameter values greater than 10%, which is twice as high as typical values in other areas of interest. Additionally, an area of lower HCPINDEX signatures ($\sim 5\%$) is located along the southern margin of the streak. LCPINDEX signatures are comparatively less prevalent and are limited to the south to southeastern sections of the streak. LCPINDEX values do not exceed

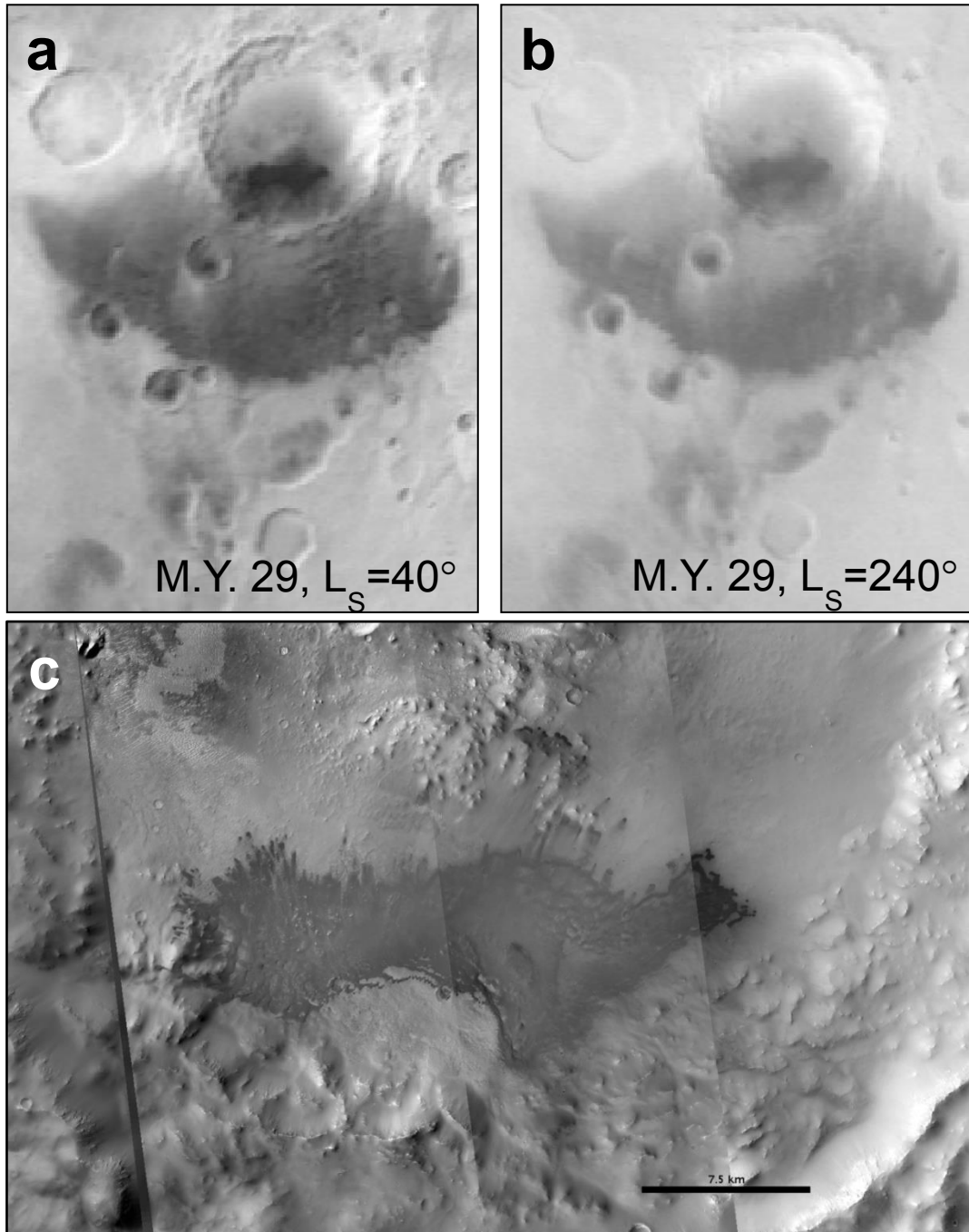


Figure 40. (a) MARCI mosaic of Arabia crater #1 (3.3°S, 30.1°E) showing the low-albedo intracrater splotch and fan-shaped streak during southern autumn. (b) Same observation area as 40a, but during the opposite time of year (southern spring). Note that the splotch and streak have brightened from 40a but are still easily distinguishable from the bright adjacent terrain. (c) CTX mosaic of the low-albedo intracrater splotch.

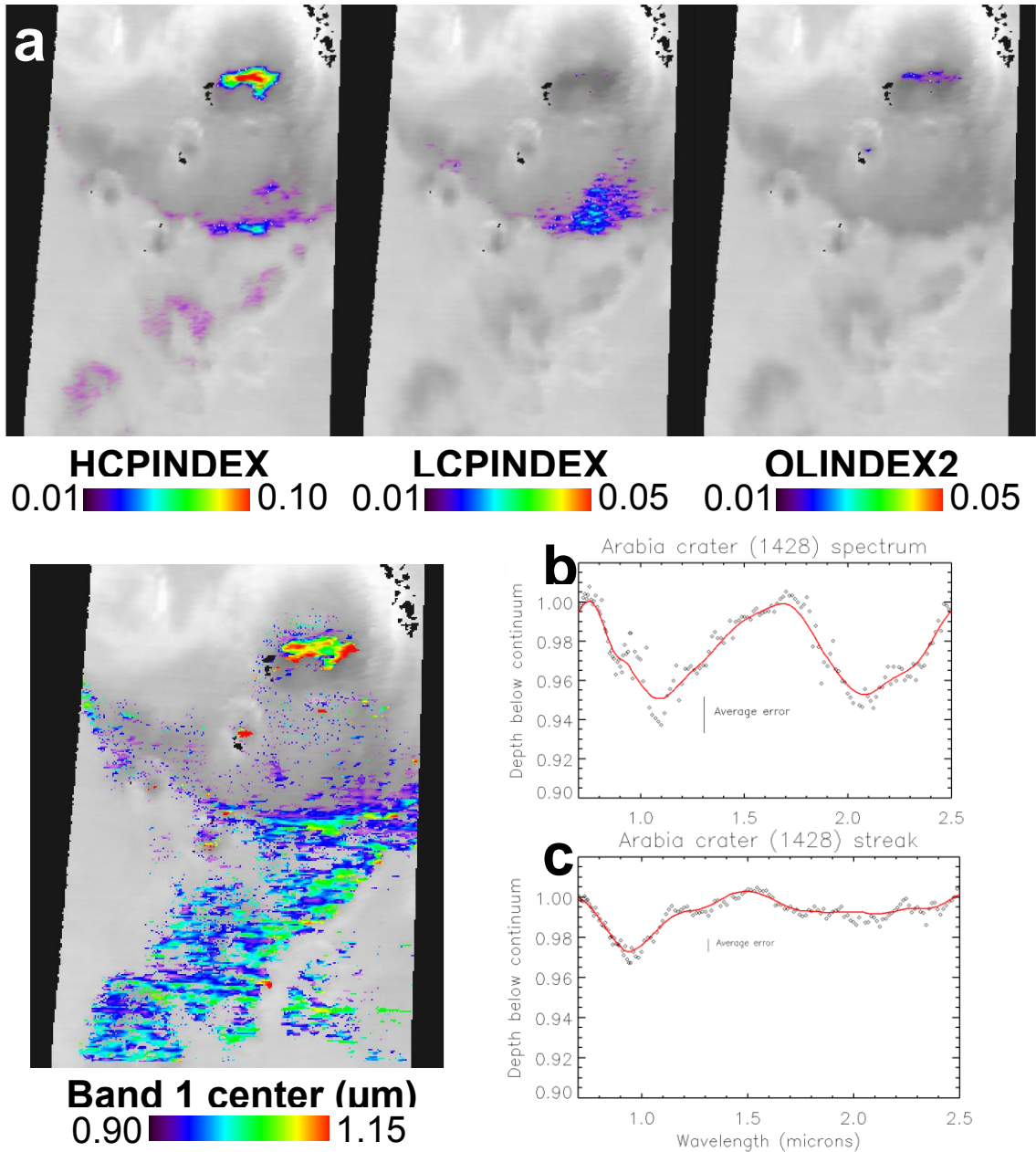
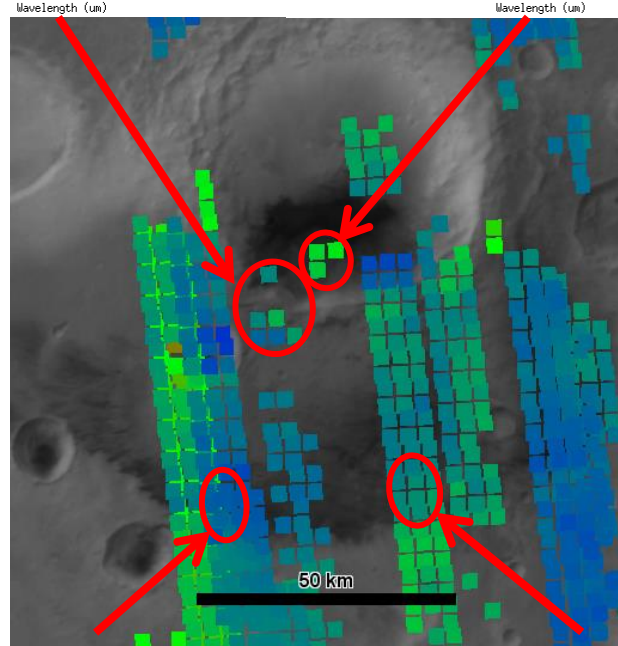
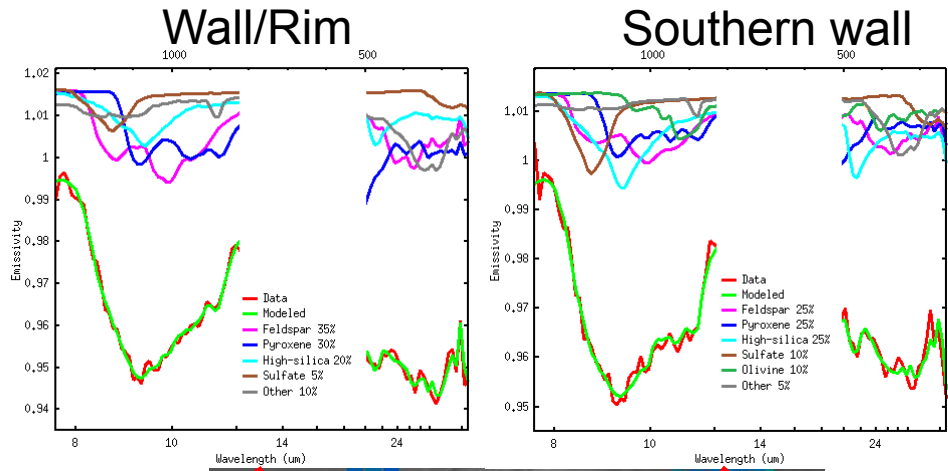


Figure 41. (a) OMEGA parameter maps for high-calcium pyroxene, low-calcium pyroxene, olivine, and the 1- μm band center. (b) Type A spectra are associated with dark sand deposits (warm-colored pixels in the band 1 center map). (c) Type B are associated with brighter dustier surfaces (blue colors in the band 1 center map).



West streak

East streak

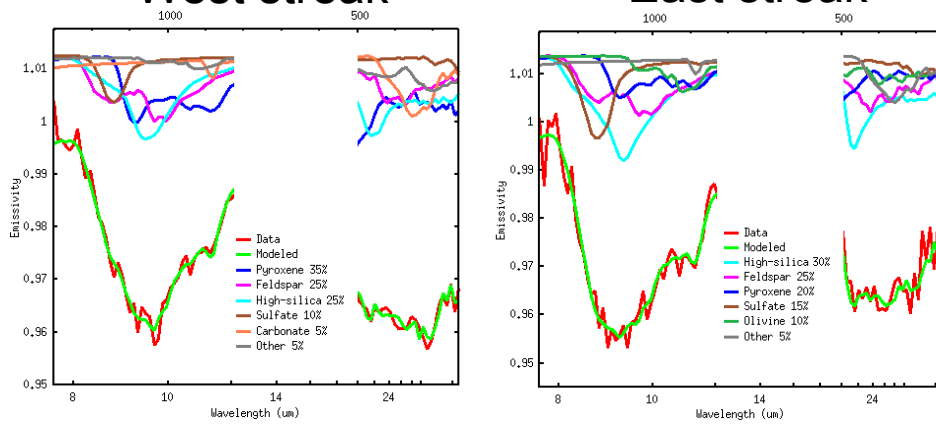


Figure 42 (previous page). TES deconvolution results for Arabia crater #2. Red ellipses denote the spectra that were averaged and unmixed to produce each plot. Background image is a MOC mosaic.

3% anywhere in the scene. OLINDEX2 signatures are similarly scarce, limited to values <2% within the intracrater splotch only.

TES deconvolutions for Arabia crater #2 are shown in Figure 42. ocks 2731 and 5284 sample the western and southern portions of the splotch, respectively. While the derived mineralogies differ (35% feldspar, 30% pyroxene, 20% high-silica phase for ock 2731; 25% feldspar, 25% pyroxene, 25% high-silica phase for ock 5284), the feldspar to pyroxene ratio is similar for both areas. TES spectra were also collected from different locations in the streak; ock 3800 samples the western streak while ock 5284 covers the eastern end. Unmixing results show that pyroxene, feldspar, and high-silica phase concentrations are consistent for both areas (35%, 25%, and 25%, respectively).

DISCUSSION

Tharsis

Of all the low albedo “windows through the dust” areas of interest observed in Tharsis, Arsia Mons exhibits the most promising mineralogical signatures. Analysis of OMEGA data reveals that the low-albedo materials exposed at Arsia Mons during the annual dust-clearing event exhibit the deepest absorption features and show remarkable spatial coincidence with detected mineral signatures. The data suggest that the most likely mineralogy at the southeastern flank of Arsia Mons is a primary LCP-HCP intermediate with potential minor contributions from iron-bearing glass and olivine.

The averaged spectrum from the southeastern flank of Arsia Mons is most consistent with a mixture of LCP and iron-bearing glass (see Figure 7). While the locations of the 1- and 2- μm absorption bands are suggestive of pyroxene in general, the exact band centers are consistent with a range of known species. The presence of a broad absorption band near 1.95 μm is consistent only with LCP among the mineral species considered in this study. The 1- μm absorption band is centered in the 1.0 to 1.05 μm region, which suggests that any LCP present is mixed with at least one other species with a characteristically higher-wavelength 1- μm band center. The most likely mixed component is HCP, with perhaps additional contributions from volcanic glass. The depth of the 2- μm band is consistent with HCP, as near-IR spectra of iron-bearing glass do not typically have this absorption. However, an LCP-HCP mixture would be expected to have a 1- μm absorption closer to the characteristic 0.9 μm band position of LCP (*i.e.*, at wavelengths shorter than 1.0 μm) rather than the 1.0 to 1.05 μm position observed in the

OMEGA spectra (*e.g.*, Adams, 1974a; Cloutis and Gaffey, 1991). Contribution from iron-bearing glass would be another way to shift the 1- μm band to longer wavelengths, although the 2- μm band would likely be considerably shallower due to the lack of a strong 2- μm band in iron-bearing glass spectra. In either case, spectra of mineral mixtures taken in the laboratory indicate that the character of the 1- μm band is dominated by OPX until HCP or glass concentrations reach $\sim 75\%$ in a simple two-phase mixture (Singer, 1981; Horgan *et al.*, 2014). The discontinuity in the long-wavelength edge of the 1- μm band at 1.3 μm may indicate that olivine is also present in minor amounts.

The detection of glass would not be surprising. For example, recent mineralogical and geomorphological studies have proposed that explosive volcanism at Tharsis played a significant role in Mars' volcanic history. This hypothesis stems from a number of separate observations, including the presence of extensive iron-bearing glass in the northern lowlands (Horgan and Bell, 2012), ash deposits present near the edifices themselves (Mouginis-Mark, 2002) and as layered stacks that thin out with increasing distance from Tharsis (Hynek, 2003), pyroclastic depositional features identified by the Spirit rover at Gusev Crater (Squyres *et al.*, 2007), and predictions of widespread pyroclastic deposits based on explosive eruption and atmospheric circulation models (Wilson and Head, 2007; Kerber *et al.*, 2012). If the Tharsis volcanoes did in fact source such material via explosive eruptions, we could easily expect to see iron-bearing glass deposits near the vents.

More surprising is the potential detection of LCP as a significant contributor to the mineralogy at Arsia Mons. Previous mineralogical surveys of the martian surface

reported that LCP is limited to highly cratered Noachian-aged terrain. Crater counting models predict an average age of about 200-1000 Ma for the upper 100 m of Arsia Mons (Hartmann, 2005). Lava flows located within the caldera, which represent the most recent recognizable volcanic activity on the edifice, have been dated at less than 100-Ma (Hartmann *et al.*, 1999). The observed LCP detections at this location are more likely due to the presence of a pyroxene with intermediate calcium content, producing deep and distinct absorption bands near 1- and 2- μm . The more precise band positions are ~ 1.02 and $1.98 \mu\text{m}$, but these do not match any single specific known pyroxene species and therefore further suggest significant contribution from additional minerals (Cloutis and Gaffey, 1991). Figure 43 shows a pair of pyroxene phase diagrams with the expected wavelength positions of the 1- μm and 2- μm absorption bands for various pyroxenes. The band positions from Arsia Mons, indicated by red boxes, do not overlap. The closest approximate would be an augite or pigeonite, as these species occupy the space between the red boxes, but both OMEGA and TES data suggest that contribution from additional minerals may be more likely.

TES deconvolution results for the southeastern flank of Arsia Mons bear strong similarity to the Group 1 spectral class of Rogers and Christensen (2007), while the plains to the southeast of Arsia Mons are closer in composition to Group 4. The modal mineralogies of the four spectral classes is shown in Figure 44. Group 1 is characterized by high concentrations of high-silica phases and depletion in pyroxene and olivine. Among the three most common species (pyroxene, plagioclase, and high-silica phases),

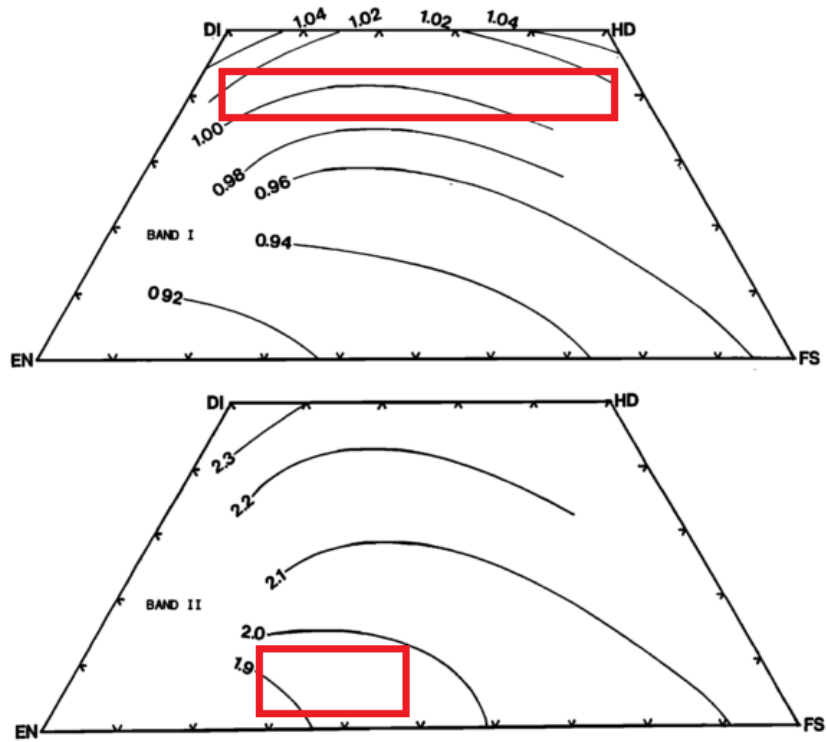


Figure 43. Pyroxene phase diagrams from Cloutis and Gaffey (1991) with labeled black lines showing the expected wavelength positions of the 1- μm (top) and 2- μm (bottom) bands for various pyroxene species. The red boxes denote the approximate areas where the spectrum from Fig. 7 would plot.

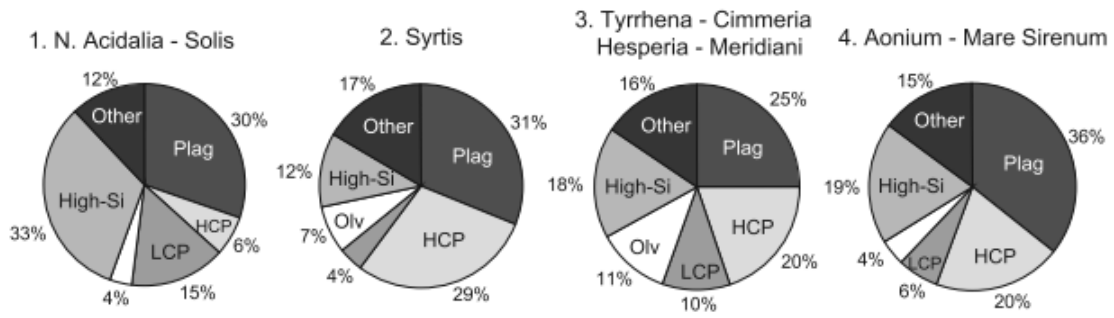


Figure 44. Modal mineralogies for the four spectral classes of Rogers and Christensen (2007). This figure is borrowed from that work.

the modeled mineral endmember abundances for rock 4673 do not deviate from the expected Group 1 modal mineralogy by more than 5%, which is the nominal detection limit of TES. The primary occurrence of Group 1 on Mars is in the plains of Northern Acidalia, where extensive weathered volcanic glass deposits have recently been detected (Horgan and Bell, 2012). The detection of abundant high-silica phases on Arsia Mons is likely due to the presence of volcanic glass, given the similarities in modal mineralogy between these surfaces and Northern Acidalia. These interpretations would also be consistent with the potential glass detections inferred from OMEGA data above. Although Northern Acidalia dominates the Group 1 type regions, one such region is located in Solis Planum and is in fact the closest type region to Arsia Mons of any of the four spectral classes, as seen in Figure 45.

Group 4 is characterized by a high plagioclase to pyroxene ratio and depletion in olivine relative to other groups. The type regions for Group 4 are the albedo features of Aonium Sinus and Mare Sirenum, which are roughly divided between Noachian and Hesperian surfaces. Pyroxene, feldspar, and high-silica phase concentrations do not deviate from the defined Group 4 composition by more than 6%. The type regions for both Aonium Sinus and Mare Sirenum are located approximately adjacent to Daedalia Planum, a lava plain at the southern edge of Tharsis that originates near Arsia Mons and extends in a southward direction. The similarities between the composition derived from this study and that of Group 4, combined with the relative close proximity between Arsia Mons and these type regions (Figure 45), is an encouraging indication that they are represented by a similar common mineralogy. Additionally, Group 4 has the highest

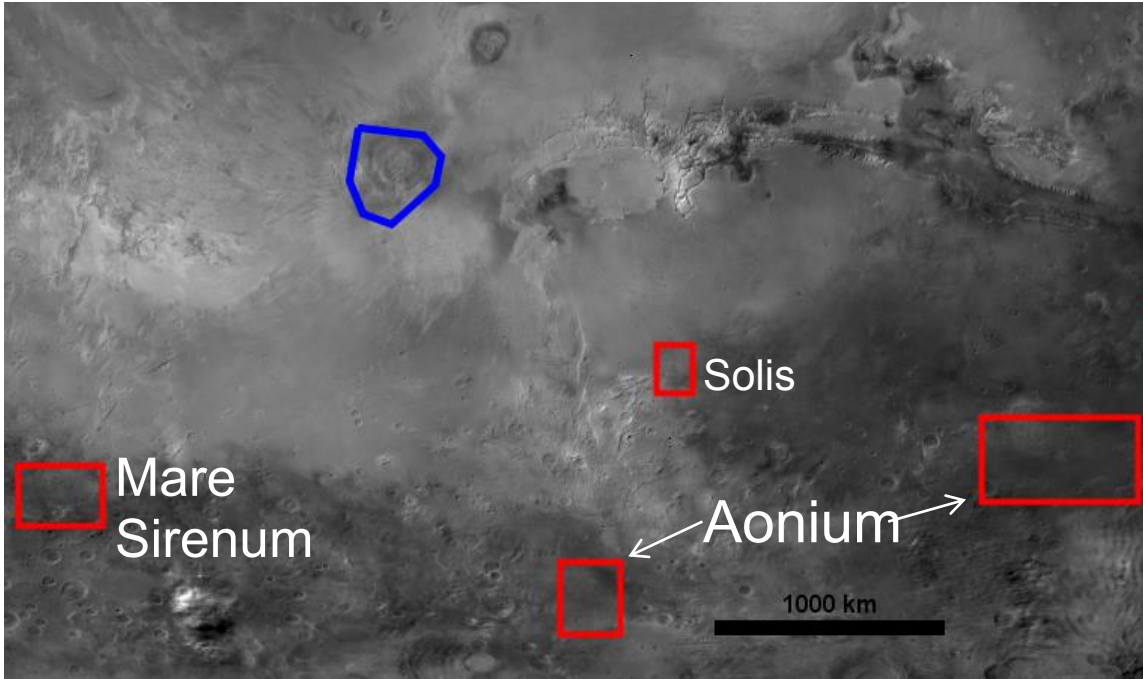


Figure 45. The location of the Arsia Mons area of interest (blue outline) in relation to type regions of the Rogers and Christensen (2007) spectral classes (red boxes). Aonium and Mare Sirenum are members of Group 4 while Solis is a member of Group 1.

average elevation of the compositional groups; Rogers and Christensen (2007) reported that the spectra with concentrations of Group 4 of at least 0.5 were predominantly found at elevations of at least 500 m. The elevation of the Arsia Mons area of interest varies from 7,500 m near the plains to 15,000 m on the upper flanks.

Aonium Sinus and Mare Sirenum, of which the Group 4 composition is characteristic, have been characterized as flat, featureless lava flows and sedimentary deposits (Greeley and Guest, 1987). These surfaces are classified as part of the Smooth member of the Plateau Sequence that dominates most of the southern highlands. Although the majority of the Plateau Sequence originates from the Noachian epoch, the Smooth unit is the youngest member of the sequence and its formation is thought to have lasted through the early to mid-Hesperian, ceasing approximately concurrently with the onset of volcanism in the highlands paterae, Syrtis Major, and Elysium Planitia regions. If the surface bedrock of Arsia Mons indeed shares the same modal mineralogy as the youngest member of the Plateau Sequence of the southern highlands, this might imply that magmas in the southern Tharsis-Daedalia region underwent minimal evolution from the mid-Hesperian, when the Plateau Sequence had completely formed, to mid-Amazonian, when the lavas that compose the area of interest on the flanks of Arsia Mons began erupting. Of course, the limited availability of high-quality OMEGA and TES data in the Tharsis interior due to the opacity of the surface dust mantle means that additional near- and thermal infrared data focused on the low-albedo surfaces of Arsia Mons are required before this hypothesis can be confidently tested.

Unfortunately, Arsia Mons was the only major volcanic construct in which spectral features diagnostic of mafic mineralogy were detected in this survey. Other low albedo “windows” on or near volcanoes located in dusty regions exhibited flat and featureless spectra, despite the data having been taken during the annual dust-clearing event in spring to early summer in the northern hemisphere. Although MARCI observations were matched with OMEGA hyperspectral data as closely as possible with respect to season, the bulk of the OMEGA data obtained for this study were collected before midyear of M.Y. 28, which is the period from which the first MARCI images used in the quadrangles were taken. Having a larger selection of NIR data to work with, where it is possible to match the minimum albedo value for each region on an annual basis more precisely with the corresponding spectral data, may offer more promising results. The exceptionally thick dust cover in Tharsis, which is estimated to be 1 to 2 meters thick (Christensen, 1986), may require particularly strict matching between the visible and NIR observations.

Quantitative albedo data from MARCI indicate that there are indeed notable variations in albedo values between the southeastern flanks of Arsia Mons and other surfaces in Tharsis that darken during the spring. Table 4 shows the average Lambertian albedo for various volcanic constructs and dark plains features during M.Y. 29, $L_S = 20\text{--}40^\circ$, which coincides with the peak of the surface darkening event observed in the MARCI observations in Figures 2 and 7. These data were converted from radiance factor (I/F) values outputted by MARCI mosaicking scripts to an approximate Lambertian albedo (Bell *et al.*, 2009; Wellington and Bell, 2013). The absolute radiometric

Table 4.

MARCI Lambertian albedo values for areas of interest in Tharsis.

| Feature | Lambertian albedo |
|-----------------------|--------------------------|
| Average dusty surface | 0.37 |
| Ascraeus Mons | 0.33 |
| Ulysses Tholus | 0.33 |
| Ceranius Tholus | 0.32 |
| Dark plains | 0.32 |
| Pavonis Mons | 0.30 |
| Arsia Mons (SE slope) | 0.27 |
| Arsia Mons (SE plain) | 0.27 |

accuracy of MARCI is <10%, although estimates of Lambertian albedo introduce additional uncertainties due to atmospheric effects and the actual martian surface deviating from ideal Lambertian reflectance. Still, all of the areas of interest in Tharsis that did not yield positive mineral signatures exhibit albedos in the range of 0.30 to 0.33 in contrast to the value of 0.37 for typical bright dusty terrain during this season. The albedos for southeastern Arsia Mons are even lower: the flank that overlaps with the OMEGA observation ORB3342_4 and the nearby plains exhibit an average albedo of 0.27. These albedo values suggest that there are real brightness differences between Arsia Mons and the rest of Tharsis during the springtime dust-clearing events, which implies varying rates of dust removal. Johnson *et al.* (2002) modeled the thermal infrared spectral effects of dust cover on basalt and found that spectrally flat dust coatings reach a “saturation thickness” at ~100 μm , after which additional dust cover does not significantly alter the albedo of the surface. That albedo variations are observed in Tharsis and affect the ability to extract high-quality infrared remote sensing data from this region might suggest that the “saturation thickness” of dust is an upper limit on the dust mantle thickness during this time period.

Previous studies have reported persistent water-ice cloud cover over the nearby southwestern flank of Arsia Mons during all seasons (Noe Dobrea and Bell, 2005). This phenomenon has not been observed to occur at other Tharsis volcanoes and might imply unique surface-atmosphere interactions at Arsia Mons that could generate stronger slope winds and more effectively lift dust off the surface.

Christensen (1986) also proposed that darkening events in Tharsis represent removal of dust from rocks and other coarse-grained material only, rather than from the actual bedrock surface. While it is difficult to lift dust airborne from a flat surface, any dust covering rocks that project into the local wind flow could be more easily removed. The exposure of these dark rocks would contribute to the observed darkening effect from remote sensing data, but the low rock abundance relative to the overall surface area in the Tharsis region would mean that most of the surface is still mantled by dust.

Elysium Planitia

Although Elysium Planitia contains a number of prominent volcanic edifices, most notably Albor Tholus, Elysium Mons, and Hecates Tholus, these constructs and the surrounding plains remained remarkably bright throughout the MARCI observation period and, not surprisingly, did not exhibit any spectral features indicative of mafic mineralogy. However, a variety of low-albedo surface features, including cliff, intracrater, and plains deposits did return high-quality OMEGA spectra. These areas provided a fairly good geographic distribution, sampling the southern and eastern boundaries of Elysium Planitia in addition to the interior. One of the areas of interest in particular, Elysium crater #1, is located less than 600 km of Albor Tholus and appears to sample local bedrock. Results from each of the areas of interest are discussed individually below.

Williams Crater. Observations of Williams Crater indicate that the closed depression along the southwestern wall contains a different lithology than the dark

deposits exposed elsewhere in the low-albedo splotch and is more representative of the local bedrock. The closed depression and the surrounding terrain have the lowest albedo of the entire splotch, which suggests that this location is sourcing new dark deposits. Although the splotch gets brighter with increasing distance away from the closed depression, the lack of dune forms in CTX images of the area indicates that dark material is not being actively transported to the northeast. In fact, the few dunes that are visible within small sub-kilometer scale impact craters exhibit an overall E-W trend, indicating local N-S wind directions.

The central to eastern portions of the Williams Crater low-albedo splotch are composed primarily of a high- and low-calcium pyroxene mixture. The absorption band centered near 1.05 μm is consistent with HCP. Although this band center also matches that of olivine, the narrow and symmetric nature of the observed absorption is inconsistent with olivine being present in any significant amount. The nearby reflectance maximum at 1.3 μm is more indicative of LCP, rather than the high-calcium phase. Another broad absorption is centered at 2.0 μm , which is in the mid-region between where LCP and HCP exhibit a $\sim 2\text{-}\mu\text{m}$ band (1.9 and 2.2 μm , respectively; Singer, 1981; Cloutis and Gaffey, 1991). The index parameter maps support these observations from the averaged spectrum; HCPINDEX and LCPINDEX signatures are present throughout the central to eastern parts of the intracrater splotch at varying strengths, while OLINDEX2 signatures are localized to a small cluster of pixels in the western end of the splotch. LCP becomes the dominant mafic phase toward the eastern end of the splotch, where the terrain becomes smoother. HCP is still present in minor amounts in the eastern

splotch, but olivine becomes undetectable ~10 km away from the closed depression. The low-albedo deposits within the depressions to the west of Williams Crater appear compositionally similar to the eastern splotch, containing greater amounts of LCP, less HCP, and no olivine.

TES results from the western and eastern parts of the Williams Crater splotch indicate the same general composition. The modal mineralogy of 30 to 35% pyroxene, 25% feldspar, and 20% high-silica phase is an excellent match with the Group 3 compositional group from Rogers and Christensen (2007), which is representative of typical southern highlands surfaces. The only significant compositional difference between the areas is olivine being modeled at 10% in the eastern splotch. This result furthers the connection between Williams Crater and Group 3, as this group is the most olivine-rich of the considered spectral classes at 11%. Although olivine is deconvolved from the averaged spectrum of both parts of the splotch, the derived concentrations from the western splotch are below the detection limit of TES while that of the eastern splotch is at the limit. This result is not consistent with OMEGA data from the same area, which indicated that olivine is present in minor amounts in the western splotch but not in the east. It should be noted that overall concentrations are still near the detection limit, so the spatial distribution of olivine in Williams Crater is still unclear.

Pettit Crater. The low-albedo floor deposits in Pettit Crater show signatures primarily from high-calcium pyroxene with smaller contributions of low-calcium pyroxene. The 1- and 2- μm absorption bands together are diagnostic of a pyroxene-dominant composition. The 2- μm absorption is centered at ~2.15 μm , which most closely

associates with high-calcium pyroxene. The position of the reflectance maximum between the two bands at $\sim 1.7 \mu\text{m}$ is also consistent with HCP. The absorption centered at $\sim 1.0 \mu\text{m}$ is likely a single composite band of LCP and HCP, whose 1- μm bands occur at ~ 0.9 and $\sim 1.05 \mu\text{m}$, respectively. Both diagnostic pyroxene bands appear to be shifted toward shorter wavelengths by the presence of low-calcium pyroxene, as the positions of the two bands for clinopyroxenes are typically 1.05 and 2.35 μm (Cloutis and Gaffey, 1991). TES deconvolutions for multiple areas near the intracrater splotch of Pettit Crater show a uniform mineralogy consisting of 30% pyroxene, 25% feldspar, and 30% high silica phases (Figure 16). The pyroxene and feldspar concentrations are an excellent match with Group 3, although the concentration of high-silica phases is substantially overestimated by comparison. Unmixed spectra from the streak of Pettit Crater also exhibit abnormally high concentrations of high-silica phases, which further suggests the widespread presence of these materials; however, the actual concentration in the streak is likely not being modeled entirely accurately due to the noisiness of the observed 8 to 12 μm silica absorption band, especially on the longer wavelength edge where the modeled fit is noticeably poor.

Elysium crater #1. The mineralogy of Elysium crater #1 is dominated by high-calcium pyroxene with a possible minor contribution from olivine. The averaged OMEGA spectrum from the eastern part of the streak, which is assumed to represent displaced intracrater splotch material, has primary absorption features at 1.05 and 2.10 μm , which are both within the diagnostic wavelength ranges for HCP (Figure 18). The reflectance maximum between the two absorption bands at $\sim 1.7 \mu\text{m}$, rather than shorter

wavelengths, is also representative of HCP. The presence of olivine is inferred from the highly asymmetric nature of the 1- μm band. Because there is substantial overlap between the position of the 1- μm band center for HCP and olivine, it is often difficult to distinguish using just this criterion alone. These interpretations of the averaged spectrum are supported by the parameter maps, which show widespread HCP and olivine signatures throughout the central and eastern parts of the streak. The western third of the streak largely lacks signatures that can be attributed to the pyroxene or olivine index parameters. These gaps in the parameter maps might represent surfaces that have a thicker local dust mantle and fewer low-albedo particles, leading to diminished mineral signatures. This interpretation is consistent with the HCPINDEX and OLINDEX2 parameter maps from Figure 18, for which peak signatures occur in the eastern streak and gradually diminish in strength towards the west. This effect is expected if the observed low-albedo streak formed by the transport of dark sediment from the crater, as fewer coarse grains would be available to saltate to such distances from the source. Alternatively, the mineralogy here might be characterized by a more thorough mixture of multiple phases (pyroxenes, olivine, glass, etc.), which would decrease the parameter values for each individual phase.

The TES results from the streak of Elysium crater #1 provide an excellent match with the Group 3 spectral class of Rogers and Christensen. The derived modal mineralogy of 35% pyroxene, 25% feldspar, and 20% high-silica phase differs from Group 3 by no more than 5% for each phase. The type regions for Group 3 are Cimmeria Terra, Hesperia Planum, Sinus Meridiani, and Tyrrhena Terra. With the exception of

Sinus Meridiani, these regions straddle the dichotomy boundary on the southern edge of Elysium Planitia and are the closest type regions to Elysium crater #1. TES spectra from the central peak and low-albedo splotch of Elysium crater #1 were also deconvolved. Both revealed a contrasting mineralogy to that of the streak, which is shown in Figure 20. The most notable difference in the crater interior spectra is a depletion of feldspar to near-detection limit concentrations, coupled with a substantial increase in olivine. The central peak in particular exhibits more extreme degrees of each trend, containing 10% feldspar and 20% olivine. Central peaks often sample material from the deep crust to upper mantle, so the comparatively primitive basaltic composition and enrichment in olivine observed in these rocks is not unexpected.

The OMEGA data from the isolated low-albedo area to the west of the primary streak exhibit slight differences from the streak and are indicative of an HCP-glass mixture (Figure 19). The high-wavelength band centers of both the 1- μm and 2- μm bands are consistent with HCP, which likely represents the dominant phase. The 1- μm band center position of 1.1 μm is beyond the range of HCP but near the lower boundary of 1- μm absorptions of iron-bearing glass, which suggests contribution from glass. This area is probably representative of the local Elysium plains composition rather than an extension of the streak material, given the observation that it is discontinuous from the streak and appears to have a slightly different mineralogy. Laboratory studies have estimated that aggregate sand with composition similar to martian dust can only saltate for a maximum of ~150 km before abrasion with the surface reduces the size of the particles to dust-sized particles (<63 μm), even if the grains are cemented (Greeley and Kraft, 2001). At grain

sizes below 63 μm , sand is incapable of saltating and is lifted into suspension. The center of the low-albedo isolated area is ~ 150 km from the rim of Elysium crater #1, which is near the upper limit of aggregate sand survivability for Mars. It is inferred here that much of the Elysium plains contain a significant amount of iron-bearing glass deposits, which is represented by the isolated low-albedo area to the west of Elysium crater #1. The crater's primary low-albedo streak is formed from saltating sand grains from the crater interior, which have buried the glass that otherwise covers the plains. It should still be noted that olivine grains have hardness comparable with quartz and, after being rounded by initial mechanical weathering, have very high survivability on Mars (*e.g.*, Sullivan *et al.*, 2008; Greeley and Kraft, 2001). Therefore it cannot be completely ruled out the isolated low-albedo region may be partially sourced by the streak material.

The strong correlation in modal mineralogy between Elysium crater #1 and the Group 3 spectral class suggests that Group 3 is at least a substantial, if not dominant component of the materials located at interior of Elysium Planitia, of which Elysium crater #1 is a part. The question of whether these materials represent the local bedrock is less clear, given that the overall area of interest produced multiple compositions. Spectra from the streak and crater interior are consistent with a mixture between HCP and olivine, albeit at varying concentrations relative to each other, so it is likely that the local bedrock would primarily carry these phases as well.

Aeolis west. The Aeolis west spectrum is representative of an HCP-glass mixture. While the general shape of the 1- μm band bears remarkable similarity to that of olivine due to the presence of shoulders located on both the short and long wavelength sides, and

OLINDEX2 is the only index parameter detected at any significant concentration (>5%), the location of the band center at >1.1 μm indicates that any olivine present is likely mixed with another component. Of the mineral species considered in this study, iron-bearing glass is the only one with 1- μm absorption beyond $\sim 1.05 \mu\text{m}$. Neither olivine nor iron-bearing glass is characterized by a 2- μm absorption band, however. The presence of this band beyond 2.0 μm is highly indicative of HCP. A glass component mixed with HCP would account for the 1- μm band center shifted to >1.10 μm as well as the diminished 2- μm band. Mixtures of HCP and iron-bearing glass have been recognized to produce spectral signatures in the laboratory that are difficult to distinguish from that of olivine by itself (Horgan et al., 2014). Deconvolution results from TES ock 6224, which overlaps with the nominal area of interest, are remarkably similar to the modal mineralogy of the Group 2 spectral class from Rogers and Christensen (2007), as the modeled plagioclase, pyroxene, and high-silica phase concentrations are all within 4% of the reference values (Figures 22 and 44). The additional TES spectra from ock 3759, which spatially correspond to an extension of the low-albedo deposits outside of the OMEGA image, have a similar spectral shape to ock 6224 but provide different mineralogical results. The mineralogy observed from this area bears closer similarity to the high-silica-phases-rich, plagioclase-poor Group 3. This presence of these two groups is not surprising and may be explained by the fact that the closest type regions from Rogers and Christensen (2007) to Aeolis west are from those of Group 2 and Group 3, as evident in Figure 46. Still, the contrast in mineralogy between these two areas is remarkable given the fact that they are part of the same continuous low-albedo feature

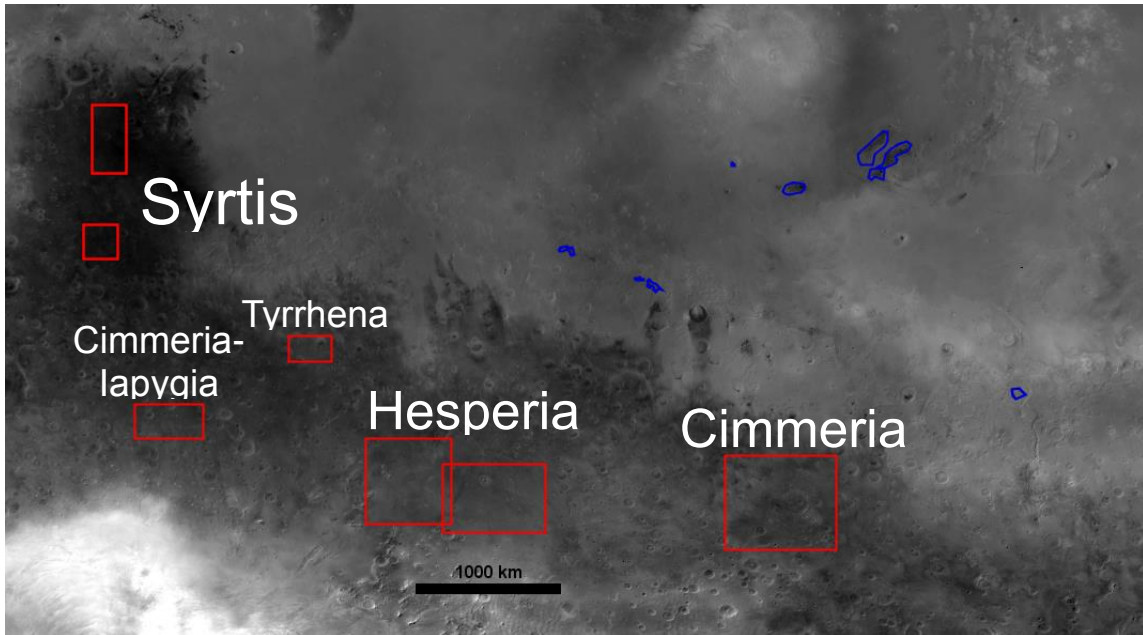


Figure 46. The location of the Elysium Planitia areas of interest (blue outlines) in relation to type regions of the Rogers and Christensen (2007) spectral classes (red boxes). Syrtis is the type region for Group 2 while the other areas are members of Group 3.

and have the same morphological expression. A composition rich in high-silica phases is consistent with OMEGA data at this same location, in particular the interpretation that the 1- μm absorption band has been shifted beyond 1.10 μm due to the presence of iron-bearing glass.

Aeolis east. The OMEGA data from Aeolis east produced an enigmatic averaged spectrum (Figure 23), but the presence of low-albedo deposits in Knobel and Robert Sharp Craters just ~100 km to the south may offer a good representation of the regional bedrock mineralogy in its place. The fact that the absorption band edges and reflectance maxima are located at the same positions suggests that the bedrock in these regions share the same general composition. The positions of the 1- and 2- μm band centers of the Knobel Crater dark deposits are representative of HCP. A mixture with olivine is possible given the position and shape of the 1- μm band, which appears to be a composite of three overlapping bands; however, the deep 2- μm band indicates that there is no significant contribution from olivine. The decrease in strength of both the HCP and olivine indices from the low-albedo surfaces of Hesperia Planum in the south towards the area of interest in the north is likely due to greater mixing with dust or weathered glass. The edges of the absorption bands and reflectance peaks for both spectra are at the same positions, the main difference being variations in the absorption band depths. The primary absorption bands from the cliff base deposits are shallowest and have additional minor bands in the 1.3 to 1.5 μm region that are unattributed to any mineral considered in this study. The TES data from this region provide inconclusive results with respect to similarities with the Rogers and Christensen (2007) spectral classes. Spectra from ock 3809, which

correspond to the central part of the cliff base deposits, do not match any spectral class well due to high concentration of high-silica phases relative to plagioclase despite a good visual fit between the modeled and observed averaged spectrum. Spectra from ock 3897, which are located near the eastern end of the cliff base deposits, exhibit exceptionally high feldspar concentrations (40%) and a low pyroxene to feldspar ratio. These observations align most closely with Group 4, although pyroxene and high-silica phase concentrations are comparatively underestimated; however, it should also be noted that the observed TES spectrum is poorly modeled from 9 to 11 μm and resulting estimates likely deviate from the actual mineralogy.

Cerberus west. The derived composition of the Cerberus Fossae region is most consistent with an HCP-glass mixture. The positions of the 1- μm band center from various locations and morphologic features varies from 1.05 μm to 1.15 μm , a range that can almost entirely uniquely be attributed to iron-bearing glass among species considered in this study. The asymmetric shapes of these bands, in particular the shorter-wavelength edge having a greater slope than the long-wavelength edge, is consistent with HCP-glass mixtures detected by OMEGA in other regions of Mars (Horgan et al., 2014). The presence of an additional absorption between 2.05 and 2.10 μm implies the presence of HCP, the only species that major bands in this wavelength region are associated with.

TES-derived mineralogy from the central to east parts of the albedo feature (ock 3808) does not match any single compositional group from Rogers and Christensen (2007) well. Pyroxene concentrations are ~40% and relatively high compared to areas of interest. Feldspar concentrations range from 20 to 30% while high silica phases appear to

be consistent at 15% throughout the entire albedo feature. Groups 2 and 3 seem to be the best approximates for the observed mineralogy given the high concentrations of pyroxene and relative scarcity of high-silica phases in this area. Spectra from the western part of the albedo feature are not extreme in this regard and actually are a fairly good match with the typical highlands material of Group 3. The unique detection of olivine at 10% concentrations at this location only furthers the association.

Cerberus crater. TES results from the Cerberus crater more closely fit the Group 3 spectral class from Rogers and Christensen (2007) than the albedo feature, especially data from the low-albedo streak surrounding the crater. Deconvolutions from the western and eastern parts of the streak both exhibit estimated a modal mineralogy that does not deviate from that of Group 3 by more than a 5% among pyroxene, plagioclase, and high-silica phases. Of particular note is the spectrum from the western part of the streak, which was modeled to have 15% olivine concentration. This detection of olivine matches closely with Group 3 (which contains 11% olivine), unlike other spectra from this study that are deficient in olivine but otherwise correlate with Group 3 well. One such example is the eastern part of the Cerberus crater streak, which also is estimated to have approximately the same concentrations of pyroxene, plagioclase, and high-silica phases but no olivine whatsoever.

Gusev Crater and Gale Crater. Results from Gusev Crater are most consistent with a mineralogy dominated by HCP with potential contribution from olivine. The averaged spectrum from one of the low-albedo splotches within the crater is most similar to a pure clinopyroxene, in particular the absorption bands centered at $\sim 1.05 \mu\text{m}$ and

reflectance maximum between the two bands near 1.55 μm . This comparison can be seen in Figure 33, which shows the Gusev Crater averaged OMEGA spectrum plotted with a laboratory reflectance spectrum of a clinopyroxene (PYX114) from Horgan *et al.* (2014). Compositional data taken by the Spirit Rover suggest that the rocks in Gusev Crater are uniformly composed of olivine-rich basalt (McSween *et al.*, 2006). The ~ 1.05 μm absorption band is consistent with the characteristic 1- μm band center of olivine, as is the position of the longer-wavelength band maximum near 1.55 μm , but these features are shared with some varieties of HCP and are therefore not unique diagnostic features. The data points near 1.3 μm exhibit some deviation from the otherwise smooth slope of the 1- μm band's longer-wavelength absorption edge that could potentially be a shoulder resulting from an overlapping band unique to olivine, but the subtleness of this feature makes such a conclusion tenuous (compare this to the more distinct shoulder at the same position in the spectrum from Gale Crater). While signatures are present in the OLINDEX2 parameter map are supported by multiple spectral features consistent with olivine, it is not possible to confidently and uniquely identify olivine from the OMEGA data.

Mineralogical results from the low-albedo materials within Gale Crater are, like Gusev, consistent with an HCP and olivine mixture. The most compelling evidence for the presence of olivine is the composite band located near 1 μm that appears to consist of three overlapping bands. The middle band is centered at 1.05 μm , the long-wavelength band at 1.3 μm , and the short-wavelength band at 0.95 μm . The 2- μm absorption band centered near 2.1 μm is likely due to the presence of HCP, as it is the only mineral group

considered in this study that absorbs in this region. This interpretation is consistent with that of a previous study that analyzed the mineralogy of Gale Crater using TES and THEMIS data and inferred the composition of the dark sand dunes to be olivine-rich basalt (Rogers and Bandfield, 2009).

Implications. The similarity of the OMEGA spectra among many of the areas of interest in Elysium Planitia suggests that the low-albedo surfaces within them are composed largely of the same lithology. The 1- and 2- μm bands observed in these spectra are indicative of pyroxene, while the nature of the composite 1- μm bands is consistent with the presence of olivine due to the similarity between their band shapes. However, the variability of the band centers among the Elysium spectra suggests that minor differences in composition on the regional scale do exist.

Many of the spectra from the Elysium region analyzed here exhibit 1- μm absorption band centers near 1.09 μm , rather than at 1.05 μm which is typical of HCP or olivine. This effect is most likely due to mixing with iron-bearing glass, as it is the only species detected on the regional scale that has a 1- μm band center beyond 1.10 μm (*e.g.* Adams *et al.*, 1974b; Minitti *et al.*, 2002; Horgan and Bell, 2012). The prevalence of the longer-wavelength 1- μm bands suggests that iron-bearing glass is a significant component of the surfaces along the southern and eastern boundaries of Elysium Planitia, as revealed by the Aeolis and Cerberus areas of interest, in addition to the interior near the Elysium volcanic province. The origin of these deposits, if emplaced by pyroclastic air fall following explosive volcanic eruptions as the majority of widespread iron-bearing glass are assumed to be (Horgan and Bell, 2012), are most likely the Tharsis Montes or

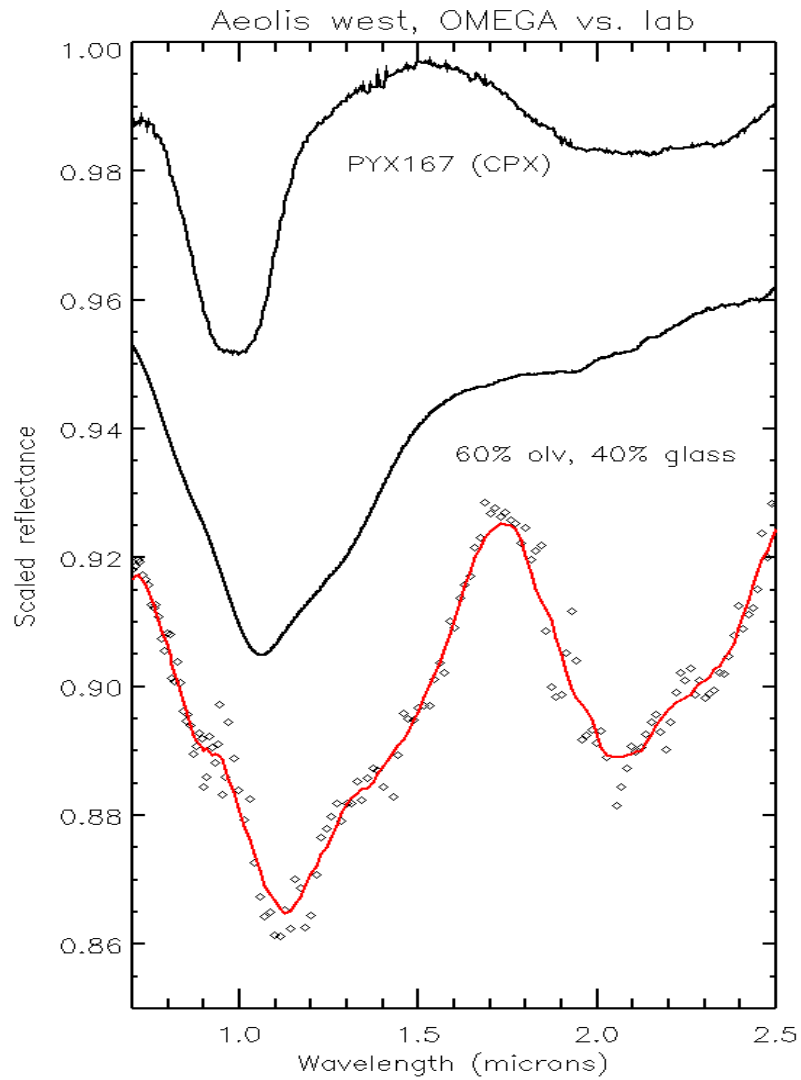


Figure 47. Averaged OMEGA spectrum from Aeolis west from Fig. 22 (red, bottom), plotted with laboratory spectra of a clinopyroxene (black, top) and intimate mixture of 60% olivine and 40% glass (black, middle).

Apollinaris Mons based on previous modelling of atmospheric pyroclast distribution (Kerber *et al.*, 2012).

The Aeolis west averaged spectrum, which is generally representative of many areas of interest in Elysium Planitia, is plotted with laboratory data of potentially equivalent mineral species in Figure 47 (Horgan *et al.*, 2014). The upper spectrum is a clinopyroxene (PYX167) that provides the best match with the observed data from Aeolis west with regard to the wavelength positions and relative depths of the 1- and 2- μm absorption bands. Nearly every other clinopyroxene sample exhibit a 2- μm band centered near 2.3 μm or beyond, but the ~ 2.1 band center of PYX167 is consistent with the OMEGA data. The middle spectrum is an intimate mixture consisting of 60% olivine and 40% iron-bearing glass. The shape of the 1- μm has a very good visual fit with Aeolis west, in particular the subtle shoulders present near 0.95 and 1.30 μm , which are interpreted as olivine. However, as mentioned previously, the wavelength positions of the 1- μm band center in many Elysium spectra are exceptionally high, residing near 1.10 μm (in the case of Aeolis west, just beyond it). This discrepancy is not resolvable using the reference laboratory data provided here, but is most likely due to even higher glass content than what the laboratory data in Figure 47 imply. Some varieties of iron-bearing glass do exhibit shallow absorptions near ~ 2.10 μm and have been detected on the Moon as potential pyroclastic deposits or impact melt (Mustard *et al.*, 2011; Horgan *et al.*, 2014).

TES deconvolution results from the limited number of low-albedo areas studied within Elysium Planitia suggest that the bedrock in the region is composed primarily of a

combination of the Group 2 spectral class, representative of Syrtis Major, and Group 3, which is representative of the southern highlands. The frequency of these two compositional groups in Elysium Planitia should not come as a surprise. The closest type areas from Rogers and Christensen (2007) to the areas of interest are all associated with Group 2 and Group 3, as evident from the map in Figure 46. The majority of the deconvolved TES spectra from the areas of interest indicate contribution primarily from either Group 2 or Group 3, or in many cases, both. In particular, these surfaces are characterized by high concentrations of pyroxene (generally ~30% but occasionally exceeding 35%) with comparatively lower amounts of feldspar that is highly variable (generally either ~15% or ~30% with few instances in between). While the abundance of Group 2 and Group 3 within Elysium Planitia and the proximity of their type areas are highly supportive of their significant contribution to the bedrock in this region, the detailed relationship between these groups is less clear. The overall extensiveness of Elysium Planitia compared to the relative scarcity of areas of interest in the region makes it difficult to infer the distribution of one compositional group to another with much confidence. While some averaged spectra appear to be intimate mixtures of Group 2 and Group 3 and do not fully match either composition (*e.g.*, Aeolis east, Cerberus west), others show near-perfect correlations with these spectral classes among the most common mineral species, indicating a purer mineralogy (*e.g.*, Elysium crater, Cerberus crater). One area of interest even exhibited pure Group 2 and Group 3 compositions from different locations within it (Aeolis west) despite having the same morphological expression.

Arabia Terra

The low-albedo deposits within the two unnamed craters in Arabia Terra are compositionally similar to many areas in Elysium Planitia and are interpreted to consist of high-calcium pyroxene mixed with mafic glass, in addition to possible minor amounts of olivine. The primary absorption features present at approximately at 1 and 2 μm are characteristic of pyroxene. The positioning of these features at relative high wavelengths ($>1 \mu\text{m}$ and $>2 \mu\text{m}$) indicate that high-calcium pyroxene is dominant over the low-calcium phase. However, the 1- μm bands for both areas are centered at $\sim 1.10 \mu\text{m}$, which is too high to be solely attributed to high-calcium pyroxene, for which the typical range is 1.0 to 1.05 μm . These higher-wavelength 1- μm band centers are probably due to the presence of iron-bearing glass, which has band centers in the 1.1 to 1.2- μm region (*e.g.* Adams *et al.*, 1974b; Minitti *et al.*, 2002; Horgan and Bell; 2012). The “type B” spectrum observed in the streak material for both craters in Arabia Terra is more enigmatic. The general spectral shape (broad 1- μm absorption, no 2- μm absorption) is broadly similar to that of Type-A clinopyroxene, but the precise positioning of the 1- μm band at $\sim 0.95 \mu\text{m}$ is too far shifted to shorter wavelengths and thus more consistent with LCP. These spectra might represent preferential physical weathering of mineral groups from the original “type A” splotch material as sediment is transported from the crater interior along the streak. Recent studies have proposed that lower-density rock-forming minerals in basaltic sands, in particular plagioclase, clays, and volcanic glass, are preferentially removed by aeolian processes (Stockstill-Cahill *et al.*, 2008). This process has the effect of enriching the mafic phases olivine and pyroxene to produce a mafic to ultramafic

compositions with as little as 40 wt. % silica. Mafic enrichment of basaltic sands has also been known to occur in Iceland, where the flat and elongated nature of the lighter plagioclase grains has made them more susceptible to mechanical alteration by wind (Mangold *et al.*, 2011). A similar process may be taking place in the unnamed Arabia craters analyzed here, in which lighter mineral grains are removed from the dark sand as it is transported from the splotch southward along the streak. The sand would become more highly concentrated in LCP and most likely olivine. Although the 1- μm spectral features diagnostic of olivine are not present in the “type B” streak spectrum (*i.e.*, composite band at 1.05 μm), spectral analysis of olivine and orthopyroxene mixtures in the laboratory indicate that olivine abundance must reach $\sim 70\%$ in order for its features to be identifiable from the strongly-absorbing orthopyroxene (Horgan *et al.*, 2014).

The deconvolved TES spectra from the unnamed craters in Arabia do not match any single spectral class from Rogers and Christensen (2007) very well. The mineralogy derived from at least part of the low-albedo intracrater splotch (ocks 2731 and 5284) exhibits approximately equal parts feldspar and pyroxene at 25 to 35% concentrations, which correlates most closely with Group 2 and Group 3 (Group 2: 31% feldspar, 33% pyroxene; Group 3: 25% feldspar, 30% pyroxene). High-silica phases are present at 20 to 25% concentrations in the intracrater Arabia deposits, which matches better with the more silica-rich Group 3 (18% high-Si) than Group 2 (12% high-Si). Contribution from Group 2 and Group 3 in the low-albedo deposits in the Arabia craters is expected given that the type regions for these compositional groups are located relatively nearby, as shown in Figure 48. The dark surfaces of Meridiani and Cimmeria-Iapygia, both of which

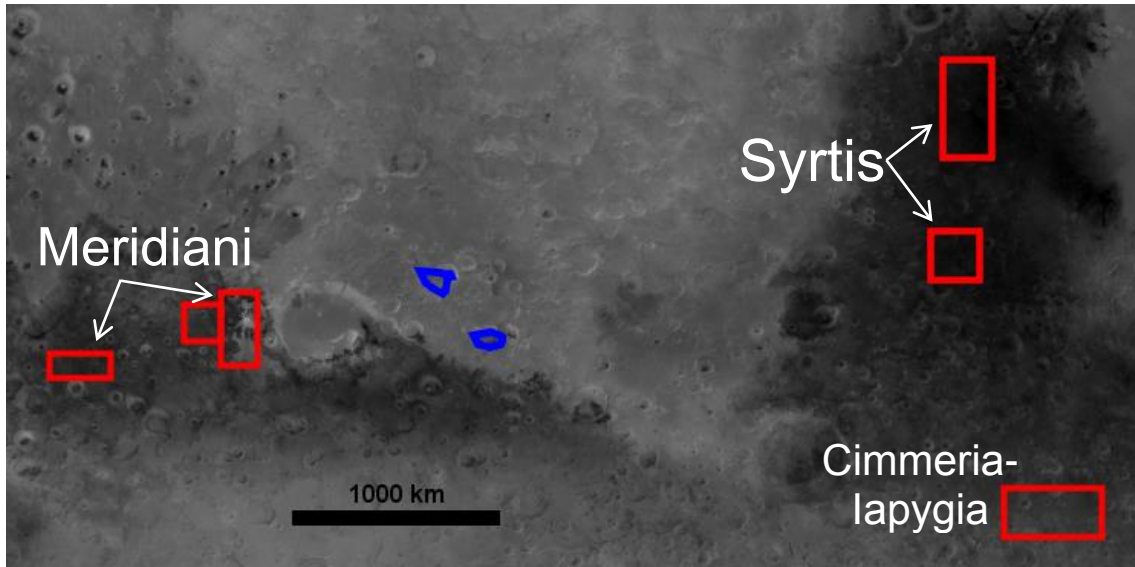


Figure 48. The location of the Arabia Terra areas of interest (blue outlines) in relation to type regions of the Rogers and Christensen (2007) spectral classes (red boxes). Syrtis is the type region of Group 2 while Meridiani is a member of Group 3.

are classified as Group 3, adjoin the southern boundary of Arabia Terra while surfaces representative of Syrtis Major and Group 2 are immediately to the east of southern Arabia Terra. The close proximity between the areas of interest and these type regions suggests that the bedrock in Arabia Terra is an intermediate between the Group 2 and Group 3 compositions. If the contrast in spectral shape between the “type A” and “type B” is indeed a result of mechanical alteration as sediments are transported from the splotch to the streak, the dark intracrater material is likely representative of the local bedrock. Christensen (1983) suggested that most low-albedo intracrater materials most likely consist of coarse sediment that has been transported by wind into the crater but cannot escape. The relatively high crater density in Arabia Terra would make it difficult for coarse sediment to experience extensive weathering during transport on the surface before getting trapped in a crater. Therefore, it is proposed that the low-albedo deposits in the Arabia craters are representative of the local bedrock in southern Arabia Terra.

CONCLUSIONS

63 different locations in the bright dusty regions of Mars were flagged as potential “windows” through the dust cover that might offer insight into the bedrock mineralogy of these regions. A minority of the areas analyzed using OMEGA near-infrared and TES thermal infrared data exhibited spectra consistent with mafic mineralogy, in particular the position and shape of the 1- μm absorption band. This work has led to the following conclusions.

1) Dozens of “windows” through the dust were identified using the DCI and MARCI methods, but only a small fraction of them yield spectra that are consistent with mafic mineralogy.

2) Bedrock from the flanks and surrounding plains of Arsia Mons contains significant amounts of LCP mixed with iron-bearing glass and HCP, as inferred from a single OMEGA image. Thermal data reveals that Arsia Mons is remarkably similar in composition to the nearby albedo features of Aonium Sinus and Sinus Meridiani. Other volcanic constructs in Tharsis did not yield any mineralogical signatures, and MARCI albedo data indicate that these surfaces are brighter than Arsia Mons even during the peak of annual dust-clearing events.

3) The bedrock in the Elysium Planitia region can be broadly characterized as HCP-rich basalt with contribution from iron-bearing glass and olivine. This represents a mixture between the general compositions of the southern highlands and Syrtis Major. The nature of this relationship across different locations, *i.e.*, whether there is an intimate mixture versus discrete occurrences of each composition, is unclear.

4) Bedrock composition from Arabia Terra is similar to that of Elysium Planitia, consisting of HCP-rich basalt with lesser amounts of mafic glass and olivine. The mineralogy of the sediment changes substantially as it is transported from the intracrater splotch to the surface streak, which may indicate enrichment of mafic phases due to preferential mechanical weathering. The bedrock in southern Arabia Terra is an intermediate between that of Syrtis Major and Meridiani.

REFERENCES

- Adams, J. B. (1974a), Visible and Near-Infrared Diffuse Reflectance Spectra of Pyroxenes as Applied to Remote Sensing of Solid Objects in the Solar System. *J. Geophys. Res.*, 79, 4829–4836.
- Adams, J. B., C. Pieters, and T. B. McCord (1974b), Orange glass: Evidence for regional deposits of pyroclastic origin on the moon, 5th LPSC, 1, 171–186.
- Bandfield, J. L., and M. D. Smith (2003), Multiple emission angle surface–atmosphere separations of thermal emission spectrometer data, *Icarus*, 161, 47–65.
- Bandfield, J. L. (2002), Global mineral distributions on Mars, *J. Geophys. Res.*, 107(E6), 5042.
- Bandfield, J. L., V. E. Hamilton, and P. R. Christensen (2000), A global view of Martian surface compositions from MGS-TES. *Science*, 287, 1626–1630.
- Bell III, J. F., E. M. Wolfe, B. N. H. Horgan, J. Joseph, S. Araki (2012), Kilometer-scale VIS-NIR spectral variations on Mars from global mapping and analysis of Mars Express OMEGA data, 43rd LPSC, abs. 1739.
- Bell III, J. F., M. J. Wolff, M. C. Malin, W. M. Calvin, B. A. Cantor, M. A. Caplinger, ... P. C. Thomas (2009), Mars Reconnaissance Orbiter Mars Color Imager (MARCI): Instrument description, calibration, and performance, *J. Geophys. Res.*, 114, E08S92.
- Bell III, J.F., T. D. Glotch, V. E. Hamilton, T. McConnochie, T. McCord, A. M. McEwen, ... R. E. Arvidson (2008), Visible to near-IR multispectral orbital observations of Mars, in *The Martian Surface: Composition, Mineralogy and Physical Properties*, edited by J. F. Bell III, chap. 8, Cambridge University Press, New York.
- Bell III, J. F., H. Y. McSween, J. A. Crisp, R. V. Morris, S. L. Murchie, H. J. Moore, ... L. Soderblom (2000), Mineralogic and compositional properties of Martian soil and dust: Results from Mars Pathfinder, *J. Geophys. Res.*, 105(E1), 1721–1755.
- Bibring, J.-P., *et al.* (2006), Global mineralogical and aqueous mars history derived from OMEGA/Mars Express data. *Science*, 312, 400–404.
- Bibring, J.-P., *et al.* (2005), Mars surface diversity as revealed by the OMEGA/Mars Express observations, *Science*, 307, 1576–1581.
- Bibring, J.-P., A. Soufflot, M. Berthé, Y. Langevin, B. Gondet, P. Drossart, ... F. Forget (2004), OMEGA: Observatoire pour la Minéralogie, l’Eau, les Glaces et l’Activité, *ESA Special Publication* 1240, 1-13.

- Burns, R. G. (1970) Mineralogical applications of crystal field theory, *Cambridge University Press*, London.
- Cantor, B., M. Malin, and K. Edgett (2002), Multiyear Mars Orbiter Camera (MOC) observations of repeated Martian weather phenomena during the northern summer season, *J. Geophys. Res.*, 107(E3).
- Christensen, P. R., E. Engle, S. Anwar, S. Dickenshied, D. Noss, N. Gorelick, M. Weiss-Malik (2009), JMARS – A Planetary GIS, *American Geophysical Union*, 2009 Fall Meeting, abs. #IN22A-06.
- Christensen, P. R., J. L. Bandfield, A. D. Rogers, T. D. Glotch, V. E. Hamilton, S. F. Ruff, and M. B. Wyatt (2008), Global mineralogy mapped from the Mars Global Surveyor Thermal Emission Spectrometer, in *The Martian Surface: Composition, Mineralogy, and Physical Properties*, edited by J. F. Bell III, chap. 9, Cambridge Univ. Press, New York.
- Christensen, P. R., S. W. Ruff, R. L. Fergason, A. T. Knudson, S. Anwar, R. E. Arvidson, ... M. B. Wyatt (2004), Initial results from the Mini-TES experiment in Gusev Crater from the Spirit Rover, *Science*, 305, 837–842.
- Christensen, P. R., et al. (2003), The Thermal Emission Imaging System (THEMIS) for the Mars 2001 Odyssey Mission, *Space Sci. Rev.*, 110, 85-130.
- Christensen, P. et al. (2001), Mars Global Surveyor Thermal Emission Spectrometer experiment: investigation description and surface science results. *J. Geophys. Res.*, 106(E10), 23,823–23,871.
- Christensen, P. R., et al. (1992), Thermal Emission Spectrometer Experiment: Mars Observer Mission, *J. Geophys. Res.*, 97(E5), 7719–7734.
- Christensen, P. R. (1986), Regional dust deposits on Mars: Physical properties, age, and history, *J. Geophys. Res.*, 91(B3), 3533–3545.
- Christensen, P. R. (1983), Eolian Intracrater Deposits on Mars: Physical Properties and Global distribution, *Icarus*, 56, 496–518.
- Clark, R. N. (1999), Spectroscopy of Rocks and Minerals, and Principles of Spectroscopy, in Manual of Remote Sensing, in *Remote Sensing for the Earth Sciences*, edited by A.N. Rencz, chap. 1, John Wiley and Sons, New York.
- Cloutis, E. A., and M. J. Gaffey (1991), Spectral-compositional variations in the constituent minerals of mafic and ultramafic assemblages and remote sensing implications, *Earth, Moon, and Planets*, 53, 11–53.

- Edwards, C. S., P. R. Christensen, and V. E. Hamilton (2008), Evidence for extensive olivine-rich basalt bedrock outcrops in Ganges and Eos chasmas, *Mars. J. Geophys. Res.*, 113, E11003.
- Flahaut, J., J. F. Mustard, C. Quantin, H. Clenet, P. Allemand, and P. Thomas (2011), Dikes of distinct composition intruded into Noachian-aged crust exposed in the walls of Valles Marineris, *Geophys. Res. Lett.*, 38, L15202.
- Greeley, R., and J. E. Guest (1987), Geologic map of the eastern equatorial region of Mars, *USGS I-1802-B*, 1:15M scale.
- Grotzinger, J. P., J. Crisp, A. R. Vasavada, R. C. Anderson, C. J. Baker, R. Barry, ... R. C. Wiens (2012), Mars Science Laboratory Mission and Science Investigation. *Space Science Reviews*, 170, 5–56.
- Hamilton, V. E., and P. R. Christensen (2005), Evidence for extensive, olivine-rich bedrock on Mars, *Geology*, 33(6), 433.
- Hartmann, W. K., M. Malin, A. McEwen, M. Carr, L. Soderblom, P. Thomas, E. Danielson, P. James, and J. Veverka (1999), Evidence for recent volcanism on Mars from crater counts, *Nature*, 397, 586–589.
- Hartmann, W. K. (2005), Martian cratering 8: Isochron refinement and the chronology of Mars, *Icarus*, 174(2), 294–320.
- Horgan, B.H.N., E. A. Cloutis, P. Mann, and J. F. Bell III (2014), Near-infrared spectra of ferrous mineral mixtures and methods for their identification in planetary surface spectra, *Icarus*, 234, 132–154.
- Horgan, B., and J. F. Bell III (2012), Widespread weathered glass on the surface of Mars. *Geology*, 40(5), 391–394.
- Johnson, J. R., P. R. Christensen, and P. G. Lucey (2002), Dust coatings on basaltic rocks and implications for thermal infrared spectroscopy of Mars, *J. Geophys. Res.*, 107, E6.
- Kerber, L., J. W. Head, J. Madeleine, F. Forget, and L. Wilson (2012), The dispersal of pyroclasts from ancient explosive volcanoes on Mars: Implications for the friable layered deposits, *Icarus*, 219, 358–381.
- Kieffer, H. H., T. Z. Martin, A. R. Peterfreund, B. M. Jakosky, E. D. Miner, and F. D. Palluconi (1977), Thermal and albedo mapping of Mars during the Viking primary mission, *J. Geophys. Res.*, 82, 4249–4292.

- Kieffer, H. H., J. S. C. Chase, E. Miner, G. Münch, and G. Neugebauer, (1973), Preliminary report on infrared radiometric measurements from Mariner 9 spacecraft, *J. Geophys. Res.*, 78, 4291–4312.
- Malin, M. C., W. M. Calvin, B. A. Cantor, R. T. Clancy, R. M. Haberle, P. B. James, ... S. W. Lee (2008), Climate, weather, and north polar observations from the Mars Reconnaissance Orbiter Mars Color Imager. *Icarus*, 194(2), 501–512.
- Malin, M. C., J. F. Bell III, B. A. Cantor, M. A. Caplinger, W. M. Calvin, R. T. Clancy, ... M. J. Wolff (2007), Context Camera Investigation on board the Mars Reconnaissance Orbiter. *J. Geophys. Res.*, 112, E05S04.
- Malin, M. C., and K. S. Edgett (2001), Mars Global Surveyor Mars Orbiter Camera: Interplanetary cruise through primary mission, *J. Geophys. Res.*, 106(E10), 23,429–23,570.
- Mangold, N., D. Baratoux, O. Arnalds, J.-M. Bardintzeff, B. Platevoet, M. Grégoire, and P. Pinet (2011), Segregation of olivine grains in volcanic sands in Iceland and implications for Mars. *Earth and Planetary Science Letters*, 310, 233–243.
- McSween, H. Y., M. B. Wyatt, R. Gellert, J.F. Bell III, R. V. Morris, R. V., K. E. Herkenhoff, ... J. Zipfel, (2006), Characterization and petrologic interpretation of olivine-rich basalts at Gusev Crater, Mars. *J. Geophys. Res.*, 111, E02S10.
- McSween, H. Y. and K. Keil (2000), Mixing relationships in the Martian regolith and the composition of globally homogeneous dust, *Geochim. Cosmochim Acta*, 64, 2155–2166.
- Minitti, M. E., J. F. Mustard, and M. J. Rutherford (2002), Effects of glass content and oxidation on the spectra of SNC-like basalts: Applications to Mars remote sensing, *J. Geophys. Res.*, 107(E5), 5030.
- Mouginis-Mark, P. J. (2002), Prodigious ash deposits near the summit of Arsia Mons volcano, Mars, *Geophysical Research Letters*, 29(16), 15–1–15–4.
- Mustard, J. F., C. M. Pieters, P. J. Isaacson, J. W. Head, S. Besse, R. N. Clark, ... S. Tompkins (2011), Compositional diversity and geologic insights of the Aristarchus crater from Moon Mineralogy Mapper data, *J. Geophys. Res.*, 116, E00G12.
- Mustard, J. F., F. Poulet, J. W. Head, N. Mangold, J.-P. Bibring, S. M. Pelkey, ... G. Neukum (2007), Mineralogy of the Nili Fossae region with OMEGA/Mars Express data: 1. Ancient impact melt in the Isidis Basin and implications for the transition from the Noachian to Hesperian, *J. Geophys. Res.*, 112, E08S03.

- Mustard, J. F., F. Poulet, A. Gendrin, J. P. Bibring, Y. Langevin, B. Gondet, ... F. Altieri (2005). Olivine and pyroxene diversity in the crust of Mars, *Science*, 307, 1594–1597.
- Noe Dobrea, E. Z. and J. F. Bell III (2005), TES spectroscopic identification of a region of persistent water ice clouds on the flanks of Arsia Mons Volcano, Mars, *J. Geophys. Res.*, 110, E05002.
- Palluconi, F. D., and H. H. Kieffer (1981), Thermal Inertia Mapping of Mars from 60°S to 60°N, *Icarus*, 45, 415–426.
- Pelkey, S. M., *et al.* (2007), CRISM multispectral summary products: Parameterizing mineral diversity on Mars from reflectance, *J. Geophys. Res.*, 112, E08S14.
- Peterfreund, A. R. (1981), Visual and infrared observations of wind streaks on Mars, *Icarus*, 45, 447–467.
- Ramsey, M. S., and P. R. Christensen (1998), Mineral abundance determination: Quantitative deconvolution of thermal emission spectra, *J. Geophys. Res.*, 103(B1), 577-596.
- Rogers, A. D. and R. L. Fergason (2011). Regional-scale stratigraphy of surface units in Tyrrhena and Iapygia Terrae, Mars: Insights into highland crustal evolution and alteration history, *J. Geophys. Res.*, 116, E08005.
- Rogers, A. D., and J. L. Bandfield (2009), Mineralogical characterization of Mars Science Laboratory candidate landing sites from THEMIS and TES data, *Icarus*, 203, 437–453.
- Rogers, A. D., J. L. Bandfield, and P. R. Christensen (2007), Global spectral classification of Martian low-albedo regions with Mars Global Surveyor Thermal Emission Spectrometer (MGS-TES) data, *J. Geophys. Res.*, 112(E02004), 1–29.
- Rogers, A. D. and P. R. Christensen (2007), Surface mineralogy of Martian low-albedo regions from MGS-TES data: Implications for upper crustal evolution and surface alteration, *J. Geophys. Res.*, 112(E1), 1–18.
- Rogers, A.D. and P. R. Christensen (2003), Age relationship of basaltic and andesitic surface compositions on Mars: Analysis of high-resolution TES observations of the northern hemisphere, *J. Geophys. Res.*, 108(E4), 5030.
- Ruff, S. W., and P. R. Christensen (2002), Bright and dark regions on Mars: Particle size and mineralogical characteristics based on Thermal Emission Spectrometer data, *J. Geophys. Res.*, 107(E12), 5127.

- Salvatore, M. R., J. F. Mustard, M. B. Wyatt, and S. L. Murchie (2010), Definitive evidence of Hesperian basalt in Acidalia and Chryse planitiae, *J. Geophys. Res.*, 115.
- Scott, D. H., and K. L. Tanaka (1986), Geologic map of the western equatorial region of Mars, *USGS I-1802-A*, 1:15M scale.
- Singer, R. (1981), Near-infrared spectral reflectance of mineral mixtures: Systematic Combinations of pyroxenes, olivine, and iron oxides. *J. Geophys. Res.*, 86(B9), 7967–7982.
- Skinner, J.A., Jr., T.M. Hare, and K.L. Tanaka (2006), Digital Renovation of the Atlas of Mars 1:15,000,000-Scale Global Geologic Series Maps, *LPSC XXXVII*, abstract #2331.
- Squyres, S. W., *et al.* (2007), Pyroclastic activity at Home Plate in Gusev Crater, Mars, *Science*, 316, 738–742.
- Stockstill-Cahill, K. R., F. S. Anderson, and V. E. Hamilton (2008), A study of low-albedo deposits within Amazonis Planitia craters: Evidence for locally derived ultramafic to mafic materials. *J. Geophys. Res.*, 113, E07008.
- Sullivan, R., R. Arvidson, J. F. Bell III, R. Gellert, M. Golombek, R. Greeley, ... J. Wray (2008), Wind-driven particle mobility on Mars: Insights from Mars Exploration Rover observations at “El Dorado” and surroundings at Gusev Crater. *J. Geophys. Res.*, 113, E06S07.
- Thomas, P., J. Veverka, S. Lee, and A. Bloom (1981), Classification of Wind Streaks on Mars, *Icarus*, 45, 124–153.
- Wellington, D. F. and J. F. Bell III (2013), *American Geophysical Union*, 2013 Fall Meeting, abs. #P41A-1910.
- Wilson, L., and J. W. Head (2007), Explosive volcanic eruptions on Mars: Tephra and accretionary lapilli formation, dispersal and recognition in the geologic record. *Journal of Volcanology and Geothermal Research*, 163(1-4), 83–97.
- Wyatt, M. B., and H. Y. McSween (2002), Spectral evidence for weathered basalt as an alternative to andesite in the northern lowlands of Mars. *Nature*, 417(6886), 263–266.
- Zuber, M. T., D. E. Smith, S. C. Solomon, D. O. Muhleman, J. W. Head, J. B. Garvin, J. B. Abshire, and J. L. Bufton (1992), The Mars Observer Laser Altimeter investigation, *J. Geophys. Res.*, 97, 7781 – 7797.